Research Article

Khakemin Khan, Zia Ur Rehman*, Shanshan Yao, Om Prakash Bajpai, Antonio Miotello*, Mohsan Nawaz, Michele Orlandi, Khalid Ali Khan, Abdulaziz A. Alanazi, and Magdi E. A. Zaki

Nanoscale engineering of semiconductor photocatalysts boosting charge separation for solar-driven H_2 production: Recent advances and future perspective

https://doi.org/10.1515/ntrev-2024-0104
received May 21, 2024; accepted September 15, 2024

Abstract: Photocatalytic hydrogen (H_2) production is regarded as an efficient method for generating renewable energy. Despite recent advancements in photocatalytic water splitting, the solar-to-hydrogen conversion efficiency of photocatalysts remains well below the 10% target needed for commercial viability due to ongoing scientific challenges. This review comprehensively analyzes recent advancements in nanoscale engineering of photocatalytic materials, emphasizing techniques to enhance photogenerated charge separation for efficient solar hydrogen production. Here we highlight the nanoscale engineering strategies for effective charge separation including crystal engineering, junction engineering, doping-induced charge separation, tailoring optoelectronic properties, hierarchical architecture, defects engineering, various types of heterojunctions, and polarity-induced charge separation, and discuss their unique properties including ferroelectric on spatial charge separation along with the fundamental principles of light-induced charge separation/transfer mechanisms, and the techniques for investigation. This study, critically assesses strategies for effective photogenerated charge separation to enhance photocatalytic hydrogen production and offers guidance for future research to design efficient energy materials for solar energy conversion.

Keywords: nanoscale engineering, charge separation, solar drive hydrogen production

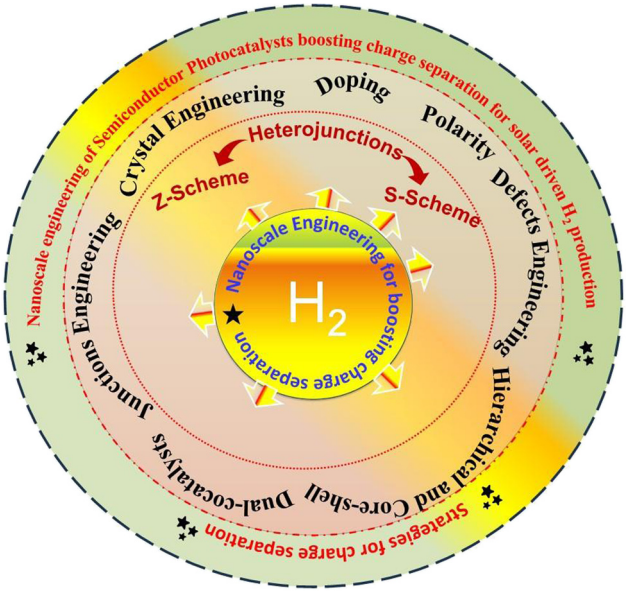

Graphical abstract: Graphical illustration of various strategies of nanoscale engineering boosting charge separation in semiconductor photocatalysts for photocatalytic hydrogen production.

*** Corresponding author: Zia Ur Rehman,** Institute for Advanced Materials, College of Materials Science and Engineering, Jiangsu University, Zhenjiang, 212013, China; Department of Chemistry, Hazara University, Mansehra, 21120, Khyber Pakhtunkhwa, Pakistan, e-mail: ziamwt1@gmail.com, tel: +86-13083590428
*** Corresponding author: Antonio Miotello,** Physics Department, University of Trento, Via Sommarive 14, 38123, Trento, Italy, e-mail: zia1marwat@hotmail.com
Khakemin Khan, Om Prakash Bajpai, Michele Orlandi: Physics Department, University of Trento, Via Sommarive 14, 38123, Trento, Italy
Shanshan Yao: Institute for Advanced Materials, College of Materials Science and Engineering, Jiangsu University, Zhenjiang, 212013, China
Mohsan Nawaz: Department of Chemistry, Hazara University, Mansehra, 21120, Khyber Pakhtunkhwa, Pakistan
Khalid Ali Khan: Applied College, Center of Bee Research and its Products (CBRP), Unit of Bee Research and Honey Production, King Khalid University, P.O. Box 9004, Abha, 61413, Saudi Arabia
Abdulaziz A. Alanazi: Department of Chemistry, College of Science and Humanities in Al-Kharj, Prince Sattam bin Abdulaziz University, Al-Kharj, 11942, Saudi Arabia
Magdi E. A. Zaki: Department of Chemistry, College of Science, Imam Mohammad Ibn Saud Islamic University, Riyadh, 11623, Saudi Arabia

1 Introduction

Significant carbon dioxide (CO_2) emissions from the overuse of fossil fuels in recent years have contributed to global warming and created challenges for sustainability and the environment [1,2]. Hence, it is crucial to decrease CO_2 emissions, and finding environmentally friendly and renewable alternatives to fossil fuels is becoming increasingly important, particularly considering the ambitious global climate regulations aimed at reducing coal consumption. A flexible energy source that is often considered as a potential answer to several energy-related problems is H_2. Significant interest has been expressed worldwide in it due to its very high gravimetric energy density, low greenhouse gas emissions, and compatibility with current production techniques and fossil fuel-powered infrastructure [3,4]. Presently, over 90% of the global H_2 production relies on fossil fuels, specifically through steam methane reforming, methane partial oxidation, and coal gasification methods. This results in the release of approximately 830 million tons of CO_2 annually, contributing to more than 2% of the total global CO_2 emissions each year [5,6]. Therefore, it is crucial to establish effective methods for generating H_2 while minimizing or eliminating carbon emissions. H_2 fuels derived from traditional fossil-fuel-based methods have a minimal or potentially adverse impact on reducing global warming [7]. Solar energy, being both abundant and renewable, holds great promise as an environmentally friendly option for H_2 production due to its plentiful supply and capacity for energy generation [8–10]. This discovery by Fujishima and Honda in 1972 has led to the development of semiconductor-based photocatalysis, which is a promising environmentally friendly technology for converting solar energy and addressing the aforesaid issues [11,12]. Consequently, there has been significant research on highly efficient semiconductor-based photocatalysts comprising special morphologies and unique compositions. These catalysts have been widely investigated for a range of processes, such as water splitting [13–15], and CO_2 reduction [16–18]. However, the efficiency of semiconductors in photocatalysis hinges on the kinetics of photogenerated charge transfer and separation, crucial for advancing toward commercial practicality. Current developments fall short of achieving a sustainable hydrogen production rate of 10% required for economic viability.

Over the last 50 years, there have been significant advancements in solar-powered hydrogen (H_2) production technology. The number of research articles on solar-driven H_2 evolution has increased dramatically since 2005, as depicted in Figure 1(a). After successfully resolving issues with system performance, longevity, and cost, significant progress has been made in the deployment and use of solar hydrogen production [19–24]. According to the data presented in Figure 1(b), by 2035, renewable energy sources are expected to account for more than 50% of global power generation. Most of this energy will be generated through solar power. This indicates a significant untapped potential that goes beyond current usage. As a result, research efforts are being directed toward developing economically viable technologies for converting, storing, and utilizing solar energy [25].

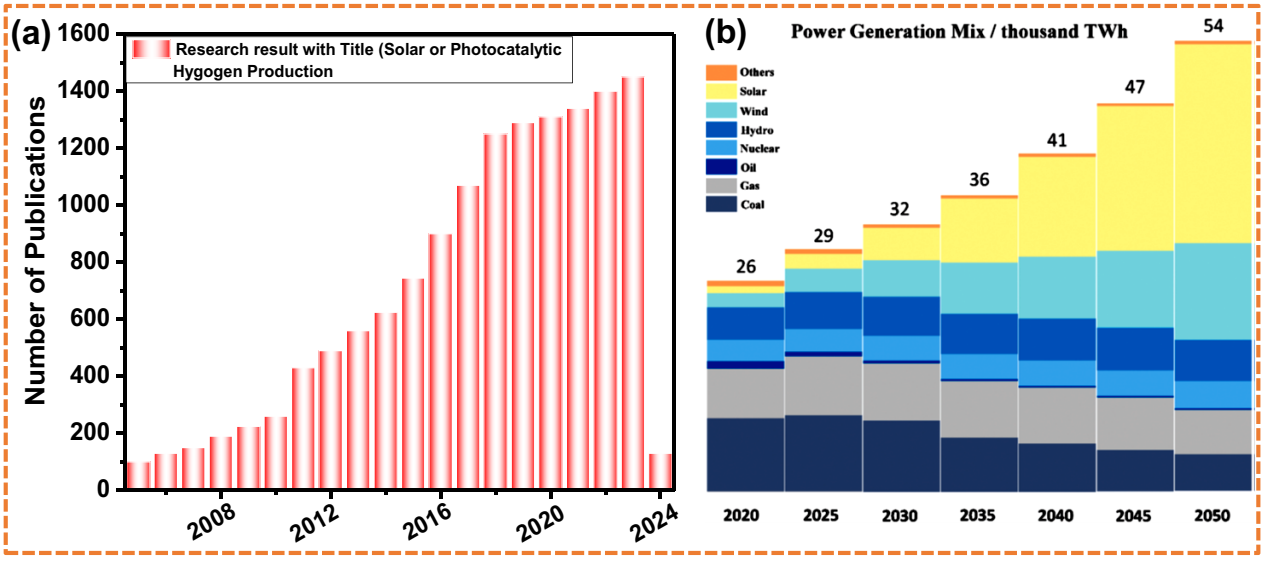

Figure 1: (a) Number of publications per year. The data were collected from Web of Science Core Collection on January 14, 2024. (b) Information from McKinsey and Company about the global energy forecast. One thousand terawatt-hours is used to measure the power-producing mix (TWh) [25].

However, due to the growing world population, it is projected that the crude oil will be required to provide the world's energy needs in various forms like oil, gas, and coal for at least another 50 years, as shown in Figure 1(b) [26]. As to date, the maximum documented solar-to-hydrogen (STH) conversion efficiency for the photocatalytic water splitting system is below 5%, while commercial feasibility requires 10%. Numerous ways have been studied to improve STH efficiency by adjusting light absorption, charge transport, and redox kinetics for water-splitting events. However, STH efficiency improved somewhat. Criticizing the rationale and important techniques may be crucial to moving forward. However, in most review articles on photocatalytic hydrogen production systems, there has been insufficient focus on nanoscale engineering strategies for charge separation when comparing the apparent quantum efficiency (AQE) and STH conversion efficiency. Herein, we highlighted the various key strategies of nanostructure engineering for boosting photogenerated charge separation for photocatalytic hydrogen production using semiconductor photocatalysts. Finally, the limitations of current photocatalytic H_2 production systems are discussed, as well as future directions for creating an efficient photocatalytic system.

2 Photocatalytic water splitting principles and mechanism

Water molecule is split into hydrogen and oxygen molecules upon light irradiation on the exposed surface of the photocatalysts, where the overall reaction is given as follows:

$$2H_2O + \text{Light energy} \rightarrow 2H_2 + O_2. \quad (1)$$

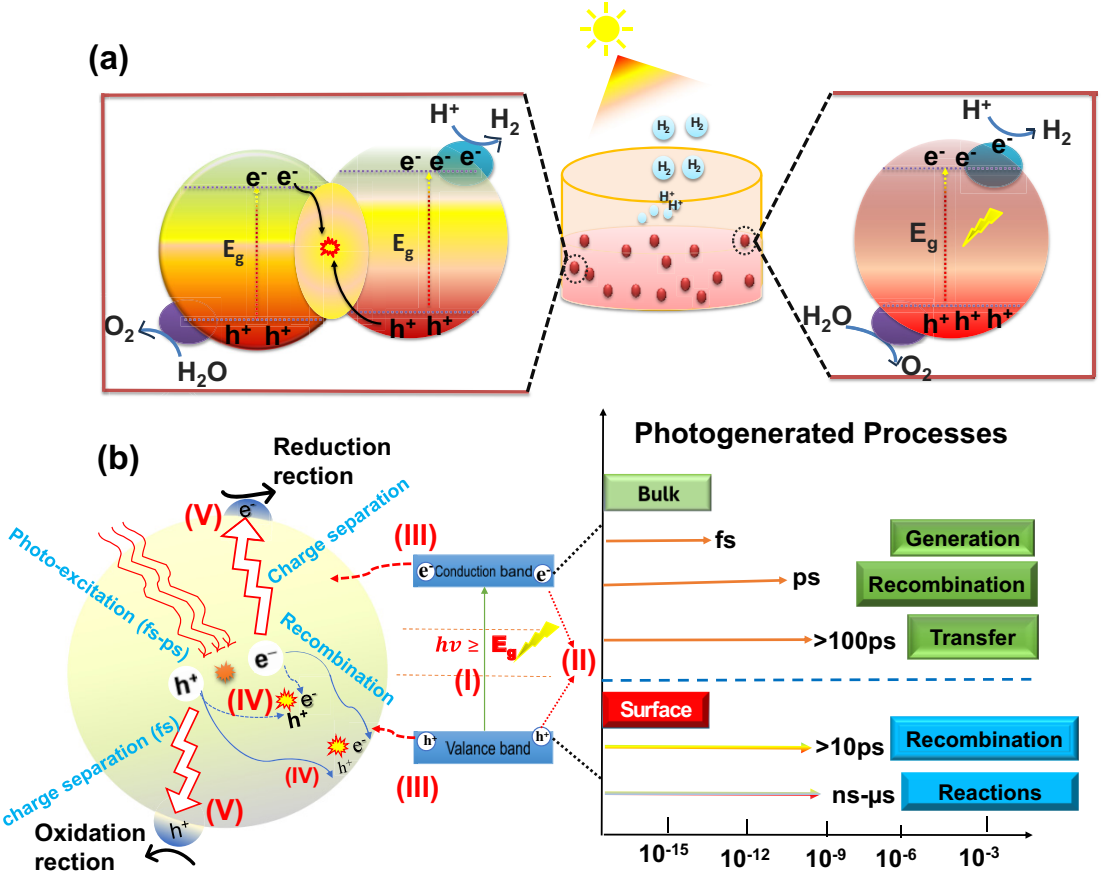

Figure 2: (a) Mechanism of photocatalytic water splitting on a semiconductor-based photocatalyst. (b) Diagrammatic representation of the various stages of charges generation and propagation on semiconductor photocatalysis together with the associated time scales: (I) photoinduced charges generation in the semiconductor take few fs; (II) Electrons and holes recombination take place in ps; (III) photogenerated electron–hole pairs reach the surface within hundreds of ps; (IV) Surface recombination take place in 10 ns; and (V) The charges are involved in catalytic reactions within microseconds to nanoseconds (ns).

Photocatalytic water splitting on a semiconductor is typically achieved *via* three basic processes in heterogeneous photocatalysis as shown in Figure 2(a) [27]. (i) When light having energy greater than the bandgap of the semiconductor falls on the photocatalyst causes the electron to move to higher energy state, *i.e.*, conduction band (CB) and holes are created in the valence band (VB); (ii) upon light irradiation, photoinduced charges overcoming coulombic barrier, diffuse and transfer to the surface of the photocatalysts; and (iii) in photocatalysis, the electron–hole pairs are used in redox reaction and the efficiency is calculated based on the above three steps. It is crucial to emphasize that photo-induced charge separation and surface catalytic reactions are collectively represented by "η."

$$\eta = \eta_{LH} \times \eta_{CS} \times \eta_{CU}, \tag{2}$$

where η_{LH} represents light utilization, η_{CS} represents the proficiency of charge separation, and η_{CU} represents the effectiveness of charge consumption. For solar-driven H_2 production, a suitable bandgap position of a photocatalyst is required to absorb more light as it can to create more photogenerated electron-hole pairs [28]. However, reducing the bandgap inclines to diminish the driving power for subsequent separation of charges and reactions on the surface during photocatalytic reactions. Furthermore, excellent photocatalysts must possess exceptional charge separation capabilities, as charge recombination takes place rapidly (between picoseconds [ps] to milliseconds [ms]) and poses a significant challenge for the separation of photogenerated charges. Besides, photoinduced charge (femtosecond [fs]–ps) and photogenerated charge separation (ps–ms) are very quick as compared to surface catalytic reaction (ms–s) that shows long live photogenerated charges for the facilitation of surface redox reactions as shown in Figure 2(b) [29,30]. Charge separation and charge utilization, *i.e.*, surface reaction are not independent, but synergistically corelated for the efficiency of photocatalysts [31,32]. An accelerated catalytic reaction will promote enhanced charge separation, and conversely, a decelerated reaction will hinder efficient charge separation. In the photocatalytic whole water splitting process, it is important to monitor the production of H_2 and O_2 gases in a balanced ratio of 2:1. Equations (3) and (4) demonstrate how the whole water-splitting process may be separated into two half reactions.

$$2H^+ + 2e \rightarrow H_2\text{HER}, \tag{3}$$

$$H_2O + 2H^+ \rightarrow \frac{1}{2O_2}\text{OER}. \tag{4}$$

Sacrificial reagents, such as electron donors and acceptors, are often used in investigating the H_2 and O_2 evolution reactions because of the challenging thermodynamic and kinetic constraints. This is called half-cell reaction, which is easier than whole water splitting in which hydrogen and oxygen are produced in the absence of sacrificial agents. These reactions have a much lower Gibbs free energy (ΔG) compared to overall water splitting (OWS), which has a ΔG of 237 kJ mol^{-1}. Some of these reactions even have a negative ΔG [33,34]. It is important to note that achieving significant photocatalytic activity in the two half-cell reactions is relatively easier than in OWS, but this is not the ultimate objective and does not constitute OWS. However, using biomass-containing compounds as hole scavengers in value-added oxidation reactions can be a viable alternative because they have lower thermodynamic requirements compared to the water oxidation reaction. Biofuel-derived organic molecules, including a byproduct of biodiesel production like glycerol, 5-hydroxymethylfurfural, CH_3OH, and CH_3CH_2OH (produced by fermentation of biomass), and urea (found in wastewater), will help in the oxidation process. The involvement of intricate processes such as carbon oxygen bond breakage, selective oxidations, catenation as C–C, and activation of C–H is possible [35,36]. Additionally, there is a need for the deliberate design of photocatalysts to allow for the targeted biomass valuation and controlled production of intermediates. The literature has provided additional information regarding the production of hydrogen through photocatalytic biomass conversion [37–41].

2.1 Charge separation and propagation in semiconductors

Semiconductor photocatalysts randomly transfer charge without a driving force. Thus, photogenerated charge recombination is most likely and photogenerated carriers are unlikely to reach active locations for redox reaction. Most photocatalytic carriers are consumed up by charge recombination before reaching reactive spots on the surface [42]. The propagation of electrons and holes in semiconductor photocatalysts is termed as electron and hole mobility, respectively. Their specific directions of mobility can be expressed in the following equation as [43]:

$$\mu = e\frac{\tau_c}{m^*}, \tag{5}$$

where the symbol τ_c represents the duration of charge carrier collisions, while m^* refers to the effective mass. The carriers' movement is driven by two forces: the concentration gradient and the internal electric field. These forces correspond to the mechanisms of diffusion charge separation and drift charge separation, respectively [44].

Carrier mobility, which is mostly dependent on the molar concentration of the electron and hole masses dictated by the semiconductors' electronic structure, has a significant impact on photocatalytic efficacy. Clearly, the electron mobility greatly surpasses that of the holes. Electrons and holes naturally disperse from regions of high carrier concentration to regions of low carrier concentration due to thermal kinetics in the presence of a concentration gradient. This process is known as diffusion current. In the same way, the existence of an electric field will also result in the occurrence of drift current due to the potential gradient. Drift currents and diffusion currents make up the entirety of the total current that is generated by the semiconductor technologies. The current density as overall can be calculated as follows [45]:

$$\begin{aligned} J_{\text{Total}} &= J_{\text{pdiffusion}} + J_{\text{ndiffusion}} + J_{\text{pdrift}} + J_{\text{ndrift}} \\ &= -qD_{\text{p}}\frac{d_{\text{p}x}}{d_x} + qD_{\text{n}}\frac{d_{\text{n}x}}{d_x} + pq\mu_{\text{p}}E_x + nq\mu_{\text{n}}E_x, \end{aligned} \tag{6}$$

where the diffusion coefficients are represented by D_{p} and D_{n}, while the charges are represented by $+q$ and $-q$, where $+q$ stands for holes and $-q$ for electrons. The dispersion of excited carriers primarily affects carrier mobility in a semiconductor in the absence of an electric field. Conversely, unequal dispersion of foreign particles or fluctuations in the potential of the electronic structure can create an internal electric field and non-zero current density within the semiconductor. This electric field makes it easier for electrons and holes to separate by pushing them in opposing directions toward the band-bending region. Built-in electric fields may be produced *via* surface/interface engineering methods, ferroelectric fields, and macroscopic polarization fields, in addition to the inherent internal polar electric fields found in certain semiconductor compounds with unique crystal structures. These methods involve spatial loading of cocatalysts, engineering crystal facets, and heterojunction formation. Semiconductors with varied atomic configurations and terminal bonding networks on their surfaces create distinct potential landscapes. When different electronic states and energy levels of crystal facets are revealed, charges redistribute in order to balance the energy levels between the facets and the bulk material. Crystal facets with a higher Fermi energy (E_{f}) tend to have an accumulation of holes, while facets with a lower Fermi energy (E_{f}) are where electrons tend to cluster. Consequently, there exists an internal electric field that flows from regions with higher Fermi energy to areas with lower Fermi energy at the two surfaces as a result of band bending in opposite directions. Unlike drift charge separation, which relies on an internal electric field, diffusion charge separation in photocatalyst systems involves the separation of charges through diffusion [46]. According to Chen *et al.*, the difference in electron and hole mobilities promotes a diffusion-based charge separation mechanism, enhancing charge separation across different crystal facets [44].

2.2 Characterization of charge separation and propagation in semiconductors

With respect to the kinetics of charge transport, light-induced charge separation and transfer usually happen extremely quickly, on the order of fs–ns. This technique covers nanometer and micrometer lengths simultaneously. Consequently, as Figure 3 illustrates, in order to better comprehend the photoinduced charge transfer mechanism and clarify the basic principles of photocatalytic processes, complex time- and space-resolved characterization approaches are essential.

2.2.1 Space-resolved techniques for charge separation and propagation

Advanced methods like surface photovoltage microscopy, scanning probe microscopy, and photochemical imaging are used to study photocatalytic charge transfer and detect separation of charges at a smaller scale. The technique of

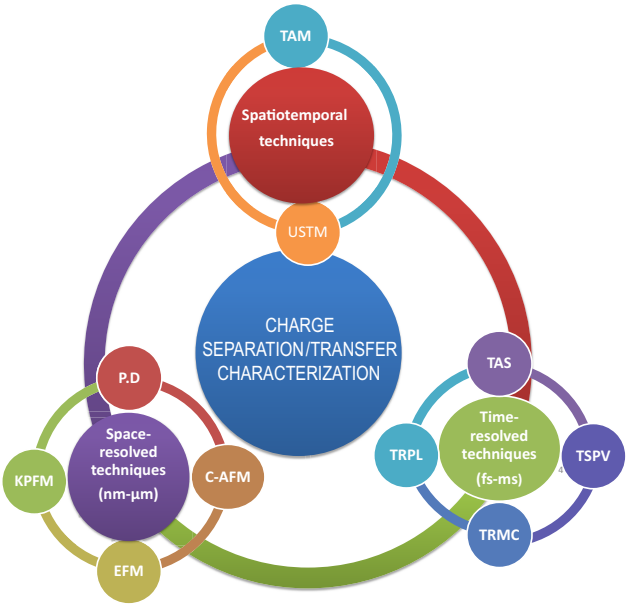

Figure 3: A comprehensive classification of the leading cutting-edge time- and space-resolved techniques for characterizing charge flow characteristics in semiconductor-based photocatalyst.

selectively depositing metals (like Pt and Au) or metal oxides (like MnO_x and PbO_2) on certain surfaces of a material by *in situ* redox reactions is known as facet-selective photodeposition. Light-induced electrons and holes interact with metal ion precursors in these reactions. Scanning probe microscopy methods are used to analyze the properties of the charge separation; Kelvin probe force microscopy (KPFM) is very helpful in this regard [47]. The electrostatic force microscope (EFM) [48] and conductive atomic force microscope (C-AFM) [49] are primarily used to elucidate the kinetics and spatial distribution of photogenerated charges at the micro-nano scale. This makes it easier to conduct a thorough analysis of the reaction mechanism. Surface voltage is detected using KPFM, which measures work function variance between a conductive tip and photocatalysts due to its exceptional sensitivity and spatial resolution [50,51]. With the use of Coulombic forces, EFM can measure the charge density produced by light and directly view the distribution of electric charges on a surface [52]. Electric current flowing between the conductive tip and the specimen surface may be measured using conductive atomic force microscopy (C-AFM). The examination of charge separation and transport characteristics in photocatalysts is made possible by this capacity [53]. Due to the unique properties of different characterization methods, certain limitations are inevitable, *e.g.*, performing KPFM measurements in an aqueous solution under alternating current (AC) voltage is challenging due to the movement of ions in the solution. Additionally, it is essential for the sample under examination to have good conductivity and secure attachment to the substrate, considering the potential impact of charge transfer between the sample and substrate. The surrounding dielectric environment can significantly affect the signal-to-noise ratio in EFM measurements. Moreover, in C-AFM contact mode, issues such as worn or contaminated tips can often arise [54]. The distribution of charges produced by light on the surface of photocatalysts may be directly seen using scanning probe voltage microscopy (SPVM). This is accomplished by contrasting scanning probe microscope photos that were captured at the same spot in both light and dark conditions. Recently, light-illuminated KPFM has been created as a powerful method for monitoring local potential fluctuations on photocatalyst surfaces in real-time. It reveals unique patterns of charge movement caused by photogenerated charges during photoirradiation [54]. Moreover, a modified form of light-illuminated KPFM has been employed to develop a technique known as frequency-modulated spatially resolved surface photovoltage spectroscopy (SRSPS). This method enables quantitative measurement of the forces driving charge separation in photocatalytic reactions [55].

2.2.2 Time-resolved techniques for charge separation and propagation

For the investigation of ultrafast charge transport dynamics, various characterization tools of time-resolved spectroscopy (TAS), transient surface photovoltage (TSPV), time-resolved photoluminescence (TRPL), transient response fourier spectroscopy, *etc.* are used which determine the time below fs [56,57]. The ground and excited states are characterized by transient absorption spectroscopy (TAS), which also looks at how photogenerated charge carriers combine with radiation. In time-resolved absorption spectroscopy (TAS), a group of energized electrons is generated by pulsed lasers. Subsequently, a faint pulse, delayed by a time interval τ, is employed to examine the sample. Excited state absorption signals (positive values) and stimulated emission (negative values) are the two main types of TAS signals used for the study. A differential absorption spectrum is the difference in absorbance between excited state and ground state absorbance. This spectrum is valuable for obtaining important kinetic information about photocatalyst charge carriers [58]. Time-resolved absorption spectroscopy (TAS) allows for the generation of excited states, the study of various electron transition processes, and the exact determination of electron and hole lifetimes. Conversely, absorption spectroscopy focuses on the shifts from the initial state to the higher energy state, whereas TRPL examines the opposite shifts that result in luminescence. Photoinduced electron and hole recombination may be studied on a variety of timeframes thanks to TRPL. The TRPL spectrum offers vital information on the charge kinetics of photocatalysts [59,60]. TRPL accurately measures the lifetimes of charge carriers but does not replicate the kinetics of charge separation. In contrast, TSPV spectroscopy analyzes the shape, duration, sign, and intensity of spectra to elucidate details about charge generation, separation, capture, and recombination processes. This method provides insights into the efficiency, direction, and mechanism of charge separation in photocatalytic devices [61]. While it is considered a semi-quantitative or qualitative approach operating at the ns level, time-resolved microwave conductivity (TRMC) measurements offer a direct and quantitative method to determine the lifetimes and local mobility of charge carriers generated by light. This technique allows for precise evaluation of the inherent characteristics and charge dynamics of photocatalysts [62]. A high-energy, pulsed electron beam generate transient charge carriers, when a photocatalyst is exposed to it. TRMC allows for the direct evaluation of charge carrier mobility and determination of their density, eliminating the requirement for supplementary independent measurements. This makes TRMC an effective method for studying the dynamics and characteristics of photocatalysts.

2.2.3 Spatiotemporal techniques for charge separation and propagation

The research employs sophisticated methods, including ultrafast spectroscopy, transient absorption microscopy (TAM), and ultrafast scanning tunneling microscopy (USTM), to investigate the dynamics of excited-state charges in photocatalysts [63]. They reveal important spatiotemporal features related to the rapid separation of charges, such as the duration of exciton existence, the average distance traveled before scattering, and the diffusion length and coefficient of charges [64,65]. Since TAM monitors the absorption signal of excited charges or excitons, it may be used to any kind of photocatalytic material. Nonetheless, the signals may include artifacts due to the existence of very dense excited states. However, USTM is a useful technique for comprehending transient dynamics and charge transport on photocatalyst surfaces. However, since electron tunnelling between the sample and the tip may change the inherent dynamics of the catalysts, applying it to samples with rough surfaces is difficult. Modern spectroscopic and microscopic technologies with great spatial and/or temporal resolution have made it possible to investigate basic scientific problems about single-particle photocatalytic processes. They provide insights into the charge separation driving force, the spatial distribution of reaction active sites, and the structural properties of photocatalysts. Despite potential limitations, continued advancements in characterization techniques will be crucial for the advancement of photocatalysis. Moreover, integrating multiple technologies can potentially lead to a more comprehensive understanding of photocatalytic processes.

2.2.4 Characterization techniques

Choosing the best method for characterizing charge separation in semiconductor-based photocatalysts depends on the specific aspects of charge dynamics one aims to investigate. Each technique offers unique strengths and insights, making them complementary rather than universally superior. No single technique can be deemed the best for all scenarios, as each has unique advantages. For a comprehensive understanding of charge separation, combining multiple techniques is often the most effective approach.

(a) **For spatial information**: Space-resolved techniques like KPFM and SPVM are ideal.
(b) **For temporal dynamics**: Time-resolved techniques like TAS and TRPL are essential.
(c) **For integrated insights**: Spatiotemporal techniques like TAM and USTM provide the most complete picture by combining spatial and temporal resolution. In practice, using a combination of these methods can provide a thorough characterization of charge separation processes, leveraging the strengths of each to obtain a detailed and holistic understanding of the photocatalytic system

3 Nanoscale engineering approaches enhancing charge separation for solar-driven hydrogen production

Nanoscale engineering is essential for improving the separation of charge carriers and speeding up their kinetics, which is particularly important for applications in photovoltaics, photocatalysis, and electronic devices. Here are some strategies used in nanoscale engineering to achieve effective charge separation for reactions. In photocatalytic processes, photoexcitation generates energetic electron–hole pairs that need to travel to the surface-active sites without recombining in order to participate in the catalytic activity. Remarkably, bulk charge recombination occurs within a few ps, whereas bulk charge separation takes hundreds of ps [66]. Since surface processes for creating solar fuel follow the diffusion equation, charge separation, and enhancement of charge utilization are critical functions of nanoscale engineering.

$$\tau = \frac{d^2}{K^2 D}. \tag{7}$$

The enhancement of charge transfer can be achieved by decreasing the diffusion time (t), which is determined by the particle size (d), a constant (k), and the diffusion coefficient of charge carriers (D). This can be accomplished by either reducing the distance over which diffusion occurs or augmenting the coefficient of diffusion. Creating catalysts at the atomic scale greatly reduces the distance over which charge can diffuse. Alternatively, improving the efficiency of charge transfer by creating faster pathways or increasing the driving force for charge separation at the atomic level can result in a higher diffusion coefficient. This, in turn, leads to faster separation and transfer of charges. These enhancements facilitate the increased migration of electrons and holes from the interior of the photocatalyst to its surface during its limited average lifespan.

Charge carrier separation can be improved in several ways. When it comes to devices like photocatalysis and solar cells, where good charge separation leads to better performance, these methods are especially helpful. Here are some well-known techniques.

3.1 Doping-induced charge separation properties

Doping involves adding trace amounts of elements to other materials to tailor their properties. The main goal of semiconductor doping is to modify the phases, shapes, dimensions, and electrical configurations of the crystal to change its optoelectronic properties [67]. Doping, for instance, permits prolonged light absorption in the solar spectrum from the visible to the near-infrared region. Additionally, doping helps to construct a bandgap that enhances conductivity and creates redox-active sites on the material's surface [68,69], resulting in an enhanced quantum efficiency (QE) of the materials [70–73]. Early studies about doping in photocatalysts contained the utilization of Cr/TiO_2 and $Rh/SrTiO_3$. Light absorption properties of such large bandgap materials were extended beyond the wavelength of 500 nm upon doping due to the creation of an additional energy level below the bandgap of the materials [74,75].

One effective method for enhancing charge separation is to add an extra built-in electric field (E_f) to the bulk of the nanostructure, which accelerates the separation of photogenerated charges. Research has demonstrated that doping semiconductors with metal and nonmetal atoms can alter their electrical, optical, and structural characteristics [76,77]. For instance, when phosphorus (P) atoms are doped into sulfide-based semiconductors, midgap impurity levels below the CB are created. This adjustment to the electrical band structure can modify the carrier concentration [78]. Theoretical studies have confirmed that doping metal sulfides with foreign atoms can create spin-polarized states while retaining the direct bandgap character. These states could significantly impact the separation of photogenerated charges [79]. Furthermore, it has been discovered that the addition of nitrogen-doped titanium dioxide (N-doped TiO_2) greatly increases light absorption, which dramatically enhances photocatalysis's ability to produce hydrogen [80]. An important case of $SrTiO_3$ which is an ultraviolet-active material as shown in Figure 4(a), but after doping with Rh^{4+}, it became a visible-light-active material for photocatalytic hydrogen production [81]. Therefore, the d–d transition brought on by doping is responsible for the increase in intrinsic absorption

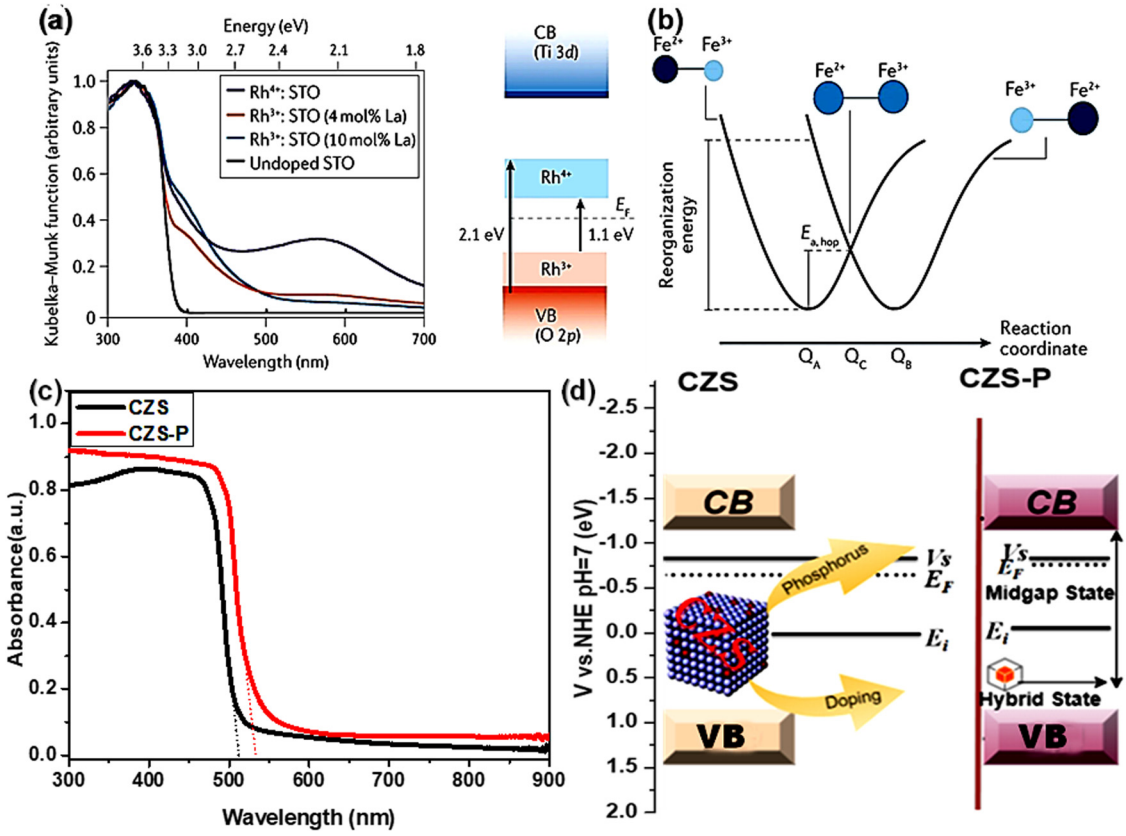

Figure 4: Effect of doping on the light harvesting: (a) $SrTiO_3$ in its lowest state left side, while the bending after Rh^{4+} is shown on the right side. (b) Graphical illustration of electron transport phenomenon, reused after permission from Pastor *et al.* [72]. (c) UV-Vis spectra of CdZnS and P-doped CdZnS. (d) Energy level representation of CdZnS and P-doped CdZnS, reused after permission from Khan *et al.* [6].

at wavelengths longer than 400 nm. In addition, single doping a cooping of certain metals, such as Sb, Rh, Ta [82,83], and Cr, is carried out to maximize polaron transit and carrier density; this balance is required to counter the effects of single metal doping [84]. Consequently, when the investigation was conducted in electrolytes with very high concentrations, immobilized trapped particles in TiO_2, α-Fe_2O_3, and WO_3 demonstrated remarkably extended lives. When compared to pure TiO_2, N, S co-doped TiO_2 has greater visible light absorption and charge separation, resulting in increased hydrogen generation [85]. Besides, carbon and fluorine co-doped ZnO result in a shorter bandgap and shallow energy levels that enhance charge separation, leading to greater hydrogen evolution rates [86].

Si-doping α-Fe_2O_3 offers a multi-pronged approach to enhancing photocatalytic performance. It simultaneously increases light absorption, improves material conductivity, elevates active site concentration, facilitates polaron transport by lowering the activation energy [81], as shown in Figure 4(b). Si-doping induces a new low-energy state in α-Fe_2O_3, resulting in longer bond lengths and reduced activation energy. This permits polarons (electron carriers) to travel more freely, increasing electrical conductivity, which is a critical factor limiting performance. Furthermore, these novel states may operate as traps for polarons, thereby increasing reaction rates [81]. Molecular dynamics simulations show that Cu incorporation in TiO_2 eliminates shallow trap states and isolates deep traps from free charges, enhancing photocatalytic activity for hydrogen production [87]. The applicability of these advantages to other dopants, however, depends on their atomic radius and the extent of crystal deformation that results [72,88]. It highlights the importance of the metal dopant's valence state, showing that increased visible light absorption does not always lead to higher hydrogen production. This is because transition metal cations create midgap states, allowing longer wavelengths of light to pass and promoting charge recombination, which reduces efficiency [89,90]. More precisely, in the case of deep dopant, a very small amount of the dopant remains active [72]. Establishing the maximum mass loading of dopants, expressed as weight percentage, that maintains the highest hydrogen production rate without decline is essential for cyclic hydrogen generation. Most studies have produced hydrogen using sacrificial agents. However, it is now imperative to generate hydrogen without such agents. Recent advancements have demonstrated this with a photocatalyst composed of $Rh_{2-y}Cr_yO_3$ loaded on Al-doped $SrTiO_3$, achieving an AQE of 0.4 at% at a wavelength of 365 nm. In this system, Rh_{2-y}-Cr_yO_3 acts as a cocatalyst, facilitating the preferential reduction of protons.

The addition of aluminum (Al) in $SrTiO_3$ eliminated deep Ti^{3+} recombination sites, reduced electron density, and raised the Fermi level, leading to stronger oxidizing potentials under sunlight. This reduction in Ti^{3+} states decreased hole and electron trapping, achieving an STH efficiency of 0.11%. Using Rh/Cr_2O_3 and CoOOH on specific STO facets at wavelengths of 350–360 nm resulted in an impressive QE of about 96% and an STH efficiency of 0.65%. This high QE is due to unique charge separation along anisotropic facets, effectively preventing charge recombination.

Similar to P-doping in CdZnS (CZS), Khan *et al.* observed a slight red shift (505–515 nm) in the absorption edge upon doping (CZS-P). This shift suggests a minor bandgap reduction (2.50–2.40 eV) attributed to the creation of midgap states (Figure 4(c) and (d)). These states, as proposed, enhance charge separation by introducing an internal electric field, potentially leading to increased photocatalytic hydrogen production [91,92]. Metal cations with vacant sp orbitals can also be used to tune the conduction band minimum (CBM) [93]. In addition to enhancing the optoelectronic properties of semiconductors, doping can impact the separation and transfer of photogenerated carriers positively or negatively. Introducing foreign particles, for instance, may impede the transmission and separation of photogenerated carriers by acting as sites for charge recombination or electron trapping. However, dopants present on the surface undoubtedly possess a greater capability to effectively separate photogenerated electron–hole pairs. This occurs because the limited electrons or holes in impurity surface states can readily interact with electron donors or acceptors within a photocatalytic system [94–98]. Phosphorus doping induces the formation of midgap state defects within the crystal structure of CZS nanorod (NR) photocatalysts, thereby generating an internal electric field. This electric field plays a crucial role in separating photogenerated charges, leading to enhanced photocatalytic hydrogen generation [6] as shown in Figure 5(a). In another case, phosphorus (P) was gradient-doped into a CdS photocatalyst, with the P concentration decreasing from the surface toward the interior. The hybridization of P 2p and S 2p orbitals resulted in an increase in the VB maximum in the regions doped with P. Additionally, the donor doping of phosphorus raised the Fermi level (E_f) [78]. After exposure to light, a homojunction can exhibit a band bending effect that creates a region resembling an anti-quantum well. Hence, the inherent directed electric field transported the photoexcited carriers from the interior to the exterior. The charge separation efficiency of a photocatalyst is significantly affected not only by the position of dopants, but also by the doping density on the surface of the photocatalyst [99,100]. According to the reported literature, the introduction of a small amount of Ni into CdS nanowires (CdS-NWS) can create short surface states because of

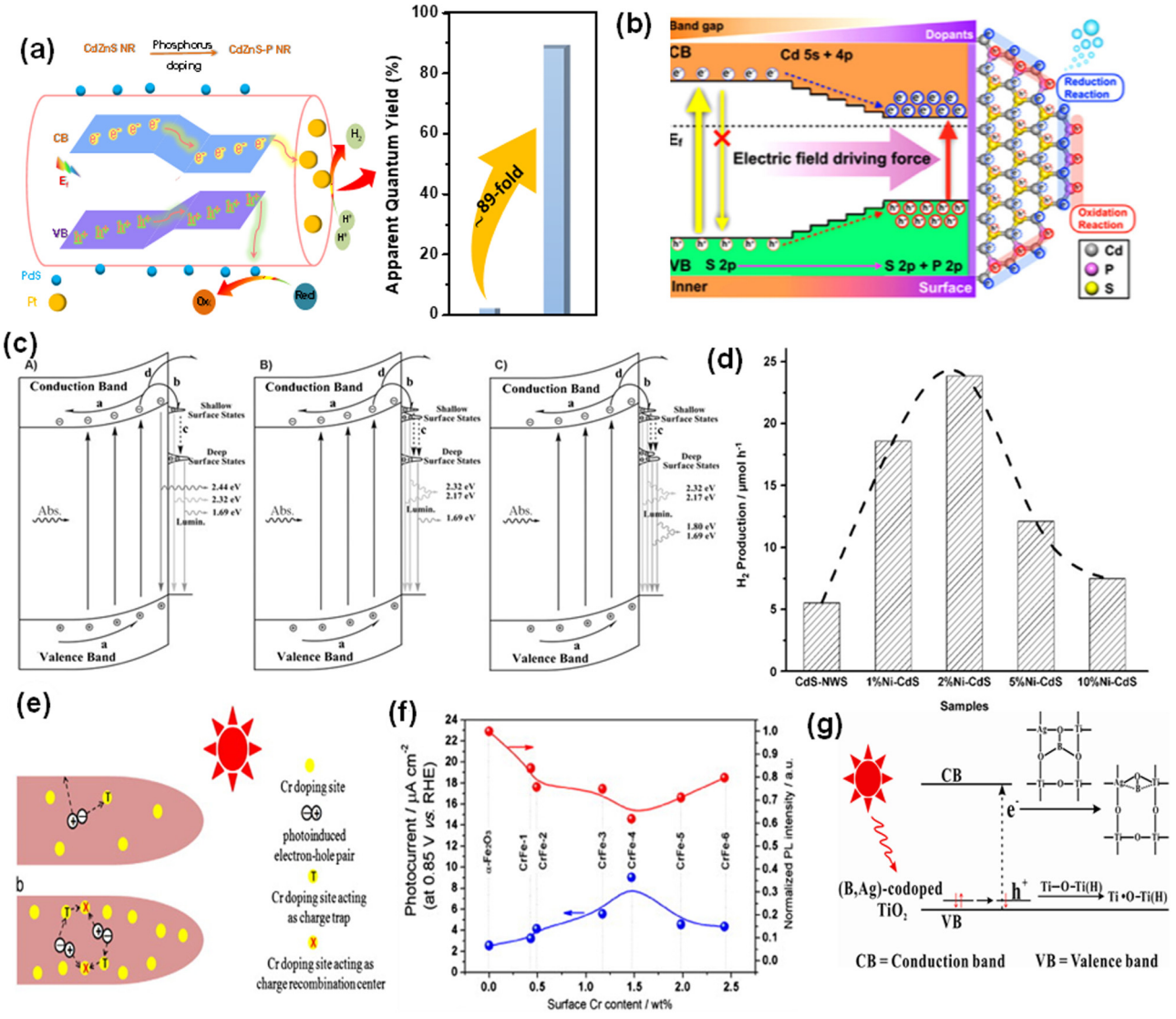

Figure 5: (a) and (b) Photocatalytic mechanism of photoinduced charges transport in pristine and P-doped samples, reused after permission from previous studies [6,78], (c) charge transfer mechanism in Ni/CdS NRs, (d) photocatalytic performance of CdS and Ni/CdS, reused after permission from Guo *et al.* [162], (e) graphical representation of charge transport Cr/Fe_2O_3 with various conc. of dopant, (f) I-T and PL intensity is directly influenced by dopant, reused after permission from Shen *et al.* [100], and (g) charge transfer mechanism in co-doped B, Al/TiO_2 (reused after permission from Feng *et al.* [101], Copyright 2013 American Chemical Society).

the existence of substituted Ni ions. On the other hand, a high concentration of Ni doping can lead to the formation of deeper surface states because of the existence of intervening Ni ions (Figure 5(c)). During photocatalysis, the photogenerated charges would be selectively captured by surface states that are close to the surfaces and will extend the duration of the photogenerated charge carriers which will affect the photocatalytic hydrogen production. In contrast, the presence of deep surface states facilitated the recombination of photogenerated charge carriers. The photocatalytic hydrogen (H_2) production by Ni-doped CdS exhibited an initial enhancement followed by a decrease as the Ni doping level increased. The greatest production rate was achieved at an Ni doping level of 2% (Figure 5(d)). Comparable correlation between the amount of doping and the behavior of charge separation in arrays of NRs made of α-Fe_2O_3 with Cr doping was reported in a previous study as shown in Figure 5(e) [100]. At a low concentration of Cr dopant, the photogenerated electrons were captured by the Cr dopant sites, while the holes were able to move to the surface freely, play a key role in charge separation. However, in case of higher concentration of Cr, numerous electron trapping sites were created which were acting as charge recombination caters instead of charge separation. The photocurrents exhibited a direct correlation with the

amount of Cr dopant, reaching an ideal level at 1.47 wt% (Figure 5(f)). This implies that it is worthwhile to maintain a moderate level of surface Cr doping in order to optimize the effectiveness of charge separation. Moreover, the charge separation in photocatalysts can be further improved by the combined effect of various dopants [100–102]. Deng *et al.* explored co-doping TiO_2 with boron (B) and silver (Ag) to create boron and silver units. These units act as electron traps, capturing photogenerated electrons upon light exposure and forming transitional structures (Figure 5(g)). This trapping process enhances the separation of electron–hole pairs, extending the lifetime of these charge carriers and ultimately leading to improved photocatalytic performance.

3.1.1 Doping

Doping offers a transformative approach for engineering photocatalysts with superior optoelectronic properties. By overcoming the existing challenges and harnessing the power of this technique, we can create a brighter future for photocatalytic hydrogen production, contributing to a cleaner and more sustainable energy landscape. Besides, there are still some challenges, which should be addressed: (1) Selecting the optimal dopant material and concentration is crucial for achieving the desired effects without introducing detrimental side effects. (2) Dopants can sometimes migrate or deactivate over time, leading to a decline in photocatalytic activity. Developing stable doping strategies is crucial for long-term performance.

3.2 Crystal engineering induced charge separation for hydrogen evolution

Crystal engineering is a field within materials science dedicated to creating new solid-state materials with distinctive properties. This is accomplished by meticulously regulating and modifying the supramolecular and microscopic arrangement of the materials' constituent parts [103–105]. The properties of a material are affected by the way molecules and ions are arranged in the solid state, which may be understood and controlled using chemical concepts and methods. Crystal engineering may change the phases, orientation, and visibility of facets to provide better photocatalytic capabilities. Crystal engineering provides a promising approach to tailor the properties of photoexcited charge separation on crystalline semiconductor photocatalysts. This method allows precise manipulation of the crystallographic structure of photocatalysts at both nano- and microscales, offering versatile control over their characteristics. This allows certain aspects to be shown in a manner that is both desirable and logical. Variations in the coordination environments and surface atom arrangements at different facets of particulate semiconductors influence their reactivity. Facets with higher surface energy, such as the (001) facet in TiO_2, are typically more reactive due to unsaturated bonds and dangling atoms, serving as active sites for chemical reactions and enhancing photocatalytic activity. In contrast, more stable facets like the (101) facet are less reactive and contribute to the semiconductor's stability and durability. Different facets exhibit distinct properties, including surface energy, electronic structure, charge separation and transport, catalytic activity, and stability. Understanding and controlling these facet-dependent properties is crucial for optimizing semiconductor performance in photocatalysis, photovoltaics, and electronic devices [106]. The results of the selected area electron diffraction analysis in Figure 6(a)–(d) demonstrate that the Rh/Cr_2O_3 cocatalyst, which is deposited on the (100) facets that attract electrons, acts as a cocatalyst for reduction in the evolution of hydrogen. On the other hand, hole transmission is facilitated by the CoOOH cocatalyst, which is mostly loaded on the (110) facets and nearby facets that collect holes. It is believed that the charge separation action inside the photocatalyst particle causes the growth of heterogeneous cocatalysts on opposite sides of the $SrTiO_3$ particle. The occurrence can be explained by the built-in electric field that arises from the contrasting work functions of the opposing sides. The charges produced by light can undergo multiple consecutive separations and transfers in the forward direction without any loss or recombination in the opposite direction. Achieving this goal involves employing various methods: introducing aluminum to minimize flaws, applying flux treatments to enhance crystal quality, engineering specific facets while incorporating highly efficient cocatalysts, and enveloping with a Cr_2O_3 shell to inhibit undesired reverse reactions. The interplay of several techniques demonstrates the need of meticulous control over many processes to achieve OWS with a high AQE (Table 1).

Li *et al.* performed a series of studies on the spatial separation of photogenerated electrons and holes between the (010) and (110) crystal facets of $BiVO_4$. They used different redox cocatalysts to know about the propagation of electrons along various facets of the $BiVO_4$ as shown in Figure 6(e)–(j) [161]. This allowed them to see the impact of the inherent electric field on the transfer of charges [161]. These efforts provide a chance to enhance the efficiency of photocatalysts by using the phenomenon of charge separation among distinct crystal facets. In 2020, Li *et al.* introduced and tested the hybrid flow battery (HFP) approach for solar hydrogen generation using

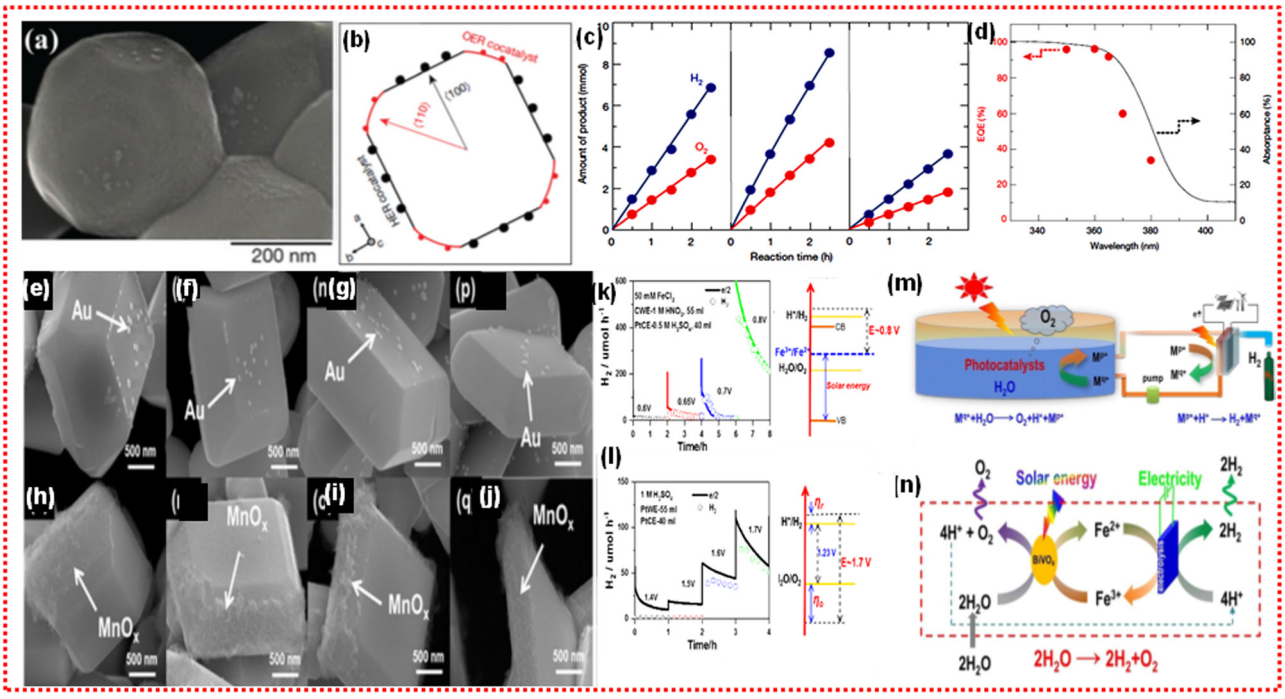

Figure 6: (a) SEM of Al-$SrTiO_3$, photodeposition of various cocatalysts, (b) orientation of the crystal determined by SAED pattern. (c) Time course of photocatalytic performances of Al-$SrTiO_3$. (d) UV spectrum of untreated $SrTiO_3$ Al is shown by the black solid line, while the red symbols indicate the wavelength dependency of the EQE = (Collected photocurrent)/(Incident optical power) * (hc/λ) in splitting of water on Al-doped $SrTiO_3$ in the presence of Rh/Cr_2O_3/CoOOH. Reproduced with permission of Takata *et al.* [163]. Springer Nature, Copyright 2020. (e)–(j) Spatial separation of redox cocatalysts on anisotropic facets of $BiVO_4$. (k) and (l) This study compares the process of water splitting using an integrated system with electrolysis. The energy graphs for the two systems are also shown with the response curves. The symbol e/2 denotes the theoretical rate of hydrogen (H_2) generation, which is determined based on the current conditions. (m) Scalable solar hydrogen generation in the presence of $BiVO_4$ and shuttle ion loop for energy storage. (n) The implementation of HFP, a photocatalyst for water oxidation, Fe^{3+}/Fe^{2+} as shuttle ions for energy storage, and an electrolysis cell for hydrogen generation. Reproduced from [161], Copyright 2020 by Wiley-VCH Verlag GmbH & Co.

particulate photocatalysts. By using the Z-scheme architecture to physically isolate the water oxidation process from the proton reduction reaction, this approach may prevent the undesirable reverse reaction of hydrogen and oxygen, hence ensuring the secure generation of these substances. The solar conversion efficiency of $BiVO_4$ crystals for HFP was enhanced by accurately controlling the exposure ratio of various facets involved in oxidation and reduction processes. An electrolysis cell was used to produce hydrogen with almost perfect Faraday efficiency, reaching almost 100%, by applying a bias of around 0.80 V. This voltage level is equivalent to the chemical potential of the Fe^{3+}/Fe^{2+} shuttle, as shown in Figure 6(k) and (l) [161].

It is crucial to note that achieving a minimum bias of 1.7 Vin is essential for water electrolysis within the same setup, given the primary hurdle posed by the significant overpotential needed for water oxidation. The solar-to-chemical energy conversion efficiency in this HFP configuration stands at 1.97%. The overpotential necessary for electrolysis, using the Fe^{3+}/Fe^{2+} shuttle, approximates 0.03 V. Furthermore, the process demonstrates a Faraday efficiency of 100 at% 0.8 V. Based on these metrics, the STH-energy-conversion efficiency is estimated to be 1.85%. This study proposes a viable approach to solar energy storage through a redox shuttle ion loop. This strategy involves two interconnected subsystems: one efficiently utilizes photocatalytic water oxidation to store solar energy and generate protons, while the other utilizes these protons to produce H_2, as depicted in Figure 6(m). Their findings indicate that $BiVO_4$ particulate photocatalyst crystals effectively address the challenges mentioned earlier, serving as efficient catalysts for water oxidation. This enables the HFP system to store solar energy and produce hydrogen (Figure 6(n)). By precisely tuning the (110) and (010) facets of $BiVO_4$ crystals, the AQE for photocatalytic water oxidation can exceed 71% when utilizing Fe^{3+} as an electron acceptor. Furthermore, the conversion of Fe^{2+} to Fe^{3+} is completely suppressed. This approach can achieve a total solar-to-energy conversion efficiency exceeding 1.9% and an STH efficiency of 1.8%. They propose a practical solar

Table 1: Most recent representative doping induced charge separation boosting solar-driven hydrogen production

Photocatalysts	Absorption range	H_2 production rate	AQE = $\frac{2 \times N \times H2}{N_{photons}} \times 100$	Ref.
B-doped C_3N_4/ZnO	350–450 nm	2.9 times higher/357 μmol g^{-1} h^{-1} full spectrum	3.29% full spectrum	[107]
Mo-CdS NRs	480–550 nm	5.8 times higher/14.62 mmol g^{-1} h^{-1}	20.5 at% 420 nm	[108]
N-doped $ZnIn_2S_4$	250–500 nm	13.8-fold higher/11,086 μmol g^{-1} h^{-1}	~20 at% 400 nm	[109]
Cu-$ZnIn_2S_4$	350–500 nm	14.8 times higher/9.8647 mmol g^{-1} h^{-1}	37.1 at% 420 nm	[110]
Oxygen vacancy self-doping surface black TiO_2	400–600 nm	12-fold increase/660 μmol g^{-1} h^{-1}	13.4 at% 365 nm	[111]
Carbon self-doped g-C_3N_4	250–450 nm	4.5-folds increase/1,224 μmol g^{-1} h^{-1} at λ > 420 nm	—	[112]
(Ti^{3+}self-doped TiO_2 mesoporous NT/N-C-/Co nanoparticles)	300–450 nm	Four times higher/~3.9 μmol g^{-1} h^{-1} at λ > 420 nm	~6.12%	[113]
Nickel-doped-CInZnS	360–430 nm	Three times higher/~3035.75 μmol g^{-1} h^{-1} at λ > 420 nm		[114]
Ti_3C_2/N,S-TiO_2/g-C_3N_4	200–500 nm	495.06 μmol h^{-1} g^{-1} at λ > 420 nm		[115]
O-$ZnIn_2S_4$/TiO_{2-x}	200–400 nm	2584.9 μmol g^{-1} h^{-1} at λ > 420 nm		[116]
Pt/N-doped vanadium carbide/C_3N_4	250–450 nm	40 μmol h^{-1} g^{-1} at λ > 420 nm		[117]
Vanadium and lanthanum co-doped ZnO/CNTs	350–500 nm	Seven times higher/925 μmol g^{-1} h^{-1}		[118]
K-doped modified g-C_3N_4	350–450 nm	66.6 times higher/~59.9 mmol g^{-1} h^{-1}	57.1 at% 420 nm	[119]
Mo-CoS_x/g-C_3N_4	250–450 nm	~193 times higher/2062.4 μmol g^{-1} h^{-1}	11 at% 420 nm	[120]
Au-Cu decorated TiO_2/B-doped g-C_3N_4	250–450 nm	Three-fold higher/2,150 μmol g^{-1} h^{-1} λ > 420 nm		[121]
$ZnIn_2S_4$ nanosheets onto S-doped g-C_3N_4	250–500 nm	7.7 times higher/1.63 mmol g^{-1} h^{-1} $\lambda \geq 420$ nm		[122]
Ca-modified CoP_x@CdS	400–550 nm	2441.5 μmol h^{-1}	35.4 at% 420 nm	[123]
P- (Cu−Zn−In−S)	350–550 nm	3.5-fold higher/12.2 mmol g^{-1} h^{-1}	5.24 at% 404 nm	[124]
N-doped Ti_3C_2 MXene quantum dots/1D CdS NRs	250–520 nm	14.79 times higher/17,094 μmol g^{-1} h^{-1} $\lambda \geq 420$ nm		[125]
Fluorine (F)-doped Ruddlesden-Popper Sr_2TiO_4 perovskites ($Sr_2TiO_{3.97}F_{0.03}$)	250–360 nm	Two times higher/282 μmol g^{-1} h^{-1} $\lambda \geq 250$ nm		[126]
Cu-doped ZnS nanoframe	200–450 nm	8.30 mmol g^{-1} h^{-1} full spectrum		[127]
FeCo doped-MoS_2 loaded CdS	200–500 nm	58-fold higher/350 μmol h^{-1}	52 at% 425 nm	[128]
Ni, In co-doped $ZnIn_2S_4$	200–500 nm	3.6 times higher/21.94 μmol h^{-1}	0.14 at% 400 nm	[129]
Bi doped $Zn_{0.5}Cd_{0.5}S$	350–450 nm	Four times higher/1.09 mmol/h	31.5 at% 420 nm	[130]
N-doped C layer with TiO_2/$ZnIn_2S_4$	200–500 nm	12.1 times higher/2.8 mmol g^{-1} h^{-1}	1.3 at% 400 nm	[131]
(Ni-H/T-CCN)	350–500 nm	5.8 times higher/4,933 μmol g^{-1} h^{-1},	7.8 at% 420 nm	[132]
Bi^{3+}-doped $Ce_2Ti_2O_7$/$ZnIn_2S_4$	200–550 nm	7.6 times higher/833.7 μmol g^{-1} h^{-1}, λ	1.9 at% 420 nm	[133]
B and S co-doped g-C_3N_4 nanotubes	200–500 nm	2.3 times higher/93.21 μmol g^{-1} h^{-1},	5.3 at% 420 nm	[134]
2D/2D Cu-doped In_2S_3/CdS	200–600 nm	1.6 times higher/863.66 μmol g^{-1} h^{-1},	8.3 at% 420 nm	[135]
Fe-doped $LaMnO_3$	200–650 nm	2.5 times higher/767.71 μmol g^{-1} h^{-1}, full spectrum		[136]
FeCoSe/$CdS_{0.95}Se_{0.05}$	200–550 nm	Two times higher/513.76 μmol h^{-1}, $\lambda \geq 420$ nm		[137]
S-g-C_3N_4 nanosheets	200–600 nm	~Two times higher/17.46 μmol g^{-1} h^{-1},	17.7 at% 420 nm	[138]
N, P-co-doped carbon anchored on ZnO NR	300–500 nm	417 μmol g^{-1} h^{-1}, $\lambda \geq 410$		[139]
Eu-doped g-C_3N_4	300–500 nm	117.1-fold higher/128.8 μmol g^{-1} h^{-1}, $\lambda \geq 410$		[140]
S-doped g-C_3N_4	300–500 nm	22.04 mmol g^{-1} h^{-1}	7.8 at% 420 nm	[141]
Defective, sulfur self-doped g-C_3N_4 nanofiber	200–500 nm	2.84-fold higher/632 μmol h^{-1} g, $\lambda \geq 410$		[142]
V, S co-doped Ta_3N_5 (polyaniline) layer	200–900 nm	3.8-fold higher/98.4 mmol g^{-1} h^{-1}, full spectrum		[143]
N-doped Fe_3C nanocages $ZnIn_2S_4$	200–500 nm	9,600 μmol g^{-1} h^{-1},	3.6 at% 425 nm	[144]
Black phosphorous doped C_3N_4 with benzene ring	300–550 nm	Four times higher/860 μmol g^{-1} h^{-1},	4.31 at% 420 nm	[145]

(Continued)

Table 1: *Continued*

Photocatalysts	Absorption range	H_2 production rate	AQE = $\frac{2 \times N \times H2}{N_{photons}} \times 100$	Ref.
S-doped CdO@In_2O_3 nanofiber	200–700 nm	~22.0-fold higher/4564.58 μmol g^{-1} h^{-1}		[146]
P-doped $ZnIn_2S_4$	300–600 nm	3.8 times higher/1566.6 μmol g^{-1} h^{-1}		[147]
In situ protonated P-interstitial-doping of g-C_3N_4	350–450 nm	Eight-fold higher/6,323 μmol g^{-1}	5.08 at% 420 nm	[148]
Cd-Cu co-doping on ZnS (CdS/CuS/ZnS)	380–720 nm	6401.06 μmol g^{-1} h^{-1},	38.3 at% 425 nm	[149]
N-doped graphene quantum dots g-C_3N_4	220–700 nm	1,248 μmol g^{-1} h^{-1}	11.5 at% 405 nm	[150]
Carbon-coated Cu- doped $ZnIn_2S_4$	200–650 nm	1455.98 μmol g^{-1} h^{-1}		[151]
Ag-doped N- vacancy-rich g-C_3N_4	350–500 nm	1.69 mmol g^{-1} h^{-1}		[152]
Ultrathin oxygen-doped g-C_3N_4/mesoporous nickel hydroxide	300–550 nm	4.7 times greater/4764.9 μmol g^{-1} h^{-1}	7.74 at% 420 nm	[153]
Pd nanoparticles anchored/carbon atom self-doped g-C_3N_4	200–600 nm	24.1 mmol g^{-1} h^{-1}	17.1 at% 400 nm	[154]
Ni-doped CdS	400–600 nm	119 times higher/1644.6 μmol g^{-1} h^{-1}	19.2 at% 450 nm	[155]
Pyrimidine-doped g-C_3N_4	200–500 nm	4.41 times higher/453 μmol g^{-1} h^{-1}	4.27 at% 420 nm	[156]
P-doped CdS	300–750 nm	11.7-fold higher/9.58 mmol g^{-1} h^{-1}	4.12 at% 420 nm	[157]
Co-doped $CsPbBr_3$ under the magnetic field of 2 T	300–750 nm	3.14 times higher/1828.36 μmol g^{-1} h^{-1}		[158]
C, N-defects and oxygen-doped g-C_3N_4 in 10% triethanolamine with 1% Pt as cocatalyst	300–550 nm	6.7 times higher/18.95 mmol g^{-1} h^{-1}	29.6 at% 420 nm	[159]
S-doped C-vacancy with honeycomb g-C_3N_4 nanosheets	300–650 nm	21.8 times higher/23.78 mmol g^{-1} h^{-1}	8.5 at% 430 nm	[160]

energy storage method involving a redox shuttle ion loop with two interconnected subsystems. The first subsystem employs highly efficient photocatalysis for water oxidation, facilitating solar energy storage and proton generation. The second subsystem utilizes these protons for hydrogen production.

3.2.1 Crystal engineering

In this section, crystal engineering for charge separation in photocatalytic hydrogen production is discussed systematically. Crystal engineering offers several advantages for enhancing charge separation in photocatalyst. By modifying band positions and introducing new energy levels, crystal engineering can create more efficient pathways for charge separation and transport. Controlled defect engineering can minimize recombination centers within the crystal lattice, allowing more charges to participate in hydrogen evolution reactions (HERs). Tailored crystal structures can enhance the mobility of photogenerated charges, ensuring they reach the surface for hydrogen production efficiently. Besides, there are still some problems to be solved for boosting charge separation.

(1) Achieving the desired crystal structure is often a complex process. Factors like dopant concentration, temperature, and pressure require careful control to ensure the intended effects.
(2) Scaling up crystal engineering techniques for large-scale production can be difficult and expensive. Developing cost-effective and scalable methods is crucial for practical applications.
(3) Accurately characterizing the complex atomic arrangement and defect structures of engineered crystals is essential for understanding their behavior and optimizing future designs. Advanced characterization tools are needed.
(4) Refining computational models to accurately predict the effects of crystal engineering on a material's properties will significantly accelerate the development of optimized photocatalysts.

3.3 Surface phase junction engineering for boosting charge separation

Surface-phase junctions are created by using polymorphism in semiconductors with distinct crystalline phases of the same semiconductor, a commonly used method to improve photoexcited charge carriers. Although semiconductors with an identical chemical profile may have distinct crystal shapes due to variable conditions at different stages of crystallization, properties related to the physical and chemical characteristics of a substance. For example, substantial research has been conducted on TiO_2 with various phase structures, such as anatase, brookite, and rutile. Surprisingly the sample containing a combination of rutile and anatase exhibits an enhanced activity, as opposed to a sample consisting of just one component. To ascertain the influence of various crystalline forms in photocatalytic performances, researchers thoroughly investigated their photocatalytic capabilities and the phase transition of rutile and anatase TiO_2 in both the bulk and surface areas [108].

Figure 7(a) shows the process of producing H_2 by photocatalysis on TiO_2. The different proportions of the two phases of TiO_2 are strongly linked to their surface-phase engineering. The TiO_2 with a combination of rutile and anatase phases exhibits the best performances. These two phases were conformed through high-resolution transmission electron microscopy (HRTEM) characterization as shown in Figure 7(b), which showed that the mixture comprised the two phases of TiO_2. Beside TiO_2 another photocatalyst gallium oxide (Ga_2O_3) having tunable a–b phase junction as shown in Figure 7(c), which have the same trend as shown by polymorphs of TiO_2. These mixed phases of gallium oxide displayed an improved performance relative to its pure phase as shown in Figure 7(d). An HRTEM technique revealed the presence of a surface phase junction at the atomic level. This junction exhibited a uniform and tightly packed junction between the two phased a and b of Ga_2O_3. The performance of Ga_2O_3 can be significantly enhanced by introducing an a–b phase junction, resulting in an increase of over eight times compared to the single phase. The recombination and trapping processes inside the corresponding phases are much slower than the very quick electron transport process (~3–6 ps) that occurs when the a–b phase junction is present. Additionally, the lifespan of photoinduced electrons in a–b Ga_2O_3 is noticeably longer than in any individual phase during the microsecond timeframe. This is the reason behind the improved activity of photocatalytic water splitting. Furthermore, it has been demonstrated that the strain and lattice misfit at the interface junctions can effectively adjust the energy bands [164]. The photogenerated charge separation thermodynamically was demonstrated by a type-II band alignment, with a larger VB of 0.35 eV for a-Ga_2O_3 compared to b-Ga_2O_3, and a CB offset of 0.07 eV as shown in Figure 7(e). So far, numerous reports on heterogeneous photocatalysts rely on the surface phase junction, such as hexagonal/cubic CdS [165].

3.3.1 Surface phase junction

In this section, the significance of surface phase junction for efficient charge separation are systematically discussed. By creating interfaces within a material or between different materials, this technique facilitates the separation of light-generated electrons and holes. This separation is crucial because recombining charges significantly hinder hydrogen production. By creating internal electric fields or spatial separation within the material, phase junctions direct electrons and holes to specific locations, preventing them from recombining before they can participate in the HER. Tailored phase junctions can also optimize light absorption by promoting the absorption of a wider range of wavelengths. Besides this, there are some challenges, which should be overcome for the effective charge separation for photocatalytic hydrogen production. To form well-defined and stable phase junctions at the surface, it is essential to carefully control the synthesis conditions. Ensuring optimal band alignment and efficient charge transfer across different phases within a junction remains a challenge. Maintaining the integrity and functionality of the phase junction under prolonged reaction conditions can be difficult.

3.4 Dual-cocatalysts induced driving force for charge separation

The efficiency of charge separation becomes a crucial factor in determining the photocatalytic efficacy when electron–hole pairs are generated. It is crucial to evaluate both the oxidation and reduction half processes in the photocatalytic OWS reaction, as it involves redox reaction. The slowest step of the half-cell reaction is the rate determining step of the overall reaction. It is well known that fabrication of dual cocatalyst significantly increases their photocatalytic performances of the photocatalysts as shown in Figure 8(a) [167]. The incorporation of Pt and PdS cocatalysts has dramatically boosted the photocatalytic performance of the CdSe photocatalyst for hydrogen generation. By co-loading Pt and PdS onto CdSe, the photocatalytic activity surged over 500-fold, achieving an astonishing AQE of 45 at% at 420 nm. This significant enhancement is attributed to the simultaneous acceleration of both the oxidation and reduction half-reactions. PdS notably amplifies sulfite oxidation, while Pt excels in proton reduction, collectively driving the photocatalytic process to unprecedented levels of efficiency. GaN:ZnO exhibits promising photocatalytic activity for the OWS reaction under visible

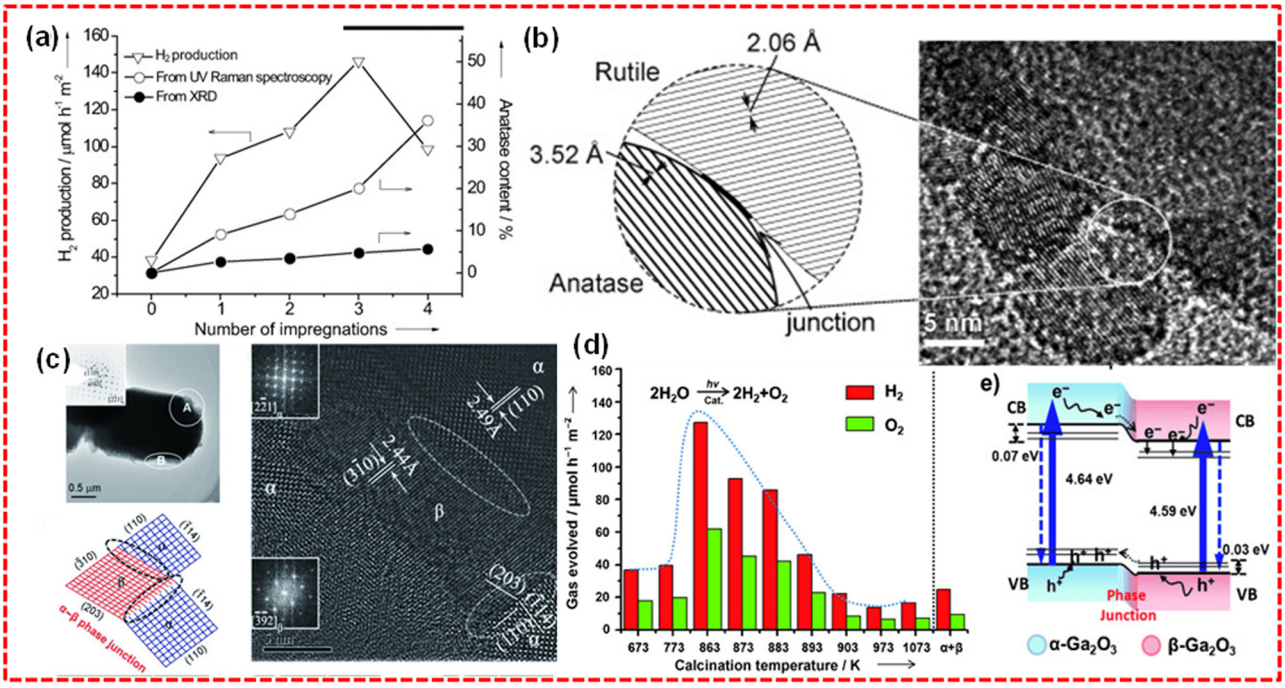

Figure 7: (a) Anatase and rutile photocatalytic H_2 evolution performance. (b) HRTEM was used to examine the surface phase junction that was created between anatase and rutile. Reproduced with permission from Zhang *et al.* [166], Copyright of Wiley-VCH Verlag GmbH & Co 2008. (c) Low-magnification image of Ga_2O_3. (d) Photocatalytic water splitting. (e) Diagram showing the flow of charge *via* the a–b phase junction [105], Copyright 2012 Wiley-VCH Verlag GmbH & Co.

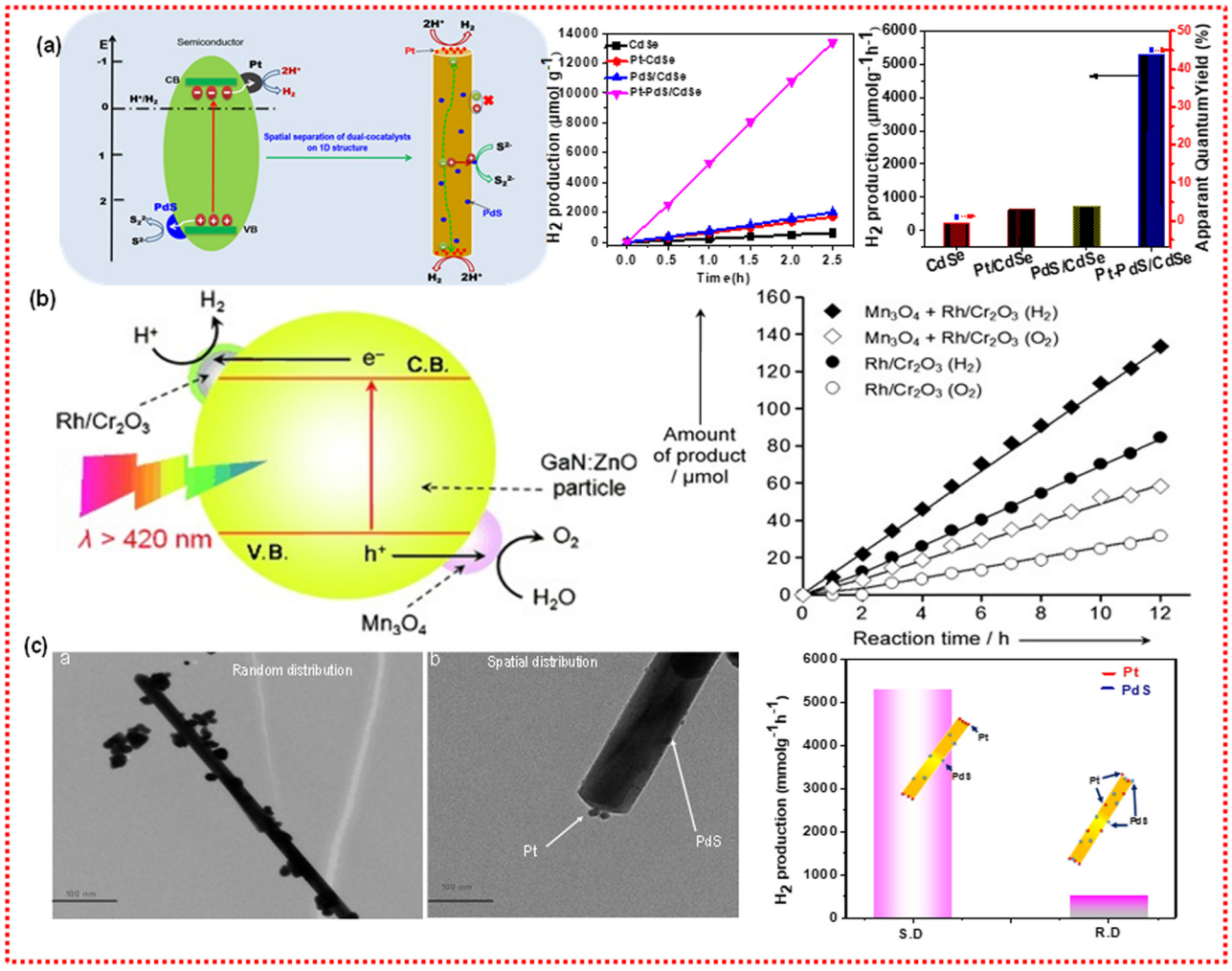

Figure 8: (a) Scheme of the proposed mechanism for photocatalytic hydrogen production on one-dimensional CdSe NRs with spatial separation of dual-cocatalysts. Photocatalytic H_2 evolution and apparent quantum yield under visible light irradiation over CdSe, Pt/CdSe, PdS/CdSe, and Pt-PdS/CdSe. Reused from the study of Khan *et al.* [167] after getting permission from RSC Copyright 2019. (b) Cr_2O_3-Mn_3O_4/GaN:ZnO. Reused from the study of Maeda *et al.* [168], Copyright 2010 Wiley-VCH Verlag GmbH & Co. (c) TEM image of CdSe NRs with random and spatial deposition of Pt and PdS by impregnation and photodeposition methods. Comparative H_2 production of CdSe NRs and nanoparticles (NPs), S.D. means selective deposition and R.D. means random deposition: catalyst, 100 mg; 0.1 M Na_2S-Na_2SO_3 aqueous solution (100 mL); light source: Xe lamp (300 W) with an optical filter (λ > 420 nm). Reproduced with permission from Khan *et al.* [167] with permission from RSC Copyright 2019.

light irradiation. Research suggests that co-loading the GaN:ZnO photocatalyst with Rh/Cr_2O_3 as an HER cocatalyst and Mn_3O_4 as an oxygen evolution reaction (OER) cocatalyst significantly enhances its OWS activity, as demonstrated in Figure 8(b) [168]. The use of dual-cocatalyst is extensively acknowledged and utilized due to its synergistic impact on redox reaction. This approach has significant promise in the development and production of semiconductor materials [169]. Incorrect placement of deposition sites can lead to significant charge recombination, such as the presence of reducing cocatalysts on sites that accumulate holes and oxidizing cocatalysts on sites that accumulate electrons. Typically, when cocatalysts are deposited by the impregnation or adsorption approach, they are simply distributed randomly on the surface of the semiconductor materials. Nevertheless, considering the selective charge propagation among the various surfaces of photocatalyst, it is logical to deliberately design the oxidation and reduction cocatalysts on different surfaces of the semiconductor, respectively, to fully exploit the benefits of dual-cocatalysts. Figure 8(c) displays that the dual cocatalysts Pt and PdS were loaded randomly through impregnation method on the surface of semiconductor CdSe NRs, the activity instead of increasing decreased. On the contrary, when Pt and PdS were selectively deposited on the surfaces of CdSe NRs, the photocatalytic performance was highly improved, representing the extraordinary synergetic effect of the dual-cocatalyst. In the above example, the photocatalysts

effectively captured and confined the photogenerated electrons and holes using reduction and oxidation cocatalysts located on different facets of the photocatalysts. This spatial segregation enables the separate occurrence of oxidation and reduction half-reactions, greatly reducing the recombination process of photogenerated charges.

It is important to consider the changes in the dual cocatalyst species throughout photocatalytic processes. This is because the high-energy charges produced by photocatalysts can take part in surface reactions with specific reactants and contribute to the potential rebuilding or automatic optimization of dual photocatalysts [170,171]. Sodium tantalate ($NaTaO_3$) photocatalyst, as shown in Figure 9(a) and (b), possesses a nano-step framework that allows for the separation of the H_2 and O_2 evolution reaction sites. Specifically, H_2 is produced on NiO particles located on the border locations of $NaTaO_3$, whereas O_2 formation takes place at the depression locations of the $NaTaO_3$ particles [172]. Nevertheless, it has been documented that the metallic Ni and NiO cocatalysts are formed *in situ* on the $NiO_x/NaTaO_3$ photocatalyst throughout the photo-catalytic procedure. This was confirmed by the use of photoelectron X-ray and synchrotron X-ray absorption spectroscopy, as depicted in Figure 9(c)–(e) [173].

It was discovered that at the initial stage of the reaction, the cocatalyst NiO is the first to receive electrons generated by light and undergoes partial reduction to form metallic Ni. This phenomenon can explain the initial production of H_2 and O_2 in a nonstoichiometric manner. With an increase in irradiation time, the quantities of unaltered NiO and converted Ni on the surface of $NaTaO_3$ eventually equalize, resulting in the production of H_2 and O_2 in a stoichiometric ratio. Therefore, nickel (Ni) in metallic form and nickel oxide (NiO) are the cocatalysts used in the OWS process on $NaTaO_3$. These cocatalysts function as the active sites for the HER and the OER, respectively. An analogous redox fluctuation among cocatalysts was also noted on alternative photocatalysts, including $SrTiO_3$ [174]. The *in situ* fluctuation in the redox reaction of the dual-cocatalyst revealed the subtle and intricate process that takes place during photocatalysis. Therefore, to fully understand the role of these intrinsic reactive sites in photocatalysis, careful recognition and classification of these sites are required.

3.4.1 Dual cocatalysts

In this section, the effect of dual cocatalysts in charge separation for photocatalytic hydrogen production was performed, where it facilitates efficient charge transfer, dual cocatalysts minimize the chances of electron–hole recombination within the photocatalyst, further enhancing overall performance. By providing dedicated pathways for both electrons and holes, dual cocatalysts significantly improve the efficiency of charge separation. This leads to

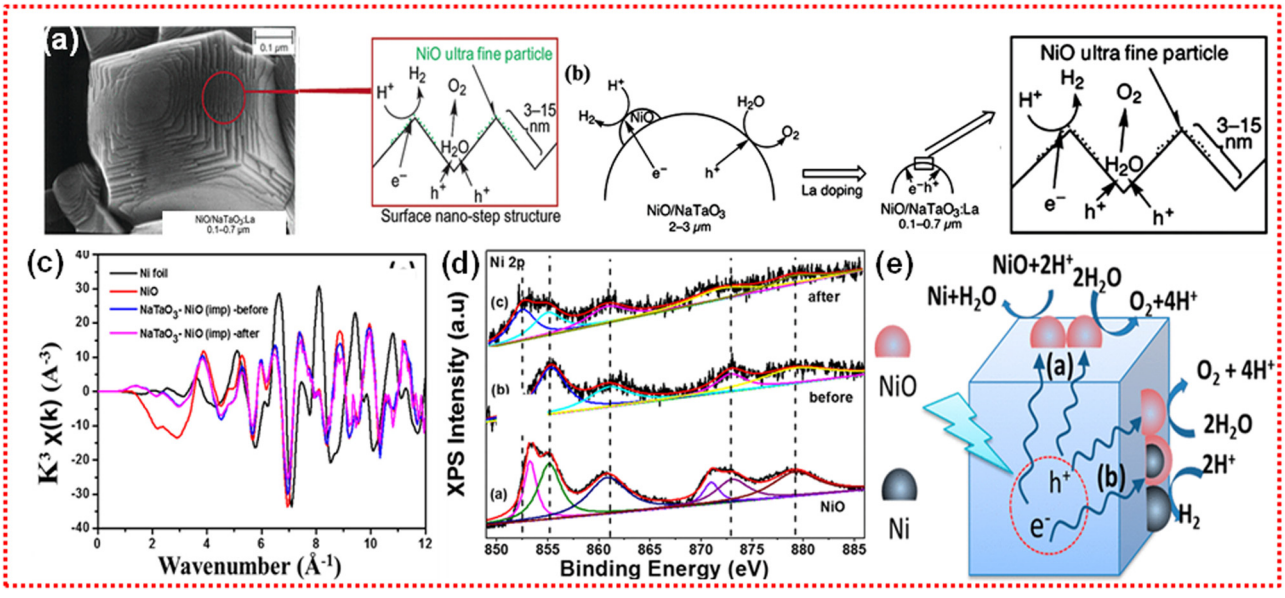

Figure 9: (a) SEM micrographs of 2% La loaded $NaTaO_3$. (b) Illustration of photocatalytic water splitting mechanism on particulate $NiO/NaTaO_3$. Reused from permission of ACS, Copyright 2003. (c) and (d) Spectroscopy characterization of NiO as cocatalyst over the surface of $NaTiO_3$ in light and dark, respectively. (e) Graphical illustration of the role of NiO as cocatalyst over $NaTiO_3$ [173], reused with the permission of ACS, Copyright 2016.

a greater number of charges available for the photocatalytic reactions. Besides their significance, there are some challenges to be considered. Finding the best dual-cocatalysts for a photocatalyst and target reaction is difficult. Catalytic activity, material compatibility, and band alignment are factors. Optimal performance requires uniform deposition and controlled distribution of dual cocatalysts on the photocatalyst. Unequal distribution can undermine functionality. Cocatalysts must function for long periods under reaction conditions. Cocatalyst degradation or deactivation reduces photocatalytic performance. Large-scale applications require cost-effective dual cocatalyst synthesis and depositing technologies.

3.4.2 Working principle of surface catalytic reaction

The reaction mechanism is a topic of ongoing discussion due to the complex and multifaceted nature of photocatalytic-based water-splitting processes. These reactions involve multiple steps and are influenced by various factors that are challenging to isolate and assess simultaneously. Consequently, there has been a significant increase in interest, both empirically and theoretically, in tracing the reaction intermediates and identifying the rate-determining stages to achieve a comprehensive understanding of the reaction processes [175–180]. Under acidic conditions, two potential pathways for the HER reaction have been hypothesized, as shown in equations (8)–(10). The initial step involves a photogenerated electron being accepted by the adsorbed and activated hydrated proton (H_3O^+) on the surface. This leads to the creation of a hydrogen atom that is absorbed and a molecule of H_2O. After absorbing another photogenerated electron and combining it with another activated hydrated proton, the adsorbed hydrogen atom releases H_2 and H_2O. The Volmer–Heyrovsky mechanism is the term used to describe this process. As an alternative, the Volmer–Tafel reaction produces hydrogen when two nearby adsorbed hydrogen atoms come together right after the activation and absorption stages.

$$H_3O^+ + e + *\rightarrow H^* + H_2O(\text{Volmer}), \quad (8)$$

$$H_3O^+ + e + H^* \rightarrow H_2 + H_2O + *\text{Heyrovsky}, \quad (9)$$

$$2H^* \rightarrow H_2 + 2*\text{Tafel}. \quad (10)$$

Typically, noble metals provide sites that can reduce protons. However, they can also provide reactive sites for oxygen and hydrogen production, which might result in the undesirable opposite reaction of forming water again. During photocatalytic OWS, the reverse reaction mostly involves the recombination of reactive hydrogen and oxygen to form water again as H_2 and O_2 into H_2O ($2H_2 + O_2 \rightarrow 2H_2O$). This reverse reaction can significantly reduce the photocatalytic activity and should thus be minimized. Nobel metals are usually used to prevent the reverse reaction and to create active sites in the form of single nanoparticles or core–shell nanoparticles which significantly increase the photocatalytic redox reactions [181–184]. In the case of zinc oxide and

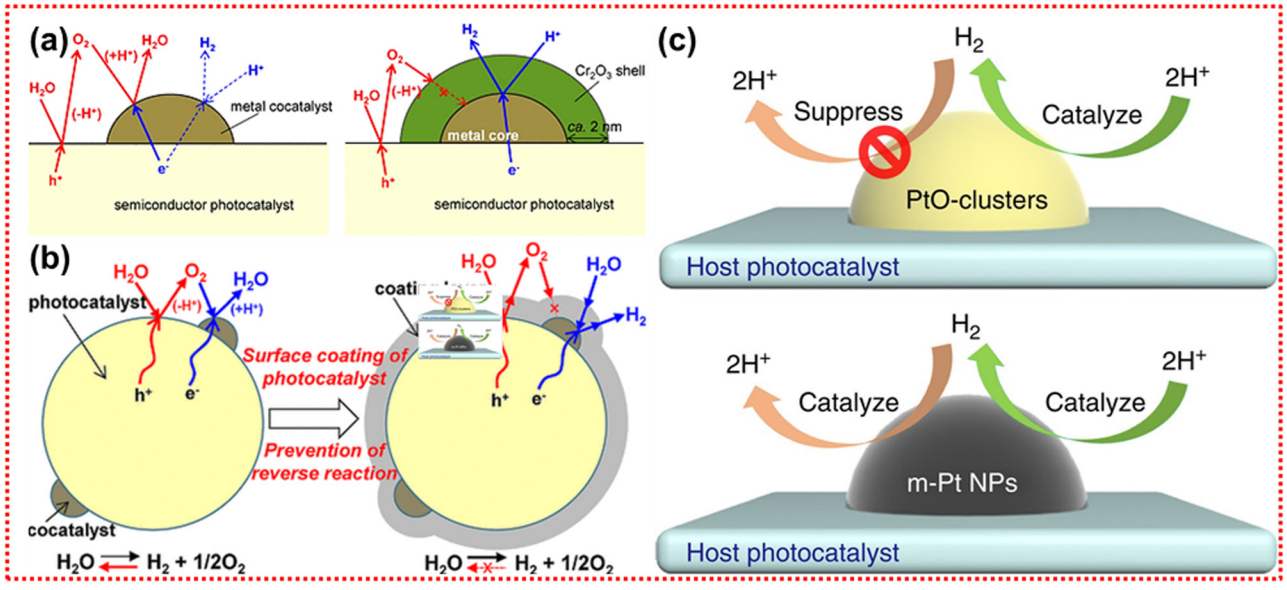

Figure 10: Diagrammatic representation of (a) shell function of Cr_2O_3 and (b) the layer composed of hydroxide of Nb, Ta, and Ti. Reproduced from the study of Takata *et al.* [182] with permission from the American Chemical Society, Copyright 2015. (c) Oxidized Pt and Pt nanoparticles are acting as H_2 generating cocatalysts. Pt which enhances the H_2 production and PtO stop the backward reaction. Reproduced from the study of Hang *et al.* [188] with permission from Springer, Copyright 2013.

gallium nitride photocatalysts, core-shell structures of the form M/Cr_2O_3 (where M = Rh, Pt, Pd, Ir, or other metals) were synthesized. This cocatalyst, as depicted in Figure 10(a), had a Cr_2O_3 coating that selectively allowed the passage of H^+ resulting in H_2, while blocking O_2 formation. This design effectively prevented the reverse reaction associated with oxygen molecules [182,185]. Furthermore, a protective layer consisting of metal titanium, tantalum, and niobium, oxy (hydroxide) and silicon oxyhydroxide was also created to provide a similar contribution to the semiconductor surface (Figure 10(b)) [186,187]. Besides, it has been observed that when Pt is in a higher oxidation state (specifically, PtO), it exhibits impressive suppression of the hydrogen oxidation reaction, yet its ability to generate hydrogen is still similar to that of the traditional metallic Pt cocatalyst, which serves as the benchmark. As shown in Figure 10(c) [188], the amorphous layer's malleability facilitates the transfer of oxygen from the inner region, where the oxygen partial pressure is higher, to the outer region, where the partial pressure is lower while inhibiting the opposite process. As a result, oxygen molecules are effectively blocked from reaching the activation sites, which inhibits the reverse reaction and promotes the OWS reaction. Equations (11)–(13) demonstrate the unique characteristics of the hydrogen evolution process within the alkali system.

$$H_2O + e + * \rightarrow H^* + OH^-, \tag{11}$$

$$H_2O + e + H^* \rightarrow H_2 + OH^- + *, \tag{12}$$

$$2H^* \rightarrow H_2 + 2*. \tag{13}$$

The OER is particularly challenging due to the necessity of a 4e–4e transfer. Explaining the kinetic process becomes difficult as a result, and it also makes it more difficult to explain the intermediates' geometric and electronic structures [189–191].

3.5 Hierarchical and core–shell morphology enhances charge separation

Nanostructures including micro/nanopores are commonly acknowledged to exhibit enhanced photocatalytic activity due to their larger specific surface areas, improved interfacial transfer of charges of reactant mass, and increased light absorption [192–194]. The presence of macroporous channels allows for efficient light harvesting and numerous reflections due to their ability to facilitate the movement of reactant mass and radiation. Core–shell and hierarchically organized porous materials possess a significant advantage in the field of photocatalysis for hydrogen evolution. This is due to the effective dispersion of active sites and their shorter diffusion routes. Several researchers have investigated the production of macro-mesoporous materials with hierarchical organization through the utilization of traditional template-directed techniques [195,196]. Wang *et al.* fabricated a structure resembling a "cauline leaf" to achieve a remarkably effective HER. This was accomplished by adorning TiO_2 nanofibers with perpendicular arrays of atomically thin MoS_2 nanosheets and CdS nanocrystals. The distinctive integrated design of the "cauline leaf" which is diagrammatically illustrated in Figure 11(a), and the synthesized hierarchal nanoarchitecture was characterized further through SEM, TEM, and HRTEM as shown in Figure 11(b). This hierarchal nanoarchitecture facilitated the capture and absorption of light, resulting in a highly efficient process of light harvesting and generation of photocarriers. Additionally, this design provided an unobstructed pathway for the rapid separation and transport of charges, thereby minimizing charge recombination. Furthermore, it offered a large surface area and a high concentration of active sites, enabling the efficient utilization of photo-generated carriers for the production of hydrogen through photocatalysis [197]. Similarly, Rao *et al.* prepared hierarchical nanostructures comprising TiO_2@NiO@ZnO supported on MXene, which showed outstanding photocatalytic hydrogen owing to the spatial distribution of charge carriers and photogenerated electrons and holes [198]. For the first time, Antonelli and Ying successfully synthesized mesoporous TiO_2 in 1995 [199]. Semiconductor materials possessing a mesoporous architecture have garnered significant interest due to their porous topology, which enables the efficient collection of photogenerated carriers over an extremely limited range. In addition, the mesoporous compounds have a large specific surface area, which means they have a greater number of active sites compared to their bulk equivalent. This leads to a high AQY = (Rate of product formation)/(Rate of photon absorption) for hydrogen generation. A wide variety of mesoporous oxides can be synthesized by the utilization of either a soft template or the nano casting approach employing a hard template [200]. A hierarchical hollow black $TiO_2/MoS_2/CdS$ simultaneous photocatalyst is devised and synthesized by Sun *et al.* This photocatalyst could absorb a wide range of wavelengths, resulting in improved hydrogen evolution performance. The composite photocatalyst's meso- and microporous characteristics are verified using N_2 sorption tests, as depicted in Figure 11(c). The adsorption–desorption data indicate the existence of evenly distributed, systematically arranged, cylindrical pores in the composite photocatalyst. Undoubtedly, the hollow b-TiO_2/MoS_2/CdS tandem heterojunction microspheres have a significantly superior H_2 production rate compared to the other photocatalysts as shown in Figure 11(d). The exceptional efficiency of photocatalytic hydrogen production can be due to the precise nanoscale design of the b-TiO_2/MoS_2/CdS tandem heterojunction. This integrated system

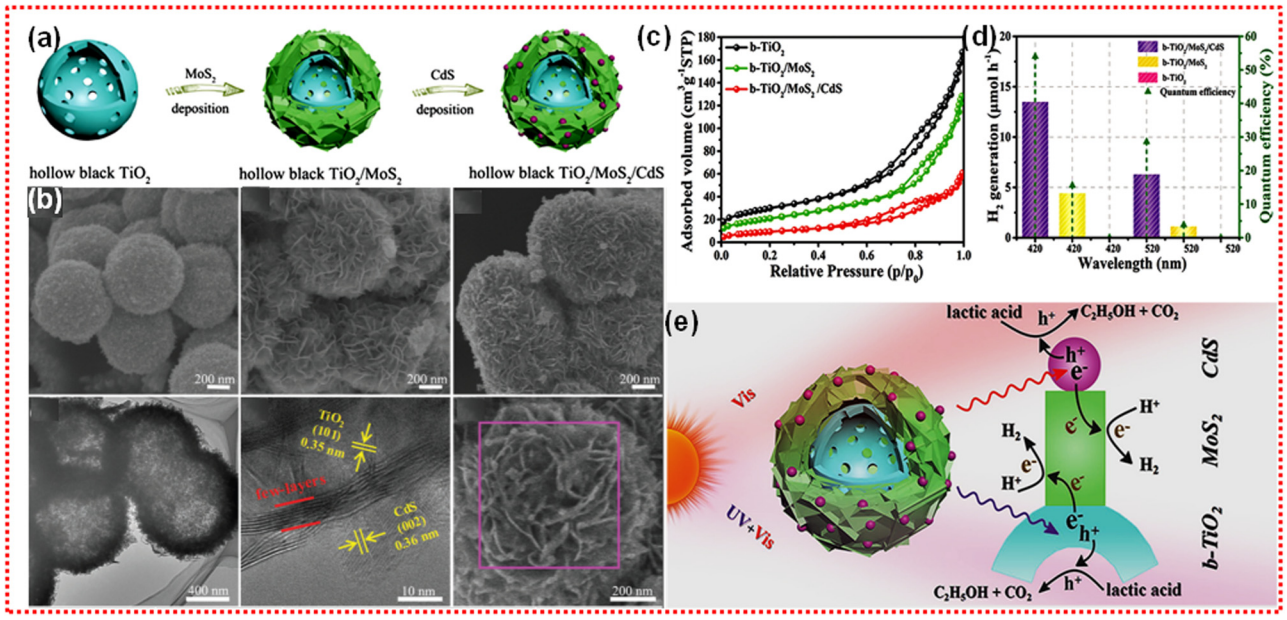

Figure 11: (a) Diagrammatic representation of the particulate b-TiO_2/MoS_2/CdS tandem heterojunction manufacturing process. (b) SEM, TEM, and HRTEM images of b-TiO_2/MoS_2/CdS microspheres. (c) Nitrogen sorption isotherms. (d) The photocatalytic hydrogen evolution rates under single-wavelength light and the corresponding AQE of b-TiO_2/MoS_2/CdS, b-TiO_2/MoS_2/CdS, and b-TiO_2, respectively. (e) Schematics of the tandem heterojunctions used for solar-driven water splitting. Adapted with permission from Sun *et al.* [201], Copyright 2018, John Wiley and Sons.

can convert solar energy into hydrogen with high efficiency across a wide range of the solar spectra, as depicted in Figure 11(e). The b-TiO_2/MoS_2/CdS tandem heterojunction could efficiently capture UV-Visible light from sunshine. Furthermore, the hollow structures have the capability to achieve numerous reflections within the enclosed space, hence enhancing light absorption. Additionally, they serve as a substrate with a large surface area for the vertical growth of MoS_2 nanosheets, maximizing the amount of exposed surface and edge sites. (ii) MoS_2 serves as a conduit, linking two compatible light-absorbing semiconductors to form a unified tandem system in b-TiO_2/MoS_2/CdS tandem heterojunctions. The presence of particulate tandem heterojunction structures, specifically TiO_2/MoS_2 and MoS_2/CdS, significantly enhances the process of charge separation from black TiO_2 and CdS to MoS_2 nanosheets. This enhancement successfully inhibits the recombination of electrons and holes. Electrons created by light were chemically interacted with protons on the surface of MoS_2 nanosheets to produce hydrogen. The photogenerated holes underwent a reaction with lactic acid at the VB of b-TiO_2 and CdS, respectively.

3.5.1 Section summary of hierarchical and core–shell structures

In this section, the benefits and challenges of hierarchical and core–shell morphologies are represented, which have proved to be a powerful approach to enhance charge separation within photocatalysts due to several factors, *i.e.*, it provides efficient pathways for charge transport, minimizing recombination. Core–shell designs create tailored interfaces between materials, promoting charge separation at these junctions. This combination ultimately leads to improved photocatalytic performance for applications like hydrogen production and environmental remediation. Some challenges are that complex structures often require multi-step fabrication. Synthesis methods must be simplified and scaled for real-world applications. Controlling the complex features and seamless core–shell interface is difficult. Poorly defined interfaces or structures can reduce their effectiveness. Compatibility between core and shell materials is crucial. Chemical or structural incompatibility can destabilize or hinder charge transfer. Optimizing shell thickness is crucial. Thick shells reduce light penetration to the core, while thin shells may hinder charge separation. Cost-effective production scaling is key to widespread adoption of this technology.

3.6 Defects engineering induced charge separation for H_2 production

Photocatalytic hydrogen generation works better when defects are used to help separate charges. The geometrical

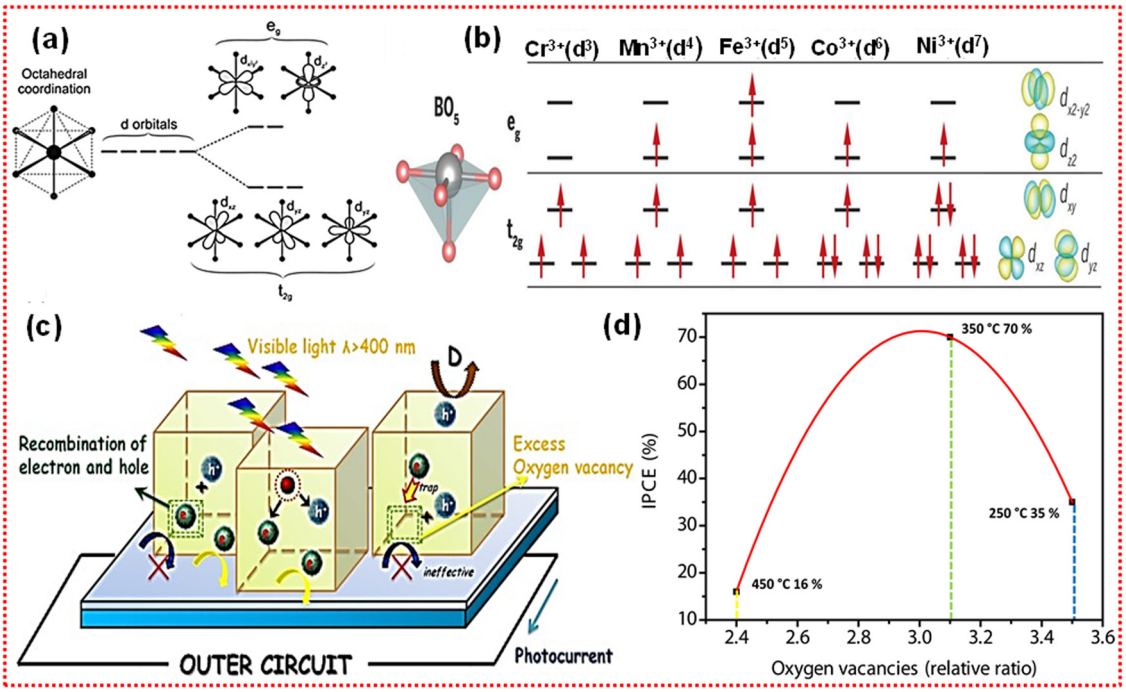

Figure 12: (a) splitting of d-orbital of transition metals. (b) Electronic configuration and pertinent metal orbitals of first-row transition metals for a BO_5 configuration, as well as orbital splitting of transition metal d orbitals. Reproduced with permission from AAAS [219]. (c) Diagram illustrating the effects of increased vacancies of oxygen on photogenerated electron transport in photoelectrochemical systems. (d) Plot of In_2O_3 nanotubes that were calcined in air at 250, 350, and 450°C to determine the optimal incident photon-to-electron conversion efficiency (IPCE) performance at the visible wavelength as a function of the comparative oxygen defects concentration. Reproduced with permission from Gan *et al.* [219], Copyright 2013.

characteristics, electronic structure, and atom coordination number of photocatalysts can all be altered by purposeful modification of the manufacturing processes. Surface reactions, charge carrier mobility and separation, and light absorption could all benefit from this modification. Following defect engineering, the types of ion losses in photocatalysts can be classified into three categories: anion vacancies, cation vacancies, and multi (anion and cation) vacancies. This section gives a summary of the various types of point defects that can be found in photocatalysts and how they can help with the photocatalytic water-splitting process.

3.6.1 Anion defects (oxygen defect) charge separation for H_2 production

Irrespective of achieving a flawless combination, imperfections of different sizes (such as 3D-0D) consistently disturb the regular arrangement of atoms in solid-state oxides [202,203]. Oxygen defects are 0D point vacancies that are created electronically in photocatalysts [204]. Solid-state oxide photocatalysts may contain oxygen defects either present before or incorporated into the crystal during synthesis [205]. The annealing temperature affects the formation energy, the partial pressure of oxygen, and the presence of additional electron-donating defects in the host crystal, all of which influence the concentration of defects caused by vacancies [206,207]. Every oxygen vacancy can function as an n-type double donor by donating two electrons to the CB [206]. Consequently, the existence of oxygen vacancies significantly impacts the catalyst's efficiency. As a result, engineering oxygen defects control to manipulate electrochemical and catalytic capabilities represents a feasible approach to augment hydrogen generation using photocatalysts.

The configuration of oxygen anions in various geometries surrounding a metal cation has an impact on the metal center where the d orbitals are situated as illustrated in Figure 12(a) and (b) [72,208]. Removing an oxygen atom from an octahedral geometry (Oh) can cause a transformation into a square pyramidal configuration (C4v), which leads to changes in the cleavage and stabilization of the t_{2g} (d_{xy}, d_{yz}, d_{xz}) and, *e.g.*, (d_{2x-y_2}, d_{z_2}) orbitals. Increasing the electronegativity of the metal cation can enhance the oxygen–metal hybridization, which controls surface binding energies and the formation of VB maxima and CBM, known as frontier orbitals [209]. The characteristics of the frontier orbitals determine surface reactivity and catalytic activity in

addition to redox properties [30,72,90,210,211]. Charge transfer in a semiconductor takes place at the boundary between the solid and liquid phases when the electrochemical potentials in both the solid and the solution reach equilibrium [70,212,213]. Consequently, a depletion area is created that extends from the surface to the interior of the semiconductor. The area of depletion consists of ionized entities and generates an internal electric field that facilitates the separation of photogenerated charges and inhibits the recombination of electrons and holes [90,210,214]. The presence of oxygen vacancies allows for the manipulation of the intensity of this interfacial field by altering the concentration of ionized species. The material can be altered in terms of light absorption, electrical conductivity, and adsorptive characteristics as per previous literature [209,215–217]. Nevertheless, in addition to their advantageous impacts, oxygen vacancies can also function as sites for photogenerated charge recombination, consequently fading the quantum yield of hydrogen [215,218]. The surplus defects of oxygen function as recombination sites for photoelectrons and holes, inhibiting the production of photocurrent rather than facilitating it. The graphical representation of the mechanism is shown in Figure 12(c) [219]. Therefore, for instance, an increase in the density of oxygen vacancies in In_2O_3 leads to a reduction in the efficiency of photon-to-current conversion as shown in Figure 12(d) [219]. Neutrality in oxygen vacancies in α-Fe_2O_3, as reported, has the potential to enhance the charge rate of recombination through the improvement of electron-vibrational coupling at the vacancy locations. Conversely, ionized oxygen defects can reduce the rate of recombination of charges through the induction of an expansion in the local iron envelope surrounding the O_v site. Consequently, electrons in the CB have a longer lifetime than holes in the VB, which undergo relaxation at a slower rate. So, hole entrapment regulates the electron–hole recombination process, which influences the oxidation reaction of oxygen-deficient α-Fe_2O_3 photocatalysts during water splitting [220]. Simulations of molecular dynamics indicate that neutral O_v states have a greater negative impact on the electron lifetime of $BiVO_4$ than ionized O_v states. Because neutral O_v induced localized structural distortions *via* the formation of V-O-V bonds, it compelled the entrapment of electrons and generated deep polaron-like V^{4+} hole traps. These could concurrently enhance the rate of non-radiative electron–hole recombination in comparison to pure $BiVO_4$.

3.6.2 Cation vacancies boosting charge separation for H_2 production

In addition to anion vacancies, cation vacancies are also a prominent subject in defect engineering. When compared to anion vacancies, cation vacancies may sometimes impart unique features to photocatalysts. However, the manufacturing or engineering management of cation vacancies remains a significant issue owing to the high production energy and stability of these vacancies [221,222]. Despite the persistent problem, many scientists have dedicated significant efforts toward multiple photocatalysts featuring cation vacancy. Wang *et al.* effectively synthesized Ti-defected TiO_2 using the solvothermal technique [223]. The presence of Ti vacancies altered the conductivity of TiO_2, changing it from being mostly n-type to being p-type. Compared to regular TiO_2, defective TiO_2 demonstrated significantly enhanced photocatalytic hydrogen evolution efficiency due to the more effective charge transfer inside the material and at the interface between the semiconductor and electrolyte (Figure 13(a) and (b)).

In addition to investigating the cation vacancies in metal oxides, the research also explores the cation vacancies in metal sulfides. As an example, Hao *et al.* produced Zn-deficient ZnS by using sodium sulfide as a source of sulfur during the hydrothermal process. Zinc vacancies have a significant impact on altering the electronic structure of zinc sulfide (ZnS). These vacancies elevate the locations of the VB, so reducing the oxidizing ability of the electron holes. This helps to safeguard ZnS against photocorrosion. The incorporation of Zn vacancies in ZnS effectively enhanced charge separation and electron transmission for photocatalytic hydrogen production as shown in Figure 13(c) and (d). Fu *et al.* used the hydrothermal approach to produce indium vacancies in In_2S_3. They observed that these vacancies had a beneficial effect on enhancing the efficiency of photocatalytic hydrogen evolution [224]. In conclusion, by lengthening charge carrier lifetimes, encouraging charge separation, altering electronic structures, boosting surface activity, and cooperating with cocatalysts, cation vacancies are essential for improving charge separation and all-around photocatalytic process efficiency.

3.6.3 Giant defect-induced charge separation for photocatalytic hydrogen production

Giant defect-induced effects on nanoscale charge separation in semiconductor photocatalysts" investigates the significant impact of defects on the performance of semiconductor-based photocatalysts, specifically focusing on charge separation processes at the nanoscale. The study employs time- and space-resolved surface photovoltage (SPV) techniques to explore how defects influence the distribution and separation of photogenerated charges in

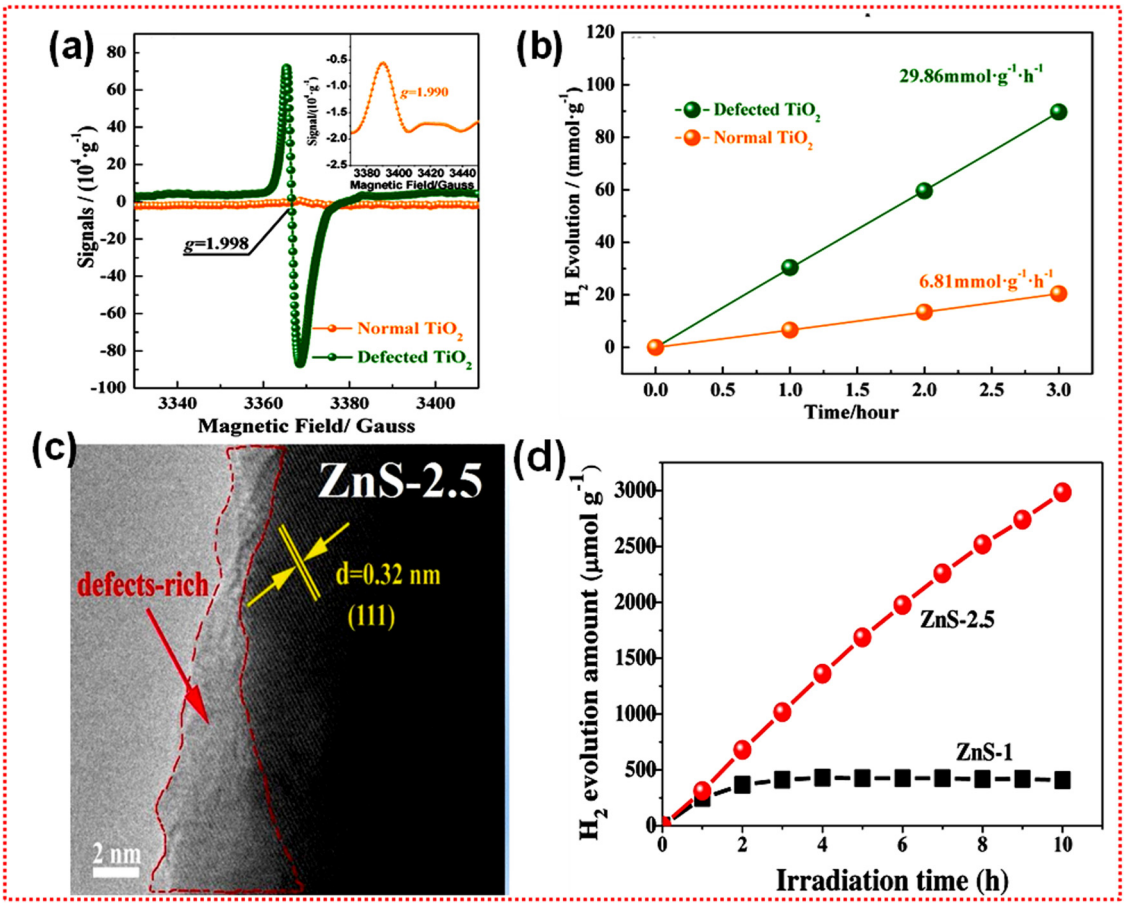

Figure 13: (a) Electron paramegnatic resonanace spectroscopy at low temperature. (b) Comparative H_2 production on normal and defective TiO_2. Reproduced with permission from Wang *et al.* [223], Copyright 2015 American Chemical Society. (c) HRTEM images of ZnS-2.5 having 2:5 between Zn and S. (d) Comparative photocatalytic H_2 production by ZnS1 and ZnS2. Reproduced with permission from Hao *et al.* [225], Copyright 2018 Elsevier.

Cu_2O single photocatalysts. The findings reveal that defects within a 100 nm surface region play a crucial role in stabilizing photogenerated charges and initiate a new charge separation process, driven by the trapping of these charges at near-surface defect states. The driving force for this defect-induced charge separation is shown to be greater than the built-in electric field in the space charge region (SCR), highlighting the potential of defect engineering to enhance solar energy conversion efficiency as shown in Figure 14. This research underscores the importance of understanding and manipulating defect states to improve photocatalytic performance and opens new avenues for optimizing semiconductor photocatalysts for solar energy applications (Table 2).

3.6.4 Defects engineering

Photocatalyst defects can both hinder and enhance hydrogen production. While they may act as recombination centers for photogenerated charges, careful engineering of these defects can promote charge separation and improve photocatalytic efficiency. Strategically manipulated defects can trap charges to prevent recombination and create new pathways for charge transport, thus enhancing HERs. This approach holds immense potential for designing efficient photocatalysts for clean and sustainable hydrogen generation.

3.7 Polarity-induced charge separation boosting hydrogen production

In photocatalysis, polarization field engineering has become a fascinating technique to separate photogenerated electron holes. The non-center symmetry of a material determines its polarity, a trait that comes from its pure crystalline structure [240]. The polarized electric field in semiconductor photocatalysts provides the driving force, which permit the distribution and movement of photogenerated electrons holes [241,242]. The manipulation of the intrinsic polarized

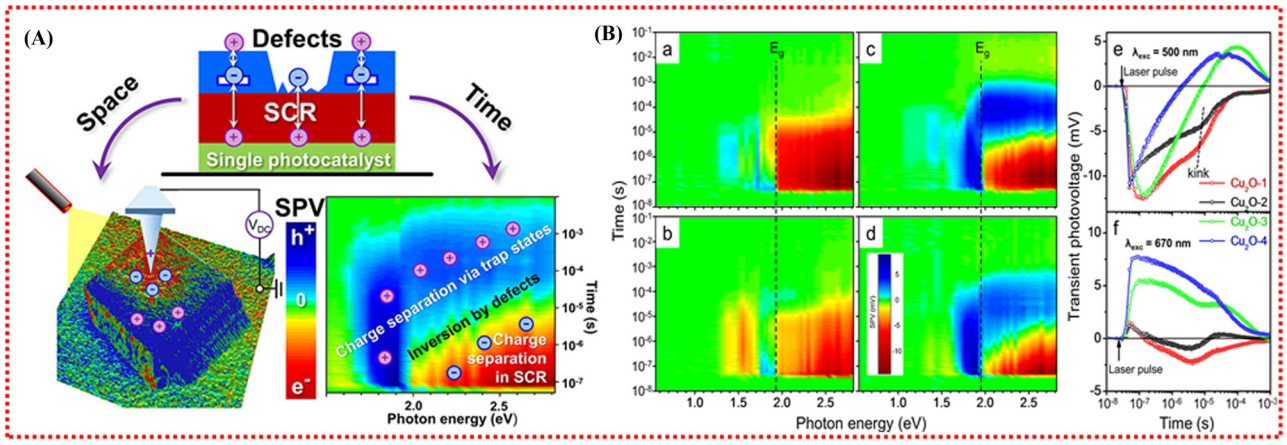

Figure 14: (A) Schematic representation of charge separation in a single photocatalyst is studied using space- and time-resolved methods, as shown in the figure. The top schematic shows charge separation-enabling defect sites in the photocatalyst's SCR. SPV microscopy is used to visualize charge distribution across the photocatalyst's surface in the left section of the figure. A time-resolved measurement of charge separation dynamics over different photon energies and time scales is shown on the right. This combined approach provides insights into photogenerated charge carrier spatial distribution and temporal evolution by analyzing defect-induced charge separation mechanisms. (B) Spectral and time-dependent SPV signal distributions for samples Cu_2O-1 to Cu_2O-4 (a–d) are shown in pseudo color. All images use the colored SPV bar in d. Red and blue represent negative and positive SPV signals. The dashed line represents the 1.92 eV band gap (Eg). (e and f) SPV transients of four Cu_2O samples at 500 nm (e) and 670 nm (f) excitation wavelengths, with photon energies of 2.48 eV (superb and gap excitation) and 1.85 eV (sub band gap excitation). Reproduced with permission from Chen *et al.* [226], Copyright 2013 ACS.

fields in semiconductors through breaking symmetry can be employed to completely create or control their pre-existing electric field, hence facilitating the separation of photogenerated charges. For instance, surface hydroxylation of g-C_3N_4 has been shown by Huang *et al.* to induce surface polarization, improving charge separation, and boosting its capacity for photocatalytic H_2 generation [243].

Based on numerical studies, it was shown that hydroxylation of g-C_3N_4 forms H–O–C═N, which promotes electron transport to the surface OH and speeds up photogenerated charge separation because of the increased polarized field. Furthermore, g-C_3N_4's remarkable piezoelectric characteristics have been scientifically established due to its atomically thin sheet-like structure. These properties arise from the intense polarization within the plane of the material along its *a*-axis. This polarization serves as a potent driving force for the electrochemical water splitting [244]. The photocatalytic performance in terms of H_2 generation by carbon nitrides has been enhanced with the addition of alkali metals along with its ionic salt in the reaction solution. The dielectric effects

Table 2: Some representative oxygen defect for photocatalytic hydrogen production

Photocatalysts	Defects engineering	Oxygen defects	Characterization	H_2 production	Ref.
N-dopedTiO_2 (Ti_3+/CdS	Annealing under $NaBH_4$	Oxygen defects	X-ray photoelectron spectroscopy (XPS), Raman, HRTEM	741.80 μmol g^{-1} h^{-1}	[227]
O–In_2S_4/TiO_{2-x}	Hydrothermal method	Oxygen defects	XPS	2880.5 μmol g^{-1} h^{-1}	[116]
WO_3/g-C_3N_4	Solid state method	Oxygen defects	HRTEM, XPS	1,034 μmol g^{-1} h^{-1}	[228]
Ni-Cr$(OH)_3$/C-TiO_2	Hydrothermal, wet chemical method	Oxygen defects	HRTEM, EPR, XPS	266 TOF/h	[229]
$ZnIn_2S_4$	Ultrasonic exfoliation: Hydrothermal	S defects	HRTEM, EPR, XPS	6.88 mmol g^{-1} h^{-1}	[230]
$ZnIn_2S_4$	$NaBH_4$ reduction	C defects	EPR, XPS	13.478 mmol g^{-1} h^{-1}	[231]
Cu-doped CeO_2	Metal ion doping	O defects	Density functional theory	18.36 μmol g^{-1} h^{-1}	[232]
$CaTiO_3$	Hydrogenation method	O defects	HRTEM, XPS	50 μmol g^{-1} h^{-1}	[233]
500°C-reduced black TiO_{2-x}	Thermal annealing	O defects	XPS, HRTEM, EPR	60 μmol g^{-1} h^{-1}	[234]
Brown TiO_2	Hydrogenation method	O defects	XPS, HRTEM, EPR	8.1 mmol g^{-1} h^{-1}	[235]
CdS/ZnO	$NaBH_4$ used as reducing agent	O defects	XPS, HRTEM, EPR	132.9 μmol g^{-1} h^{-1}	[236]
g-C_3N_4–ZnO	Mixing and ultrasonication	O defects	XPS, HRTEM	322 μmol g^{-1} h^{-1}	[237]
TiO_2	Aching through plasma	O defects	XPS, HRTEM	114 μmol g^{-1} h^{-1}	[238]
Mn-loaded ZnO	Hydrothermal	O defects	XPS, HRTEM	70 μmol g^{-1} h^{-1}	[239]

produced by charge dipoles close to the semiconductor surface are probably responsible for this amplification [245–247]. Due to its ability to produce a strong electric field at the surface area, surface polarity poses an interesting question for further investigation. Two van der Waals heterostructure monolayer C_2N/ZnSe and bilayer C_2N/ZnSe-were predicted by Jia *et al.* using density functional theory. In the bilayer C_2N/ZnSe, a type-II band alignment generates an inherent electric field at the interface crucial for separating photogenerated charges, resulting in electron accumulation in the CB. Conversely, in the C_2N/ZnSe monolayer (C_2N/ZnSe-ML) heterostructure, the strong built-in electric field extends from C_2N to ZnSe-ML due to the polarization and intrinsic electric field of ZnSe-ML. This creates a type-II heterostructure and effectively separates photogenerated electrons and holes thanks to the built-in electric field. They determined the electric field of ZnSe-ML, ZnSe-BL, C_2N/ZnSe-ML, and C_2N/ZnSe-BL to get a better idea of how charges move across interfaces. The results are shown in Figure 15(a)–(g) [248]. A built-in electric field is created at the interface of the bilayer C_2N/ZnSe by a type-II band alignment, which is essential for separating photogenerated charges where electrons concentrate in the CB. In contrast, the polarization of ZnSe-ML and its intrinsic electric field in the C_2N/ZnSe monolayer (C_2N/ZnSe-ML) heterostructure result in a strong built-in electric field extending from C_2N to ZnSe-ML. As one can see from Figure 15(j)–(l) [249], the polar surface (Ga-polar or N-polar) was oriented perpendicular to the *c*-axis direction, while the nonpolar surface was parallel to it. These differences in built-in electric fields and surface polarity-induced band bending are likely to separate the charges in space. The discovery that an anisotropic polarization field influences the separation of charges between the polar and nonpolar surfaces of GaN underscores the significance of constructing polarization fields in photocatalysts. This indicates that polarization fields play a crucial role in optimizing photocatalytic processes by improving the separation of photogenerated charges in photocatalysis.

3.7.1 Ferroelectric induced charge separation for photocatalytic H_2 production

Nowadays, semiconductors with an internal electric field due to spontaneous dipole moment and subsequent polarization are very desirable [250]. Several semiconductors have been demonstrated to act as active photocatalysts,

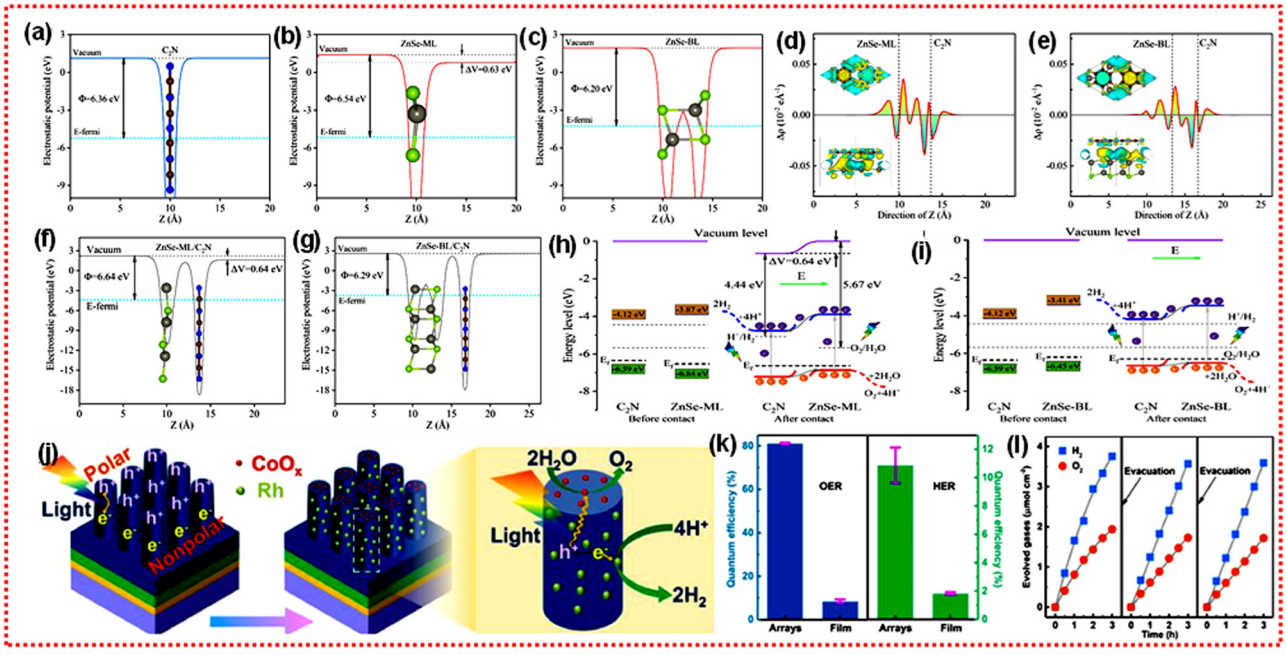

Figure 15: The average electrostatic potential along the *z*-axis. (a) For C_2N, (b) for ZnSe-ML, (c) ZnSe-BL. (d) and (e) The plane-averaged charge density differences of the C_2N/ZnSe-ML and C_2N/ZnSe-BL heterostructures. The inset is the 3D iso surface of the charge density difference, where the iso surface value is set to be 0.00015 e/A-3. (f) and (g) The average electrostatic potential along the *z*-axis for C_2N/ZnSe-ML heterostructure and C_2N/ZnSe-BL heterostructure, respectively. (h) and (i) Schematic illustration of the type-II photocatalytic mechanism. Reproduced with permission from Jia *et al.* [248], Copyright 2023, Elsevier. (j) Schematic representation of (GaN) system. (k) The corresponding QE of OER and HER. (l) Multi-cycles of photocatalytic OWS on the Rh-CoO_x/GaN NR arrays. All the photocatalytic reactions were reprinted with permission from Li *et al.* [249], Copyright 2020, John Wiley & Sons.

e.g., $PbTiO_3$ [251], $BaTiO_3$ [252], and $BiFeO_3$ [253]. For example, $K_{0.5}Na_{0.5}NbO_3$, which has a long-lasting polarization field, exhibits photogenerated charges that have a long lifespan, as reported by Park *et al.* The material's photocatalytic efficiency for producing hydrogen is increased by the ferroelectric polarization, which significantly improves the separation of photogenerated charges inside the material [254]. Furthermore, studies using various electric fields were carried out on photogenerated charge separation at the nano/micrometer level. The depolarization field in single-domain ferroelectric $PbTiO_3$ has been shown to be crucial in separating photogenerated electron–hole pairs, as shown in Figure 16(a) and (d), based on SRSPS. Electrons are directed toward the positive polarization facets by this field, whereas holes are directed toward the negative polarization facets. Furthermore, along the polarization direction, the electric potential difference between opposing polarization faces grows with particle size. This improves the charge separation capacity of $PbTiO_3$. These results suggest that this driving force may efficiently separate charges and directly increase ferroelectrics' photocatalytic activity. The chemical composition study of Niobium potassium niobate (NKN) powder further established the relationship between polarization and photocatalytic effectiveness. Figure 16(f) shows that the maximum polarization occurs at $x = 0.5$. The photocatalytic performance exhibited a same pattern, with the most significant improvement seen at $x = 0.5$ [254]. To explicitly illustrate this benefit of polarization, researchers conducted TRPL lifespan studies [254]. Typically, Figure 16(g) demonstrates that the excited electrons in polarized NKN have a longer lifespan compared to the non-polarized electrons. The determined lifespan of electric charges in polarized NKN powder was 3.31 ns, which is much more than that of the non-polarized counterpart (1.64 ns). This result unequivocally illustrates that the internal field has the capacity to impede the charge recombination process, hence facilitating the split of the photogenerated charges.

3.7.2 Section summary

The utilization of polarity-induced charge separation presents a highly promising approach to enhance hydrogen production in the field of photocatalysis. This method takes advantage of the inherent polarity of specific semiconductor materials. Polarity inherently generates discrete regions within the material exhibiting varying surface band positions. This facilitates the accumulation of photogenerated electrons and holes on opposite sides, reducing recombination and enhancing their involvement in HERs.

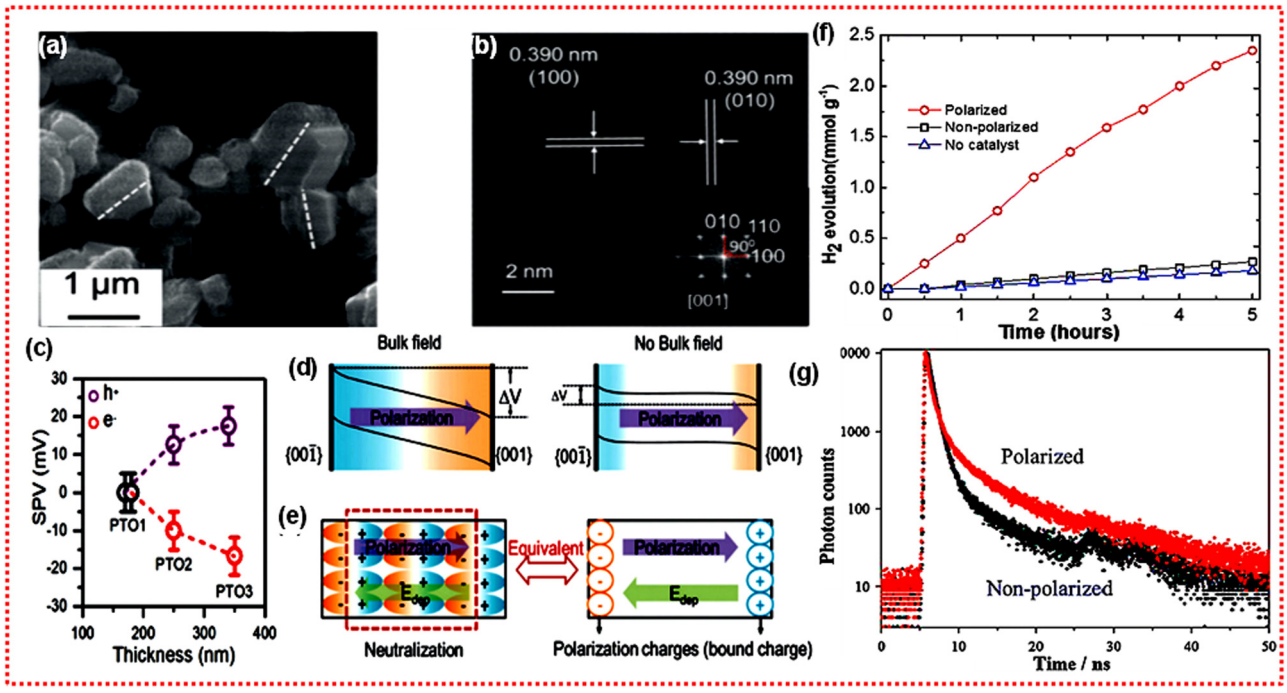

Figure 16: MnO_x photodepolarizes on $PbTiO_3$ surface. Spatial deposition of MnO_x on isotropic 001 facets of $PbTiO_3$. (b) HRTEM micrograph of $PbTiO_3$ along electron diffraction in the inset of 001 region axis. (c) Relationship of SPV thickness of $PbTiO_3$ particles. (d) Bandgap modulation in $PbTiO_3$ particle in the left and field polarization in the right. (e) Graphical representation of depolarized field. Reused with permission from Liu *et al.* [255]. (f) Effect of polarity on photocatalytic H_2 production, reused from Chen *et al.* [256]. (g) Time decay of $K_{0.5}Na_{0.5}NbO_3$, reused with permission from Park *et al.* [254].

Polarity decreases recombination losses and enhances the overall efficiency of hydrogen production by physically separating charges in space. Besides the potential, it has some challenges which have to be considered during synthesis of photocatalysts.

Achieving the desired surface orientation for optimal polarity can be challenging. Synthesis methods need to be refined for precise control over exposed facets. The surface properties and polarity can sometimes degrade over time, leading to reduced performance. Developing stable polar structures is crucial for long-term applications. Not all photocatalysts exhibit significant inherent polarity. Exploring new materials with tailored polar properties is necessary for broader application. A deeper understanding of the mechanisms governing charge transfer between polar surfaces is required to further optimize photocatalytic efficiency.

For efficient hydrogen production, it is important to understand the photocatalytic pathways to make an appropriate semiconducting heterojunction. Various types of heterojunctions are reported like type I and II, S-scheme, and Z-scheme heterojunction [257,258]. Here Figure 17 represents the mechanistic pathways of different heterojunctions. Dharani *et al.* featured a detail work on different types of S-schemes photocatalyst for solar hydrogen production [257]. Also, in materials development, Li Teng *et al.* explained recent advances, challenges, and future trends in various S-scheme photocatalyst for hydrogen production [259]. They had especially focused on S-scheme photocatalysts based on TiO_2, perovskite materials, CdS, g-C_3N_4, covalent organic framework (COF), ZnO, and $ZnIn_2S_4$, *etc.* Similarly, Schumacher and Marschall reported the recent advances and future challenges on Z-scheme photocatalyst for hydrogen production [260]. They described the recent trends of 2D/2D materials, direct Z-schemes, MOFs, and COF materials making heterojunction.

Besides the many interesting review, recently, various materials have been reported, which show efficient hydrogen production using different heterojunction. Similarly Qi *et al.* reported a novel In_2O_3/In_2S_3-$CdIn_2S_4$ nanotube photocatalyst with considerably improved photocatalytic H_2 production

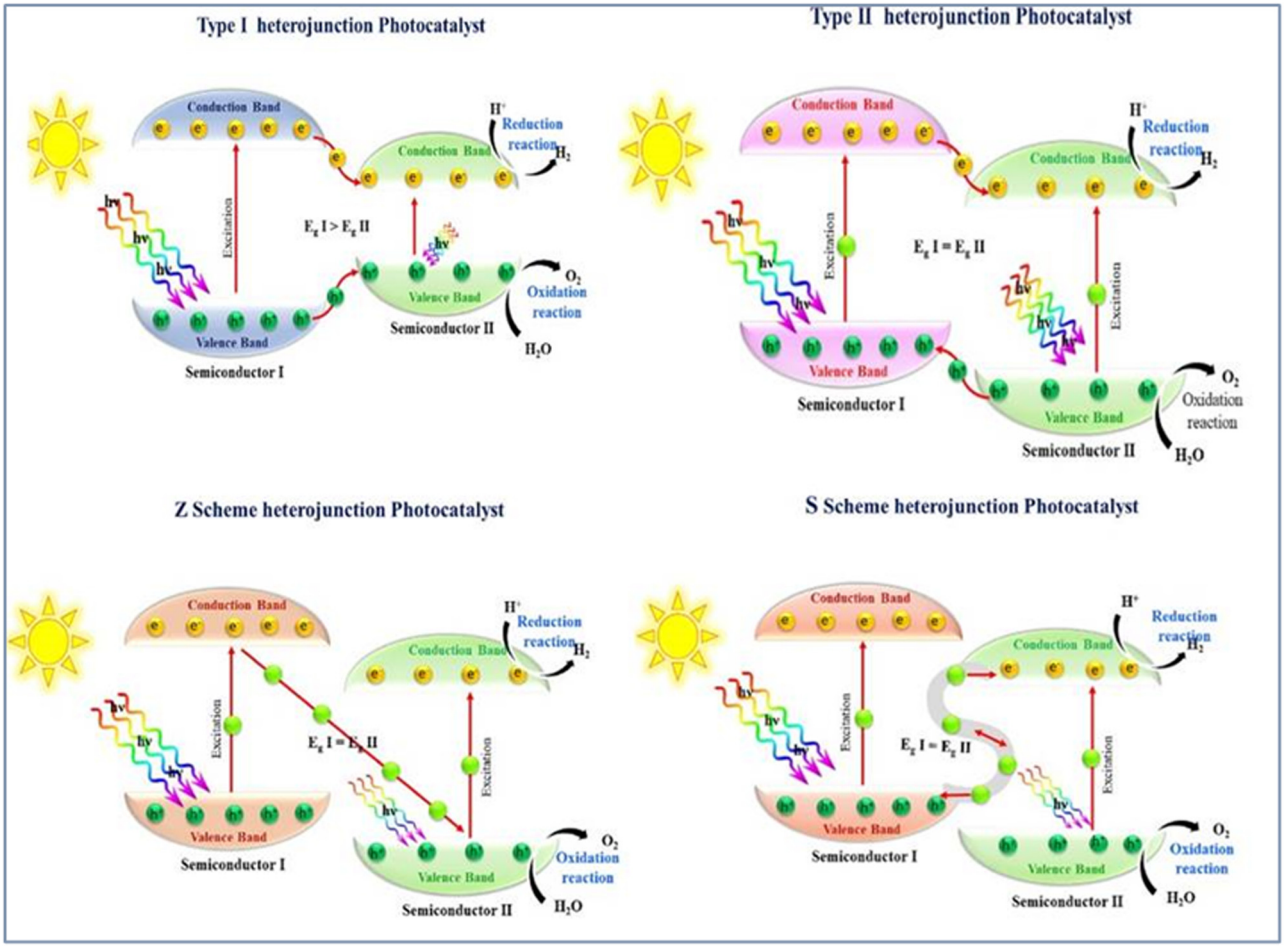

Figure 17: Schematic showing the different types of heterojunctions photocatalysts. Reproduced with permission from Dharani *et al.* [257].

(≥420 nm), yielding 2,892 μmol g^{-1} [261]. Increase in efficiency due to formation of Z-scheme leads to assist the photogenerated electrons and faster separation of charge. Liu *et al.* reported p–n-type direct Z-scheme heterojunction made by CuS/TiO_2 by using metal-organic framework (MOF) as a target substrate [262]. They found 29.5 times higher H_2 production compared to pristine CuS. Another $CoFe_2O_4$@$ZnIn_2S_4$ p–n heterojunction Z-scheme photocatalyst was designed by Ge *et al.* and prepared photocatalyst showing excellent hydrogen production rate (1576.5 μmol g^{-1} h^{-1}) in the absence of platinum cocatalyst [263]. Sun *et al.* reported Z-scheme of sea-urchin-like ZnS/SnO_2 heterojunctions, which leads to 15.5 times higher rate of hydrogen production [264].

Likewise, here we present some recent promising results of different type-I and type-II heterojunction materials. The heterojunction of $MnCo_2S_4$/CdS was reported by Cheng *et al.*, who prepared junction leads yielding 42 times higher H_2 production in comparison to pristine CdS [265]. Xue *et al.* showed that type-I $SnSe_2$/ZnS heterojunction, which can increase the H_2 production 7.4 times compared to pristine ZnS [266]. Cao *et al.* formed the type-I heterojunction by using defective TiO_2 and ultrafine Cu_2O *via in situ* method. They observed that hydrogen production rate increased by 3.2 times than only defective TiO_2 [267]. A 0D/0D type-I ZnS/$Ag_6Si_2O_7$ heterojunction was prepared by Zhu *et al.*, which showed five times higher hydrogen production [268]. Xu *et al.* prepared type-II heterostructure by using ZnO and $Mn_{0.2}Cd_{0.8}S$ which leads to 9.36 times increased hydrogen production (4297.99 μmol g^{-1} h^{-1}) as compared to pristine one [269]. Wang *et al.* reported construction of Type II heterojunction using metal sulfides and zirconium-based MOF [270]. This combination leads to higher hydrogen production (64.0 μmol g^{-1} h^{-1}) due to effective separation of charges. In another work a quasi-type-II heterostructure was prepared *via* merging Ni-MOF and Cu–In–Zn–S quantum dots which leads to the 5.28 higher H_2 productions than pristine quantum dots [270]. Peng *et al.* reported cost effective TiO_2/$SrTiO_3$ type-II heterojunctions that show 26 times increased H_2 production than pristine TiO_2 [271]. Li *et al.* prepared novel GaSe/$YAlS_3$ type-II heterojunction where STH improved by 406% along with increased absorption in visible region [272].

4 Summary and future outlook

The development of nanoscale engineering techniques for charge separation allows for precise control of charge flow, providing a detailed understanding of charge separation and transfer kinetics at the nanoscale level, which are providing knowledge guides for designing smart semiconductor-based photocatalysts. This review begins by presenting the fundamental principles of charge kinetics to elucidate the key elements involved in charge transport processes. These insights have facilitated the creation of effective nanoscale charge separation strategies with specific objectives. Subsequently, various methodologies for achieving charge separation at the nanoscale on the surface of photocatalysts are introduced. This study focuses on strategies to improve charge separation at the nanoscale in photocatalysts, and explore methods to strengthen the driving force for this charge separation, aiming to achieve a synergistic enhancement of both bulk and surface charge separation efficiencies. This combined approach has the potential to significantly improve overall photocatalytic performance. The development of sophisticated nanoscale regulation techniques is attributed to the recent advancements in our mechanistic understanding of photocatalysis. These advancements, coupled with precise photocatalyst design, have ushered in an era of more refined control over charge separation and transfer processes. While progress has been made in manipulating charge carrier dynamics within photocatalysts, significant challenges and opportunities remain in developing highly efficient and stable materials:

(1) From a nanoscale perspective, enhancing bulk charge separation frequently involves fabricating atomically thin structures. This method effectively reduces the travel distance for charge carriers within the bulk material, thereby promoting more efficient separation. However, synthesizing two-dimensional (2D) materials, especially non-layered variants, remains a formidable challenge. Overcoming these synthesis hurdles is crucial for advancing the efficiency of charge separation and, consequently, the overall performance of photocatalytic systems. Exploring harsher synthetic conditions may be necessary to overcome these limitations. Layered and junction photocatalysts can benefit from two promising strategies for promoting charge separation at the nanoscale: atom intercalation and atomic junction construction. These techniques introduce well-defined pathways for charge transport within the material. By creating these nanoscale channels, the random diffusion of charge carriers is reduced, leading to more directed transfer, and ultimately mitigating the recombination of electrons and holes. Unlike atom intercalation and atomic junction construction, which rely on manipulating the free diffusion process of photogenerated charge carriers, enhancing the driving force for charge separation offers a distinct approach. This strategy, often achieved by polar unit stacking or increasing the polarity of individual units within the photocatalyst, enables the spontaneous separation of electrons and holes. They are essentially driven to move in opposite directions due to the enhanced

electrostatic force. However, it is important to note that the intrinsic diffusion pathway for charge carriers is primarily dictated by the photocatalyst's electronic band structure, while the driving force for separation is largely influenced by its crystal structure. While the influence of the intrinsic diffusion behavior of photogenerated charges on their separation has been extensively studied, the impact of the driving force on this behavior remains relatively unexplored. Recent findings suggest that piezoelectric polarization can enhance the reduction of active sites, potentially altering the pathway for photo charge transfer. This opens an exciting new research avenue: by precisely tuning the polarity of photocatalysts, we can potentially create a powerful driving force that optimizes charge movement within the material. This could significantly improve photocatalytic performance.

(2) Poly-step synthetic procedures are often employed to develop collaborative strategies that simultaneously enhance both bulk and surface charge separation in photocatalysts. This combined approach has the potential to dramatically improve photocatalytic activity by creating synergistic effects. These effects can arise from the combination of multiple strategies, leading to a significant boost in overall charge separation efficiency. However, potential suppression effects can also occur due to incompatibilities between different strategies. A key challenge lies in optimizing material design to avoid or minimize these conflicts within co-strategies while maximizing their synergistic advantages. This requires a deep understanding of the interplay between various approaches and their impact on charge transport and recombination processes.

(3) Surface engineering and hierarchical, core–shell engineering are two prominent nanoscale strategies for enhancing surface charge separation. These techniques aim to regulate the spatial structure of the photocatalyst surface. Surface defect engineering introduces controlled defects, like vacancies and dopants, which can create built in-electric field, which facilitate photogenerated charge separation. Alternatively, hierarchical, and core–shell engineering help in quick charge transportation and hindering recombination. However, the effectiveness of defects depends heavily on their type, location, and concentration. While the synergistic interaction of multiple defects, such as vacancies and dopants, can significantly improve the photocatalytic performance, it also significantly increases the complexity of defect design. Additionally, the potential for corrosion caused by defects on the photocatalyst's surface lattice presents another challenge. While surface phase junctions offer a complementary approach to enhance charge separation. These junctions provide several benefits, including: Facilitated charge transfer between phases. Synergistic effects between different phases lead to enhancement of charge separation. The combined effect of these benefits can lead to a significant boost in the overall photocatalytic efficiency.

(4) The basic understanding of the intricate mechanisms governing photogenerated charge separation remains incomplete. While some of the basics are discussed, key parameters influencing charge diffusion, real-world scenarios involve highly complex. To deepen our understanding of these existing mechanisms, microscopic studies are needed that probe photocatalysis at smaller scales. This necessitates the development and application of advanced characterization techniques specifically designed to analyze charge dynamics. A deeper understanding of charge carrier dynamics within photocatalysts necessitates a comprehensive investigation of charge kinetics across both spatial and temporal dimensions. The experimental technique has some benefits along with limitations. For the mitigation of the limitations, the development of multi-scale theoretical simulations is highly anticipated. These simulations, incorporating functionalities that capture the microscopic behavior of charge carriers, could significantly complement experimental data. Such theoretical models could provide insights into charge transfer at the surface of photocatalysts. These perspectives indicate a multi-faceted approach for improving photocatalytic efficiency, combining material design, advanced characterization, and innovative fabrication techniques to overcome current challenges and achieve significant advancements in semiconductor-based photocatalysis.

The quest to optimize photocatalytic processes has placed increasing emphasis on charge separation efficiency. Exploiting nanoscale-level control strategies offers a revolutionary approach, bringing this longstanding scientific challenge into the realm of microscopic manipulation. High-efficiency photocatalytic systems are a major target in material design. To achieve this goal, researchers are turning to nanoscale-level charge separation strategies. These strategies aim to optimize the internal processes within photocatalysts, leading to improvements in AQE, STH conversion efficiency, or IPCE for photo electrocatalytic applications. This review aims to be a springboard for a deeper understanding of photogenerated charge kinetics. By providing this knowledge base, we hope to empower researchers with a bottom-up design approach for efficient photocatalysts. This, in turn, is expected to ignite further research fervor toward the precise design of high-performance photocatalysts.

Funding information: This work was financially supported by "Producing Hydrogen in Trentino-H_2@TN" (PAT-Trento) through the research grant (SAP 40104237), and by the National Natural Science Foundation of China (Grant No. 51874146), the China Postdoctoral Science Foundation (Grant Nos 2018T110551 and 2017M621640), the Deanship of Scientific Research of King Khalid University, Saudi Arabia, through Large Groups Project under Grant number RGP2/328/45 and also this work was supported by the Deanship of Scientific Research at Imam Mohammad Ibn Saud Islamic University (IMSIU), Saudi Arabia.

Author contributions: All authors have accepted responsibility for the entire content of this manuscript and approved its submission.

Conflicts of interest: The authors state no conflict of interest.

Data availability statement: The datasets generated and/or analyzed during the current study are available from the corresponding author on reasonable request.

References

[1] Delannoy L, Auzanneau M, Andrieu B, Vidal O, Longaretti P-Y, Prados E, et al. Emerging consensus on net energy paves the way for improved integrated assessment modeling. Energy Environ Sci. 2024;17:11–26.

[2] Han Z, Zakari A, Youn IJ, Tawiah V. The impact of natural resources on renewable energy consumption. Resour Policy. 2023;83:103692.

[3] Zou Y-Q, von Wolff N, Anaby A, Xie Y, Milstein D. Ethylene glycol as an efficient and reversible liquid-organic hydrogen carrier. Nat Catal. 2019;2:415–22.

[4] Song H, Luo S, Huang H, Deng B, Ye J. Solar-driven hydrogen production: Recent advances, challenges, and future perspectives. ACS Energy Lett. 2022;7:1043–65.

[5] Birol F. The future of hydrogen: seizing today's opportunities. IEA Report prepared for the G; 2019. p. 20.

[6] Khan K, Tao X, Shi M, Zeng B, Feng Z, Li C, et al. Visible-light-driven photocatalytic hydrogen production on $Cd_{0.5}Zn_{0.5}S$ nanorods with an apparent quantum efficiency exceeding 80%. Adv Funct Mater. 2020;30:2003731.

[7] Megía PJ, Vizcaíno AJ, Calles JA, Carrero A. Hydrogen production technologies: From fossil fuels toward renewable sources. A mini review. Energy & Fuels. 2021;35:16403–15.

[8] Zhou P, Navid IA, Ma Y, Xiao Y, Wang P, Ye Z, et al. Solar-to-hydrogen efficiency of more than 9% in photocatalytic water splitting. Nature. 2023;613:66–70.

[9] Ampelli C, Giusi D, Miceli M, Merdzhanova T, Smirnov V, Chime U, et al. An artificial leaf device built with earth-abundant materials for combined H_2 production and storage as formate with efficiency >10%. Energy Environ Sci. 2023;16:1644–61.

[10] Kim JH, Hansora D, Sharma P, Jang J-W, Lee JS. Toward practical solar hydrogen production–an artificial photosynthetic leaf-to-farm challenge. Chem Soc Rev. 2019;48:1908–71.

[11] Fujishima A, Honda K. Electrochemical photolysis of water at a semiconductor electrode. Nature. 1972;238:37–8.

[12] Lelieveld J, Pöschl U. Chemists can help to solve the air-pollution health crisis. Nature. 2017;551:291–3.

[13] Opoku F, Govender KK, van Sittert CGCE, Govender PP. Recent progress in the development of semiconductor-based photocatalyst materials for applications in photocatalytic water splitting and degradation of pollutants. Adv Sustain Syst. 2017;1:1700006.

[14] Chen X, Shen S, Guo L, Mao SS. Semiconductor-based photocatalytic hydrogen generation. Chem Rev. 2010;110:6503–70.

[15] Lin S, Zhang Y, You Y, Zeng C, Xiao X, Ma T, et al. Bifunctional hydrogen production and storage on 0D–1D heterojunction of $Cd_{0.5}Zn_{0.5}S$@Halloysites. Adv Funct Mater. 2019;29:1903825.

[16] Tu W, Zhou Y, Zou Z. Photocatalytic conversion of CO_2 into renewable hydrocarbon fuels: state-of-the-art accomplishment, challenges, and prospects. Adv Mater (Deerfield Beach, Fla). 2014;26:4607–26.

[17] Bai S, Wang L, Li Z, Xiong Y. Facet-engineered surface and interface design of photocatalytic materials. Adv Sci (Weinheim, Baden-Wurttemberg, Ger). 2017;4:1600216.

[18] Chen F, Huang H, Ye L, Zhang T, Zhang Y, Han X, et al. Thickness-dependent facet junction control of layered $BiOIO_3$ single crystals for highly efficient CO_2 photoreduction. Adv Funct Mater. 2018;28:1804284.

[19] Wang Q, Domen K. Particulate photocatalysts for light-driven water splitting: mechanisms, challenges, and design strategies. Chem Rev. 2019;120:919–85.

[20] Chen Y, Feng X, Liu Y, Guan X, Burda C, Guo L. Metal oxide-based tandem cells for self-biased photoelectrochemical water splitting. ACS Energy Lett. 2020;5:844–66.

[21] Zhou X, Liu R, Sun K, Friedrich D, McDowell MT, Yang F, et al. Interface engineering of the photoelectrochemical performance of Ni-oxide-coated n-Si photoanodes by atomic-layer deposition of ultrathin films of cobalt oxide. Energy Environ Sci. 2015;8:2644–9.

[22] Budama VK, Duarte JPR, Roeb M, Sattler C. Potential of solar thermochemical water-splitting cycles: A review. Sol Energy. 2023;249:353–66.

[23] Luo S, Ren X, Lin H, Song H, Ye J. Plasmonic photothermal catalysis for solar-to-fuel conversion: current status and prospects. Chem Sci. 2021;12:5701–19.

[24] Lu W-N, Luo S, Zhao Y, Xu J, Yang G, Picheau E, et al. Bifunctional Co active site on dilute CoCu plasmonic alloy for light-driven H_2 production from methanol and water. Appl Catal B: Environ. 2023;343:123520.

[25] Mastepanov A. From Covid "today" to low-carbon "tomorrow": analysis of foreign forecasts for the development of world energy. Georesursy. 2021;23:42–52.

[26] Outlook AE. Energy information administration. Department of Energy; 2010. vol. 92010, p. 1–15.

[27] Li R. Latest progress in hydrogen production from solar water splitting *via* photocatalysis, photoelectrochemical, and photovoltaic-photoelectrochemical solutions. Chin J Catal. 2017;38:5–12.

[28] Chen S, Takata T, Domen K. Particulate photocatalysts for overall water splitting. Nat Rev Mater. 2017;2:1–17.

[29] Chen R, Fan F, Dittrich T, Li C. Imaging photogenerated charge carriers on surfaces and interfaces of photocatalysts with surface photovoltage microscopy. Chem Soc Rev. 2018;47:8238–62.

[30] Corby S, Rao RR, Steier L, Durrant JR. The kinetics of metal oxide photoanodes from charge generation to catalysis. Nat Rev Mater. 2021;6:1136–55.
[31] Yang J, Wang D, Han H, Li C. Roles of co-catalysts in photocatalysis and photoelectrocatalysis. Acc Chem Res. 2013;46:1900–9.
[32] Ding C, Shi J, Wang Z, Li C. Photoelectrocatalytic water splitting: significance of cocatalysts, electrolyte, and interfaces. ACS Catal. 2017;7:675–88.
[33] Huo H, He H, Huang C, Guan X, Wu F, Du Y, et al. Solar-driven CO_2-to-ethanol conversion enabled by continuous CO_2 transport *via* a superhydrophobic Cu_2O nano fence. Chem Sci. 2024;15:1638–47.
[34] Jiang T, Wei J, Li J, Xue H, Tian J, Gautier R. Rapid identification of efficient photocatalysts by visualizing the spatial distribution of photoinduced charge carriers. ACS Catal. 2023;13:4168–77.
[35] Agouridas V, El Mahdi O, Diemer V, Cargoet M, Monbaliu J-CM, Melnyk O. Native chemical ligation and extended methods: mechanisms, catalysis, scope, and limitations. Chem Rev. 2019;119:7328–443.
[36] Khan I, Liu W, Zada A, Raziq F, Ali S, Shah MIA, et al. Recent progress in emerging materials and hybrid nanocomposites for peroxymonosulfate and peroxydisulfate activation towards solar light-driven photocatalytic degradation of emerging pollutants. Coord Chem Rev. 2024;499:215466.
[37] Huang Z, Luo N, Zhang C, Wang F. Radical generation and fate control for photocatalytic biomass conversion. Nat Rev Chem. 2022;6:197–214.
[38] Luo H, Barrio J, Sunny N, Li A, Steier L, Shah N, et al. Progress and perspectives in photo- and electrochemical-oxidation of biomass for sustainable chemicals and hydrogen production. Adv Energy Mater. 2021;11:2101180.
[39] Wu X, Xie S, Zhang H, Zhang Q, Sels BF, Wang Y. Metal sulfide photocatalysts for lignocellulose valorization. Adv Mater. 2021;33:2007129.
[40] Shimura K, Yoshida H. Heterogeneous photocatalytic hydrogen production from water and biomass derivatives. Energy Environ Sci. 2011;4:2467–81.
[41] Ma X, Cheng H. In-plane electric field induced by cyano groups and graphitic carbon structure for enhancing photocatalytic hydrogen production of carbon nitride. Sep Purif Technol. 2024;330:125260.
[42] KazumaE. Key factors for controlling plasmon-induced chemical reactions on metal surfaces. J Phys Chem Lett. 2023;15:59–67.
[43] Le Bahers T, Rerat M, Sautet PJT. Semiconductors used in photovoltaic and photocatalytic devices: assessing fundamental properties from DFT. J Phys Chem C. 2014;118:5997–6008.
[44] Chen R, Pang S, An H, Zhu J, Ye S, Gao Y, et al. Charge separation *via* asymmetric illumination in photocatalytic Cu_2O particles. Nat Energy. 2018;3:655–63.
[45] Kittel C, McEuen P. Introduction to solid state physics. John Wiley & Sons, Inc; 2018.
[46] Mora-Seró I, Dittrich T, Garcia-Belmonte G, Bisquert J. Determination of spatial charge separation of diffusing electrons by transient photovoltage measurements. J Appl Phys. 2006;100:103705.
[47] Melitz W, Shen J, Kummel AC, Lee S. Kelvin probe force microscopy and its application. Surf Sci Rep. 2011;66:1–27.
[48] Schäfer S, Wang Z, Zierold R, Kipp T, Mews A. Laser-induced charge separation in CdSe nanowires. Nano Lett. 2011;11:2672–7.
[49] Warren SC, Voïtchovsky K, Dotan H, Leroy CM, Cornuz M, Stellacci F, et al. Identifying champion nanostructures for solar water-splitting. Nat Mater. 2013;12:842–9.
[50] Lee S-H, Lee SW, Oh T, Petrosko SH, Mirkin CA, Jang J-W. Direct observation of plasmon-induced interfacial charge separation in metal/semiconductor hybrid nanostructures by measuring surface potentials. Nano Lett. 2018;18:109–16.
[51] Lu J, Lv Z, Qiu X, Lai S, Jiang H. Ultrasensitive and high-speed AlGaN/AlN solar-blind ultraviolet photodetector: A full-channel-self-depleted phototransistor by a virtual photogate. Photonics Res. 2022;10:2229–38.
[52] Costi R, Cohen G, Salant A, Rabani E, Banin U. Electrostatic force microscopy study of single Au-CdSe hybrid nanodumbbells: evidence for light-induced charge separation. Nano Lett. 2009;9:2031–9.
[53] Lanza MJM. A review on resistive switching in high-k dielectrics: A nanoscale point of view using conductive atomic force microscope. Mater (Basel, Switz). 2014;7:2155–82.
[54] Li JB, Chawla V, Clemens BM. Investigating the role of grain boundaries in CZTS and CZTSSe thin film solar cells with scanning probe microscopy. Adv Mater. 2012;24:720–3.
[55] Li B, Chen M, Hu Q, Zhu J, Yang X, Li Z, et al. Facilely tunable dodecahedral POM framework loaded with mono- or bimetallic sites for efficient photocatalytic CO_2 reduction. Appl Catal B: Environ Energy. 2024;346:123733.
[56] Xu JY, Tong X, Yu P, Wenya GE, McGrath T, Fong MJ, et al. Ultrafast dynamics of charge transfer and photochemical reactions in solar energy conversion. Adv Sci (Weinheim, Baden-Wurttemberg, Ger). 2018;5:1800221.
[57] Knowles KE, Koch MD, Shelton JL. Three applications of ultrafast transient absorption spectroscopy of semiconductor thin films: spectroelectrochemistry, microscopy, and identification of thermal contributions. J Mater Chem C. 2018;6:11853–67.
[58] Tan X, Gustafson TL, Lefumeux C, Burdzinski G, Buntinx G, Poizat OJ. Solvation dynamics probed by femtosecond transient absorption spectroscopy: vibrational cooling and conformational relaxation in S1 trans-4,4′-diphenylstibene. J Phys Chem A. 2002;106:3593–8.
[59] Rajan A, Neppolian B, Anpo M. Visible light-responsive TiO_2 thin-film photocatalysts for the separate evolution of H_2 and O_2 from water. UV-visible photocatalysis clean energy prod pollut remediation. Wiley Online Library; 2023. p. 137–52.
[60] Bian Z, Tachikawa T, Zhang P, Fujitsuka M, Majima T. A nanocomposite superstructure of metal oxides with effective charge transfer interfaces. Nat Commun. 2014;5:3038.
[61] Dittrich T, Valle Rios L, Kapil S, Gurieva G, Rujisamphan N, Schorr S. Temperature dependent transient surface photovoltage spectroscopy of a $Cu_{1.95}Zn_{1.1}Sn_{0.96}Se_4$ kesterite single phase powder. Appl Phys Lett. 2017;110:023901.
[62] Nakada A, Higashi M, Kimura T, Suzuki H, Kato D, Okajima H, et al. Band engineering of double-layered Sillén–Aurivillius perovskite oxychlorides for visible-light-driven water splitting. Chem Mater. 2019;31:3419–29.
[63] Beane G, Devkota T, Brown BS, Hartland GV. Ultrafast measurements of the dynamics of single nanostructures: a review. Rep Prog Phys. 2018;82:016401.
[64] Guo Z, Manser JS, Wan Y, Kamat PV, Huang L. Spatial and temporal imaging of long-range charge transport in perovskite thin films by ultrafast microscopy. Nat Commun. 2015;6:7471.
[65] Svelto O, Silvestri SD, Denardo G. Ultrafast Processes in Spectroscopy [electronic resource].
[66] Yu M, Wang T, Huang C, Wu F, Liu X, Huo H, et al. Enhanced charge separation by continuous homojunction with spatially

separated redox sites for hydrogen evolution. Nano Res. 2023;16:12323–30.
[67] Sze S, Ng K. Physics of semiconductor devices. Vol. 1, Hoboken: John Wiley & Sons, Inc.; 2007. p. 7–78.
[68] Uzun İ, Taşyürek LB, Orak İ, Karakaplan M. Evaluation of synthesized new cellulose derivatives to make diodes and investigation of electrical and photoelectrical characteristics of these diodes. Mater Sci Eng: B. 2024;300:117111.
[69] Barber J. A mechanism for water splitting and oxygen production in photosynthesis. Nat Plants. 2017;3:1–5.
[70] Rahman MZ, Kibria MG, Mullins CB. Metal-free photocatalysts for hydrogen evolution. Chem Soc Rev. 2020;49:1887–931.
[71] He Y, Huang Z, Wu K, Ma J, Zhou Y-G, Yu Z. Recent advances in transition-metal-catalyzed carbene insertion to C–H bonds. Chem Soc Rev. 2022;51:2759–852.
[72] Pastor E, Sachs M, Selim S, Durrant JR, Bakulin AA, Walsh A. Electronic defects in metal oxide photocatalysts. Nat Rev Mater. 2022;7:503–21.
[73] Yang Y, Niu S, Han D, Liu T, Wang G, Li Y. Progress in developing metal oxide nanomaterials for photoelectrochemical water splitting. Adv Energy Mater. 2017;7:1700555.
[74] Borgarello E, Kiwi J, Graetzel M, Pelizzetti E, Visca M. Visible light induced water cleavage in colloidal solutions of chromium-doped titanium dioxide particles. J Am Chem Soc. 1982;104:2996–3002.
[75] Zhang C, Ma C, Zhang W, Wang Y, Rehman ZU, Shen X, et al. $CoFe_2O_4$ nanoparticles modified amidation of N-doped carbon nanofibers hybrid catalysts to accelerate electrochemical kinetics of Li-S batteries with high sulfur loading. Chem Eng J. 2024;481:148374.
[76] Ding X, Yu W, Sheng X, Shi H, You D, Peng M, et al. Feasible fabrication of o-phenanthroline-based polymer adsorbent for selective capture of aqueous Ag(I). Chin Chem Lett. 2023;34:107485.
[77] Bautista-Quijano JR, Telschow O, Paulus F, Vaynzof Y. Solvent-antisolvent interactions in metal halide perovskites. Chem Commun (Cambridge, Engl). 2023;59:10588–603.
[78] Huang H, Dai B, Wang W, Lu C, Kou J, Ni Y, et al. Oriented built-in electric field introduced by surface gradient diffusion doping for enhanced photocatalytic H_2 evolution in CdS nanorods. Nano Lett. 2017;17:3803–8.
[79] Chakraborty S, Mondal P, Makkar M, Moretti L, Cerullo G, Viswanatha R. Transition metal doping in CdS quantum dots: diffusion, magnetism, and ultrafast charge carrier dynamics. Chem Mater. 2023;35:2146–54.
[80] Chen X, Liu L, Yu PY, Mao SS. Increasing solar absorption for photocatalysis with black hydrogenated titanium dioxide nanocrystals. Science. 2011;331:746–50.
[81] Murthy DH, Matsuzaki H, Wang Q, Suzuki Y, Seki K, Hisatomi T, et al. Revealing the role of the Rh valence state, La doping level and Ru cocatalyst in determining the H_2 evolution efficiency in doped $SrTiO_3$ photocatalysts. Sustain Energy Fuels. 2019;3:208–18.
[82] Furuhashi K, Jia Q, Kudo A, Onishi HJ. Time-resolved infrared absorption study of $SrTiO_3$ photocatalysts codoped with rhodium and antimony. J Phys Chem C. 2013;117:19101–6.
[83] Ishii T, Kato H, Kudo A. H_2 evolution from an aqueous methanol solution on $SrTiO_3$ photocatalysts codoped with chromium and tantalum ions under visible light irradiation. J Photochem Photobiol A: Chem. 2004;163:181–6.
[84] Zhao Z, Willard EJ, Li H, Wu Z, Castro RH, Osterloh FE. Aluminum enhances photochemical charge separation in strontium titanate nanocrystal photocatalysts for overall water splitting. J Mater Chem A. 2018;6:16170–6.
[85] Gu P, Wang X, Li T, Meng H. Investigation of defects in N-doped ZnO powders prepared by a facile solvothermal method and their UV photocatalytic properties. Mater Res Bull. 2013;48:4699–703.
[86] Maleki A, Rosen MA. Design of a cost-effective on-grid hybrid wind–hydrogen based CHP system using a modified heuristic approach. Int J Hydrogen Energy. 2017;42:15973–89.
[87] Cheng C, Fang W-H, Long R, Prezhdo OV. Water splitting with a single-atom Cu/TiO_2 photocatalyst: Atomistic origin of high efficiency and proposed enhancement by spin selection. JACS Au. 2021;1:550–9.
[88] Qiu W, Xiao S, Ke J, Wang Z, Tang S, Zhang K, et al. Freeing the polarons to facilitate charge transport in $BiVO_4$ from oxygen vacancies with an oxidative 2D precursor. Angew Chem Int Ed. 2019;131:19263–71.
[89] Rahman MZ, Raziq F, Zhang H, Gascon J. Key strategies for enhancing H_2 production in transition metal oxide based photocatalysts. Angew Chem Int Ed. 2023;135:e202305385.
[90] Moss B, Wang Q, Butler KT, Grau-Crespo R, Selim S, Regoutz A, et al. Linking in situ charge accumulation to electronic structure in doped $SrTiO_3$ reveals design principles for hydrogen-evolving photocatalysts. Nat Mater. 2021;20:511–7.
[91] Rafique M, Hajra S, Irshad M, Usman M, Imran M, Assiri MA, et al. Hydrogen production using TiO_2-based photocatalysts: A comprehensive review. ACS Omega. 2023;8:25640–8.
[92] Meng F, Hao T, Tian W, Zhao J, Wang S, Zhang HJS, et al. Photocatalytic aqueous environmental remediation *via* two-dimensional carbon nitride nanosheets. Surf Interfaces. 2024;44:103717.
[93] Ouyang S, Kikugawa N, Chen D, Zou Z, Ye J. A systematical study on photocatalytic properties of $AgMO_2$ (M= Al, Ga, In): effects of chemical compositions, crystal structures, and electronic structures. J Phys Chem C. 2009;113:1560–6.
[94] Shi R, Ye HF, Liang F, Wang Z, Li K, Weng Y, et al. Interstitial P-doped CdS with long-lived photogenerated electrons for photocatalytic water splitting without sacrificial agents. Adv Mater. 2018;30:1705941.
[95] Ould-Chikh S, Proux O, Afanasiev P, Khrouz L, Hedhili MN, Anjum DH, et al. Photocatalysis with chromium-doped TiO_2: bulk and surface doping. ChemSusChem. 2014;7:1361–71.
[96] Tonda S, Kumar S, Kandula S, Shanker V. Fe-doped and -mediated graphitic carbon nitride nanosheets for enhanced photocatalytic performance under natural sunlight. J Mater Chem A. 2014;2:6772–80.
[97] Chang S-m, Liu W-s. Surface doping is more beneficial than bulk doping to the photocatalytic activity of vanadium-doped TiO_2. Appl Catal B: Environ. 2011;101:333–42.
[98] Shen S, Zhou J, Dong C-L, Hu Y, Tseng EN, Guo P, et al. Surface engineered doping of hematite nanorod arrays for improved photoelectrochemical water splitting. Sci Rep. 2014;4:6627.
[99] Li S, Zhang L, Jiang T, Chen L, Lin Y, Wang D, et al. Construction of shallow surface states through light Ni doping for high-efficiency photocatalytic hydrogen production of CdS nanocrystals. Chemistry. 2014;20:311–6.
[100] Shen S, Jiang J, Guo P, Kronawitter CX, Mao SS, Guo L. Effect of Cr doping on the photoelectrochemical performance of hematite nanorod photoanodes. Nano Energy. 2012;1:732–41.

[101] Feng N, Wang Q, Zheng A, Zhang Z, Fan J, Liu S-B, et al. Understanding the high photocatalytic activity of (B, Ag)-codoped TiO_2 under solar-light irradiation with XPS, solid-state NMR, and DFT calculations. J Am Chem Soc. 2013;135:1607–16.
[102] Jiang L, Yuan X, Zeng G, Chen X, Wu Z, Liang J, et al. Phosphorus- and sulfur-codoped g-C_3N_4: facile preparation, mechanism insight, and application as efficient photocatalyst for tetracycline and methyl orange degradation under visible light irradiation. ACS Sustain Chem & Eng. 2017;5:5831–41.
[103] Sayed M, Yu J, Liu G, Jaroniec M. Non-noble plasmonic metal-based photocatalysts. Chem Rev. 2022;122:10484–537.
[104] Fujishima A, Zhang X, Tryk DA. TiO_2 photocatalysis and related surface phenomena. Surf Sci Rep. 2008;63:515–82.
[105] Wang X, Xu Q, Li M, Shen S, Wang X, Wang Y, et al. Photocatalytic overall water splitting promoted by an α–β phase junction on Ga_2O_3. Angew Chem Int Ed Engl. 2012;124:13266–9.
[106] Liu G, Jimmy CY, Lu GQM, Cheng H-M. Crystal facet engineering of semiconductor photocatalysts: motivations, advances and unique properties. Chem Commun (Cambridge, Engl). 2011;47:6763–83.
[107] Kim D, Yong K. Boron doping induced charge transfer switching of a C_3N_4/ZnO photocatalyst from Z-scheme to type II to enhance photocatalytic hydrogen production. Appl Catal B: Environ. 2021;282:119538.
[108] Guo C, Tian K, Wang L, Liang F, Wang F, Chen D, et al. Approach of fermi level and electron-trap level in cadmium sulfide nanorods via molybdenum doping with enhanced carrier separation for boosted photocatalytic hydrogen production. J Colloid Interface Sci. 2021;583:661–71.
[109] Du C, Yan B, Lin Z, Yang G. Enhanced carrier separation and increased electron density in 2D heavily N-doped $ZnIn_2S_4$ for photocatalytic hydrogen production. J Mater Chem A. 2020;8:207–17.
[110] Zhang S, Zhang Z, Si Y, Li B, Deng F, Yang L, et al. Gradient hydrogen migration modulated with self-adapting S vacancy in copper-doped $ZnIn_2S_4$ nanosheet for photocatalytic hydrogen evolution. ACS Nano. 2021;15:15238–48.
[111] Gao J, Xue J, Jia S, Shen Q, Zhang X, Jia H, et al. Self-doping surface oxygen vacancy-induced lattice strains for enhancing visible light-driven photocatalytic H_2 evolution over black TiO_2. ACS Appl Mater Interfaces. 2021;13:18758–71.
[112] Liu E, Lin X, Hong Y, Yang L, Luo B, Shi W, et al. Rational copolymerization strategy engineered C self-doped g-C_3N_4 for efficient and robust solar photocatalytic H_2 evolution. Renew Energy. 2021;178:757–65.
[113] Zou W-S, Hong M, Kong W-L, Zhao Q-C, Li W, Wang Y. Oxygen vacancy defects and cobalt nanoparticle-mediated charge separation in black Ti^{3+} self-doped TiO_2 mesoporous nanotubes for enhanced solar-driven hydrogen evolution and tetracycline degradation. ACS Appl Electron Mater. 2022;4:2885–96.
[114] Li G, Liang H, Yu H, Xu T, Bai J. Boosting visible-light-driven photocatalytic H_2 evolution of C/$ZnIn_2S_4$ hollow tubes by Ni doping. Fuel. 2022;328:125205.
[115] Biswal L, Nayak S, Parida K. Rationally designed Ti_3C_2/N, S-TiO_2/g-C_3N_4 ternary heterostructure with spatial charge separation for enhanced photocatalytic hydrogen evolution. J Colloid Interface Sci. 2022;621:254–66.
[116] Liu J, Wan J, Liu L, Yang W, Low J, Gao X, et al. Synergistic effect of oxygen defect and doping engineering on S-scheme O-$ZnIn_2S_4$/TiO_{2-x} heterojunction for effective photocatalytic hydrogen production by water reduction coupled with oxidative dehydrogenation. Chem Eng J. 2022;430:133125.
[117] Shao M, Chen H, Hao S, Liu H, Cao Y, Zhao Y, et al. N-doped vanadium carbide combined with Pt as a multifunctional cocatalyst to boost photocatalytic hydrogen production. Appl Surf Sci. 2022;577:151857.
[118] Ahmad I, Shukrullah S, Naz M, Ahmed E, Ahmad M, Akhtar M, et al. Microwave-assisted one-pot hydrothermal synthesis of V and La co-doped ZnO/CNTs nanocomposite for boosted photocatalytic hydrogen production. Int J Hydrogen Energy. 2022;47:15505–15.
[119] Chen L, Ning S, Liang R, Xia Y, Huang R, Yan G, et al. Potassium doped and nitrogen defect modified graphitic carbon nitride for boosted photocatalytic hydrogen production. Int J Hydrogen Energy. 2022;47:14044–52.
[120] Chen M, Zhou X, Luo J, Zhou X, Ge Y. Boosting photocatalytic hydrogen evolution of g-C_3N_4 via enhancing its interfacial redox activity and charge separation with Mo-doped CoSx. Int J Hydrogen Energy. 2022;47:35723–36.
[121] Babu P, Dash SR, Parida K. Mechanistic insight the visible light driven hydrogen generation by plasmonic Au-Cu alloy mounted on TiO_2@B-doped g-C_3N_4 heterojunction photocatalyst. J Alloy Compd. 2022;909:164754.
[122] Wang Y, Li J, Chen S, Xie Y, Ma Y, Luo Y, et al. In situ loading of $ZnIn_2S_4$ nanosheets onto S doped g-C_3N_4 nanosheets to construct type II heterojunctions for improving photocatalytic hydrogen production. J Alloy Compd. 2022;924:166569.
[123] Ren X, Liu F, Wang Q, Song H, Luo S, Li S, et al. Engineering interfacial charge transfer channel for efficient photocatalytic H_2 evolution: The interplay of CoPx and Ca^{2+} dopant. Appl Catal B: Environ. 2022;303:120887.
[124] Wu L, Su F, Liu T, Liu G-Q, Li Y, Ma T, et al. Phosphorus-doped single-crystalline quaternary sulfide nanobelts enable efficient visible-light photocatalytic hydrogen evolution. J Am Chem Soc. 2022;144:20620–9.
[125] Ding L, Zeng S, Zhang W, Guo C, Chen X, Peng B, et al. Nitrogen-doped Ti_3C_2 MXene quantum dots/1D CdS nanorod heterostructure photocatalyst of highly efficient hydrogen evolution. ACS Appl Energy Mater. 2022;5:11540–52.
[126] Han X, Liu P, Ran R, Wang W, Zhou W, Shao Z. Non-metal fluorine doping in Ruddlesden–Popper perovskite oxide enables high-efficiency photocatalytic water splitting for hydrogen production. Mater Today Energy. 2022;23:100896.
[127] Huang J, Chen J, Liu W, Zhang J, Chen J, Li Y. Copper-doped zinc sulfide nanoframes with three-dimensional photocatalytic surfaces for enhanced solar driven H_2 production. Chin J Catal. 2022;43:782–92.
[128] Gopannagari M, Rangappa AP, Seo S, Kim E, Reddy KAJ, Bhavani P, et al. Atomically engineered molybdenum di-sulfide by dual heteroatom doping for accelerating hydrogen evolution reaction on cadmium sulfide nanorods. Solid State Sci. 2022;134:107047.
[129] Zhou D, Xue X, Wang X, Luan Q, Li A, Zhang L, et al. Ni, In co-doped $ZnIn_2S_4$ for efficient hydrogen evolution: Modulating charge flow and balancing H adsorption/desorption. Appl Catal B: Environ. 2022;310:121337.
[130] Yang G, Chen T, Liu H, Xing C, Yu G, Li X. Bi-doped twin crystal $Zn_{0.5}Cd_{0.5}S$ photocatalyst for highly efficient photocatalytic hydrogen production from water. Appl Surf Sci. 2023;616:156393.
[131] Liu S, Chi D, Chen R, Ma Y, Fang H, Zhang K, et al. N-doped C layer boost Z-scheme interfacial charge transfer in TiO_2/$ZnIn_2S_4$

heterojunctions for enhance photocatalytic hydrogen evolution. Renew Energy. 2023;219:119494.
[132] Shi W, Cao L, Shi Y, Zhong W, Chen Z, Wei Y, et al. Boosted built-in electric field and active sites based on Ni-doped heptazine/triazine crystalline carbon nitride for achieving high-efficient photocatalytic H_2 evolution. J Mol Structure. 2023;1280:135076.
[133] Geng L, Li W, Dong M, Ma X, Li Y, Li M, et al. Synergistic effect of excellent carriers separation and efficient high level energy electron utilization on Bi^{3+}-$Ce_2Ti_2O_7$/$ZnIn_2S_4$ heterostructure for photocatalytic hydrogen production. J Colloid Interface Sci. 2023;650:2035–48.
[134] Mo Z, Miao Z, Yan P, Sun P, Wu G, Zhu X, et al. Electronic and energy level structural engineering of graphitic carbon nitride nanotubes with B and S co-doping for photocatalytic hydrogen evolution. J Colloid Interface Sci. 2023;645:525–32.
[135] Yang L, Gao T, Yuan S, Dong Y, Chen Y, Wang X, et al. Spatial charge separated two-dimensional/two-dimensional Cu-In_2S_3/CdS heterojunction for boosting photocatalytic hydrogen production. J Colloid Interface Sci. 2023;652:1503–11.
[136] Zhan M, Fang M, Li L, Zhao Y, Yang B, Min X, et al. Effect of Fe dopant on oxygen vacancy variation and enhanced photocatalysis hydrogen production of $LaMnO_3$ perovskite nanofibers. Mater Sci Semicond Process. 2023;166:107697.
[137] Du S, Lin S, Ren K, Li C, Zhang F. Revealing the effects of transition metal doping on CoSe cocatalyst for enhancing photocatalytic H_2 production. Appl Catal B: Environ. 2023;328:122503.
[138] Wu X, Li D, Luo B, Chen B, Huang Y, Yu T, et al. Molecular-level insights on NIR-driven photocatalytic H_2 generation with ultrathin porous S-doped g-C_3N_4 nanosheets. Appl Catal B: Environ. 2023;325:122292.
[139] Yashwanth H, Rondiya SR, Eya HI, Dzade NZ, Phase DM, Dhole SD, et al. Synergy between nitrogen, phosphorus co-doped carbon quantum dots and ZnO nanorods for enhanced hydrogen production. J Alloy Compd. 2023;937:168397.
[140] Li Y, Lai C, Zhong J, Li J. Largely elevated photocatalytic hydrogen generation over Eu doped g-C_3N_4 photocatalyst. Int J Hydrogen Energy. 2023;48:24356–68.
[141] Shi W, Cao L, Shi Y, Chen Z, Cai Y, Guo F, et al. Environmentally friendly supermolecule self-assembly preparation of S-doped hollow porous tubular g-C_3N_4 for boosted photocatalytic H_2 production. Ceram Int. 2023;49:11989–98.
[142] Abu-Sari SM, Ang BC, Daud WMAW, Patah MFA. Visible-light-driven photocatalytic hydrogen production on defective, sulfur self-doped g-C_3N_4 nanofiber fabricate *via* electrospinning method. J Environ Chem Eng. 2023;11:109318.
[143] Sindhu M, Sharma A, Maan KS, Patel V, Singh PP, Nguyen V-H. Fabrication and characterization of novel V, S co-doped Ta_3N_5 protected with PANI composite materials for hydrogen generation from light-driven water splitting. J Taiwan Inst Chem Eng. 2023;158:105024.
[144] Varma P, Gopannagari M, Reddy KAJ, Kim TK, Reddy DA. Design of $ZnIn_2S_4$@ N-Fe_3C Nanorods-Embedded Nanocages assemblies for Efficient photocatalytic hydrogen generation. ChemCatChem. 2023;15:e202300316.
[145] Suhag MH, Katsumata H, Tateishi I, Furukawa M, Kaneco S. Black Phosphorus-Doped Graphitic Carbon Nitride with Aromatic Benzene Rings for Efficient Photocatalytic Hydrogen Production. Langmuir: ACS J Surf Colloids. 2023;39:13121–31.
[146] Zhang H, Zhu Z, Yang M, Li Y, Lin X, Li M, et al. Constructing the Sulfur-Doped CdO@ In_2O_3 Nanofibers Ternary Heterojunction for Efficient Photocatalytic Hydrogen Production. Nanomaterials. 2023;13:401.
[147] Feng X, Chen H, Yin H, Yuan C, Lv H, Fei Q, et al. Facile synthesis of P-doped $ZnIn_2S_4$ with enhanced visible-light-driven photocatalytic hydrogen production. Molecules. 2023;28:4520.
[148] Wang W, Du L, Xia R, Liang R, Zhou T, Lee HK, et al. In situ protonated-phosphorus interstitial doping induces long-lived shallow charge trapping in porous $C_{3-x}N_4$ photocatalysts for highly efficient H_2 generation. Energy Environ Sci. 2023;16:460–72.
[149] Kang E, Kim JH. Highly boosted photocatalytic H_2 production from ZnS particles assisted by Cd-Cu co-doping. J Environ Chem Eng. 2023;11:109833.
[150] Chen H, Mo Z, Wang Z, Yan P, Sun P, Wu G, et al. Implanting nitrogen-doped graphene quantum dots on porous ultrathin carbon nitride for efficient metal-free photocatalytic hydrogen evolution. J Environ Chem Eng. 2023;11:109801.
[151] Liu T, Wang T, Ding C, Wang M, Wang W, Shen H, et al. One-pot synthesis of carbon coated Cu-doped $ZnIn_2S_4$ core–shell structure for boosted photocatalytic H_2-evolution. Sep Purif Technol. 2023;310:123170.
[152] Kong Y, Li D, Zhang C, Han W, Xue Y, Zhang W, et al. Synergistic silver doping and N vacancy promoting photocatalytic performances of carbon nitride for pollutant oxidation and hydrogen production. Chem Eng J. 2024;479:147676.
[153] Yang D, Qu C, Meng F, Wang L, Li Y, Ye Q, et al. Synergistic enhancement of photocatalytic hydrogen evolution by ultrathin oxygen-doped graphitic carbon nitride nanosheets loaded amorphous mesoporous nickel hydroxide. Sep Purif Technol. 2024;330:125366.
[154] Ren M, Meng J, Yang Y, Zhang X, Yang G, Qin L, et al. Synergy between palladium single atoms and small nanoparticles co-anchored on carbon atom self-doped graphitic carbon nitride boosting photocatalytic H_2 generation. Appl Catal B: Environ Energy. 2024;343:123680.
[155] Ba J, Cai W, Chen Y, Lin L, Huang Y, Yu X, et al. Effective incorporation of Ni dopant into CdS derived from hybrid ZIF for enhanced photocatalytic hydrogen evolution. Int J Hydrogen Energy. 2024;53:1137–48.
[156] Chen Y, Lei L, Gong Y, Wang H, Fan H, Wang W. Enhanced electron delocalization on pyrimidine doped graphitic carbon nitride for boosting photocatalytic hydrogen evolution. Int J Hydrogen Energy. 2024;51:1058–68.
[157] Cui S, Ao R, Lin Z, Ding M. Phosphorous-doped cadmium sulfide hollow octahedrons for enhanced visible-light photocatalytic H_2 evolution. Int J Hydrogen Energy. 2024;51:848–56.
[158] Li J, Hu D, Chen Q. Spin-polarization and crystal structure engineering enhanced photocatalytic H_2 production and photoluminescence properties in cobalt-doped $CsPbBr_3$. Ceram Int. 2024;50:5293–310.
[159] Zhai M, Zhang Y, Xu J, Wang C, Wang L. Controllable introducing C, N-defects and oxygen-doping on carbon nitride to tune electronic structure and boost photocatalytic hydrogen evolution. Appl Surf Sci. 2024;652:159378.
[160] Tian Y, Zeng D, Shen T, Guan R, Shi W. One-step synthesis of S-doped C-vacancy g-C_3N_4 with honeycomb porous nanosheets structure for efficient visible-light-driven hydrogen evolution. Fuel. 2024;357:129927.
[161] Zhao Y, Ding C, Zhu J, Qin W, Tao X, Fan F, et al. A hydrogen farm strategy for scalable solar hydrogen production with particulate photocatalysts. Angew Chem (Int Ed Engl). 2020;59:9653–8.

[162] Guo H-L, Zhu Q, Wu X-L, Jiang Y-F, Xie X, Xu A-W. Oxygen deficient ZnO 1− x nanosheets with high visible light photocatalytic activity. Nanoscale. 2015;7:7216–23.
[163] Takata T, Jiang J, Sakata Y, Nakabayashi M, Shibata N, Nandal V, et al. Photocatalytic water splitting with a quantum efficiency of almost unity. Nature. 2020;581:411–4.
[164] Ju M-G, Wang X, Liang W, Zhao Y, Li C. Tuning the energy bandgap of crystalline gallium oxide to enhance photocatalytic water splitting: mixed-phase junctions. J Mater Chem A. 2014;2:17005–14.
[165] Ai Z, Zhao G, Zhong Y, Shao Y, Huang B, Wu Y, et al. Phase junction CdS: high efficient and stable photocatalyst for hydrogen generation. Appl Catal B: Environ. 2018;221:179–86.
[166] Zhang J, Xu Q, Feng Z, Li M, Li C. Importance of the relationship between surface phases and photocatalytic activity of TiO_2. Angew Chem Int Ed. 2008;120:1790–3.
[167] Khan K, Tao X, Zhao Y, Zeng B, Shi M, Ta N, et al. Spatial separation of dual-co-catalysts on one-dimensional semiconductors for photocatalytic hydrogen production. J Mater Chem A. 2019;7:15607–14.
[168] Maeda K, Xiong A, Yoshinaga T, Ikeda T, Sakamoto N, Hisatomi T, et al. Photocatalytic overall water splitting promoted by two different co-catalysts for hydrogen and oxygen evolution under visible light. Angew Chem Int Ed. 2010;122:4190–3.
[169] Nie X, Li W, Jiang X, Guo X, Song C. Recent advances in catalytic CO_2 hydrogenation to alcohols and hydrocarbons. Adv Catal. 2019;65:121–233.
[170] Liu L, Corma A. Structural transformations of solid electrocatalysts and photocatalysts. Nat Rev Chem. 2021;5:256–76.
[171] Tao X, Shi W, Zeng B, Zhao Y, Ta N, Wang S, et al. Photoinduced surface activation of semiconductor photocatalysts under reaction conditions: a commonly overlooked phenomenon in photocatalysis. ACS Catal. 2020;10:5941–8.
[172] Kato H, Asakura K, Kudo A. Highly efficient water splitting into H_2 and O_2 over lanthanum-doped $NaTaO_3$ photocatalysts with high crystallinity and surface nanostructure. J Am Chem Soc. 2003;125:3082–9.
[173] Zhang Q, Li Z, Wang S, Li R, Zhang X, Liang Z, et al. Effect of redox co-catalysts location on photocatalytic overall water splitting over cubic $NaTaO_3$ semiconductor crystals exposed with equivalent facets. ACS Catal. 2016;6:2182–91.
[174] Townsend TK, Browning ND, Osterloh FE. Overall photocatalytic water splitting with NiO_x–$SrTiO_3$–a revised mechanism. Energy Environ Sci. 2012;5:9543–50.
[175] Karkas MD, Verho O, Johnston EV, Åkermark B. Artificial photosynthesis: molecular systems for catalytic water oxidation. Chem Rev. 2014;114:11863–2001.
[176] Montoya JH, Seitz LC, Chakthranont P, Vojvodic A, Jaramillo TF, Nørskov JK. Materials for solar fuels and chemicals. Nat Mater. 2017;16:70–81.
[177] Long Y, Lin J, Ye F, Liu W, Wang D, Cheng Q, et al. Tailoring the atomic-local environment of carbon nanotube tips for selective H_2O_2 electrosynthesis at high current densities. Adv Mater. 2023;35:2303905.
[178] van Oversteeg CH, Doan HQ, de Groot FM, Cuk T. In situ X-ray absorption spectroscopy of transition metal based water oxidation catalysts. Chem Soc Rev. 2017;46:102–25.
[179] Fang Y, Hou Y, Fu X, Wang X. Semiconducting polymers for oxygen evolution reaction under light illumination. Chem Rev. 2022;122:4204–56.
[180] Sun H, Yan Z, Liu F, Xu W, Cheng F, Chen J. Self-supported transition-metal-based electrocatalysts for hydrogen and oxygen evolution. Adv Mater. 2020;32:1806326.
[181] Maeda K, Teramura K, Lu D, Saito N, Inoue Y, Domen K. Noble-metal/Cr_2O_3 core/shell nanoparticles as a cocatalyst for photocatalytic overall water splitting. Angew Chem Int Ed. 2006;118:7970–3.
[182] Takata T, Pan C, Nakabayashi M, Shibata N, Domen K. Fabrication of a core–shell-type photocatalyst via photodeposition of group IV and V transition metal oxyhydroxides: an effective surface modification method for overall water splitting. J Am Chem Soc. 2015;137:9627–34.
[183] Bau JA, Takanabe K. Ultrathin microporous SiO_2 membranes photodeposited on hydrogen evolving catalysts enabling overall water splitting. ACS Catal. 2017;7:7931–40.
[184] Chiang TH, Lyu H, Hisatomi T, Goto Y, Takata T, Katayama M, et al. Efficient photocatalytic water splitting using Al-doped $SrTiO_3$ coloaded with molybdenum oxide and rhodium–chromium oxide. ACS Catal. 2018;8:2782–8.
[185] Maeda K, Teramura K, Saito N, Inoue Y, Domen K. Improvement of photocatalytic activity of (Ga1−xZnx)(N1−xOx) solid solution for overall water splitting by co-loading Cr and another transition metal. J Catal. 2006;243:303–8.
[186] Yoshida M, Takanabe K, Maeda K, Ishikawa A, Kubota J, Sakata Y, et al. Role and function of noble-metal/Cr-layer core/shell structure co-catalysts for photocatalytic overall water splitting studied by model electrodes. J Phys Chem C. 2009;113:10151–7.
[187] Pan C, Takata T, Nakabayashi M, Matsumoto T, Shibata N, Ikuhara Y, et al. A complex perovskite-type oxynitride: the first photocatalyst for water splitting operable at up to 600 nm. Angew Chem Int Ed. 2015;54:2955–9.
[188] Hang Li Y, Xing J, Jia Chen Z, Li Z, Tian F, Rong Zheng L, et al. Unidirectional suppression of hydrogen oxidation on oxidized platinum clusters. Nat Commun. 2013;4:2500.
[189] Dau H, Limberg C, Reier T, Risch M, Roggan S, Strasser P. The mechanism of water oxidation: from electrolysis via homogeneous to biological catalysis. ChemCatChem. 2010;2:724–61.
[190] Zhang X, Bieberle-Hütter A. Modeling and simulations in photoelectrochemical water oxidation: from single level to multiscale modeling. ChemSusChem. 2016;9:1223–42.
[191] Tao X, Zhao Y, Mu L, Wang S, Li R, Li C. Bismuth tantalum oxyhalogen: a promising candidate photocatalyst for solar water splitting. Adv Energy Mater. 2018;8:1701392.
[192] Maeda K, Teramura K, Lu D, Takata T, Saito N, Inoue Y, et al. Photocatalyst releasing hydrogen from water. Nature. 2006;440:295.
[193] Zhang N, Yang M-Q, Liu S, Sun Y, Xu Y-J. Waltzing with the versatile platform of graphene to synthesize composite photocatalysts. Chem Rev. 2015;115:10307–77.
[194] Zou Z, Ye J, Sayama K, Arakawa H. Direct splitting of water under visible light irradiation with an oxide semiconductor photocatalyst. Nature. 2001;414:625–7.
[195] Liu S, Yu J, Jaroniec M. Tunable photocatalytic selectivity of hollow TiO_2 microspheres composed of anatase polyhedra with exposed {001} facets. J Am Chem Soc. 2010;132:11914–6.
[196] Vaudreuil S, Bousmina M, Kaliaguine S, Bonneviot L. Synthesis of macrostructured silica by sedimentation–aggregation. Adv Mater. 2001;13:1310–2.
[197] Wang L, Duan X, Wang G, Liu C, Luo S, Zhang S, et al. Omnidirectional enhancement of photocatalytic hydrogen

evolution over hierarchical “cauline leaf” nanoarchitectures. Appl Catal B: Environ. 2016;186:88–96.
[198] Rao VN, Kwon H, Lee Y, Ravi P, Ahn CW, Kim K, et al. Synergistic integration of MXene nanosheets with CdS@TiO_2 core@ shell S-scheme photocatalyst for augmented hydrogen generation. Chem Eng J. 2023;471:144490.
[199] Antonelli DM, Ying J. Synthesis of a stable hexagonally packed mesoporous niobium oxide molecular sieve through a novel ligand-assisted templating mechanism. Angew Chem Int Ed Engl. 1996;35:426–30.
[200] Dacquin J-P, Dhainaut J, Duprez D, Royer S, Lee AF, Wilson K. An efficient route to highly organized, tunable macroporous–mesoporous alumina. J Am Chem Soc. 2009;131:12896–7.
[201] Sun B, Zhou W, Li H, Ren L, Qiao P, Li W, et al. Synthesis of particulate hierarchical tandem heterojunctions toward optimized photocatalytic hydrogen production. Adv Mater. 2018;30:1804282.
[202] Strand J, Shluger AL. On the structure of oxygen deficient amorphous oxide films. Adv Sci (Weinheim, Baden-Wurttemberg, Ger). 2023;11:2306243.
[203] Amoresi RAC, Junior UC, Simões AZ, Perazolli LA, Longo E, Andrés J. Oxygen defects, morphology, and surface chemistry of metal oxides: a deep insight through a joint experimental and theoretical perspective. Metal Oxide Defects. Elsevier; 2023. p. 191–215.
[204] John L, Murugesan S, Ravindranath NA, Clinsha P, Parida PK, Mythili R, et al. Phase pure $PdCoO_2$ delafossite using molten salt route: Structural, photoemission and magnetic characterization. J Solid State Chem. 2024;329:124426.
[205] Zhang H, Yu L, Chen T, Zhou W, Lou XW. Surface modulation of hierarchical MoS_2 nanosheets by Ni single atoms for enhanced electrocatalytic hydrogen evolution. Adv Funct Mater. 2018;28:1807086.
[206] Wexler RB, Gautam GS, Stechel EB, Carter EA. Factors governing oxygen vacancy formation in oxide perovskites. J Am Chem Soc. 2021;143:13212–27.
[207] Pamplin BR. Crystal growth: International series on the Science of the solid state. Elsevier; 2013.
[208] Hwang J, Rao RR, Giordano L, Katayama Y, Yu Y, Shao-Horn Y. Perovskites in catalysis and electrocatalysis. Sci (N York, NY). 2017;358:751–6.
[209] Greiner MT, Lu Z-H. Thin-film metal oxides in organic semiconductor devices: their electronic structures, work functions and interfaces. NPG Asia Mater. 2013;5:e55-e.
[210] Le Formal F, Pendlebury SR, Cornuz M, Tilley SD, Grätzel M, Durrant JR. Back electron–hole recombination in hematite photoanodes for water splitting. J Am Chem Soc. 2014;136:2564–74.
[211] Chen X, Liu L, Huang F. Black titanium dioxide (TiO_2) nanomaterials. Chem Soc Rev. 2015;44:1861–85.
[212] Kisch H. Semiconductor photocatalysis—mechanistic and synthetic aspects. Angew Chem Ind Ed. 2013;52:812–47.
[213] Tilley SD. Will Cuprous Oxide Really Make It in Water-Splitting Applications? ACS Energy Lett. 2023;8:2338–44.
[214] Rahman MZ, Edvinsson T, Gascon J. Hole utilization in solar hydrogen production. Nat Rev Chem. 2022;6:243–58.
[215] Selim S, Pastor E, Garcia-Tecedor M, Morris MR, Francas L, Sachs M, et al. Impact of oxygen vacancy occupancy on charge carrier dynamics in $BiVO_4$ photoanodes. J Am Chem Soc. 2019;141:18791–8.
[216] Tsai K-A, Lai C-C, Chen Y-H, Leu C, Chang J-C, Kuo C-Y, et al. Exploring the impact of surface oxygen vacancies on charge carrier dynamics in $BiVO_4$ photoanodes through atmospheric pressure plasma jet post-treatment for efficiency improvement in photoelectrochemical water oxidation. Appl Catal B: Environ. 2024;341:123288.
[217] Pryds N, Park D-S, Jespersen T, Yun S. Twisted oxide membranes: A perspective. APL Mater. 2024;12:010901.
[218] Zhang X, Hao W, Tsang C-S, Liu M, Hwang GS, Lee LYS. Psesudocubic phase tungsten oxide as a photocatalyst for hydrogen evolution reaction. ACS Appl Energy Mater. 2019;2:8792–800.
[219] Gan J, Lu X, Wu J, Xie S, Zhai T, Yu M, et al. Oxygen vacancies promoting photoelectrochemical performance of In_2O_3 nanocubes. Sci Rep. 2013;3:1021.
[220] Zhou Z, Liu J, Long R, Li L, Guo L, Prezhdo OV. Control of charge carriers trapping and relaxation in hematite by oxygen vacancy charge: ab initio non-adiabatic molecular dynamics. J Am Chem Soc. 2017;139:6707–17.
[221] Zhang YC, Afzal N, Pan L, Zhang X, Zou JJ. Structure-activity relationship of defective metal-based photocatalysts for water splitting: experimental and theoretical perspectives. Adv Sci. 2019;6:1900053.
[222] Xiong J, Di J, Xia J, Zhu W, Li H. Surface defect engineering in 2D nanomaterials for photocatalysis. Adv Funct Mater. 2018;28:1801983.
[223] Wang S, Pan L, Song J-J, Mi W, Zou J-J, Wang L, et al. Titanium-defected undoped anatase TiO_2 with p-type conductivity, room-temperature ferromagnetism, and remarkable photocatalytic performance. J Am Chem Soc. 2015;137:2975–83.
[224] Fu X, Wang X, Chen Z, Zhang Z, Li Z, Leung DY, et al. Photocatalytic performance of tetragonal and cubic β-In_2S_3 for the water splitting under visible light irradiation. Appl Catal B: Environ. 2010;95:393–9.
[225] Hao X, Wang Y, Zhou J, Cui Z, Wang Y, Zou Z. Zinc vacancy-promoted photocatalytic activity and photostability of ZnS for efficient visible-light-driven hydrogen evolution. Appl Catal B: Environ. 2018;221:302–11.
[226] Chen R, Pang S, An H, Dittrich T, Fan F, Li C. Giant defect-induced effects on nanoscale charge separation in semiconductor photocatalysts. Nano Lett. 2018;19:426–32.
[227] Zhou J, Zhao J, Liu R. Defect engineering of zeolite imidazole framework derived ZnS nanosheets towards enhanced visible light driven photocatalytic hydrogen production. Appl Catal B: Environ. 2020;278:119265.
[228] Du X, Song S, Wang Y, Jin W, Ding T, Tian Y, et al. Facile one-pot synthesis of defect-engineered step-scheme WO_3/gC_3N_4 heterojunctions for efficient photocatalytic hydrogen production. Catal Sci Technol. 2021;11:2734–44.
[229] Zhang X, Yao Q, Wu H, Zhou Y, Zhu M, Lu Z-H. Carbon-doped mesoporous TiO_2-immobilized Ni nanoparticles: Oxygen defect engineering enhances hydrogen production. Appl Catal B: Environ. 2023;339:123153.
[230] Zhang S, Liu X, Liu C, Luo S, Wang L, Cai T, et al. MoS_2 quantum dot growth induced by S vacancies in a $ZnIn_2S_4$ monolayer: atomic-level heterostructure for photocatalytic hydrogen production. ACS Nano. 2018;12:751–8.
[231] Du C, Zhang Q, Lin Z, Yan B, Xia C, Yang G. Half-unit-cell $ZnIn_2S_4$ monolayer with sulfur vacancies for photocatalytic hydrogen evolution. Appl Catal B: Environ. 2019;248:193–201.

[232] Li R, Wen C, Yan K, Liu T, Zhang B, Xu M, et al. The water splitting cycle for hydrogen production at photo-induced oxygen vacancies using solar energy: experiments and DFT calculation on pure and metal-doped CeO_2. J Mater Chem A. 2023;11:7128–41.
[233] Cai J, Cao A, Huang J, Jin W, Zhang J, Jiang Z, et al. Understanding oxygen vacancies in disorder-engineered surface and subsurface of $CaTiO_3$ nanosheets on photocatalytic hydrogen evolution. Appl Catal B: Environ. 2020;267:118378.
[234] Bi Y, Wang Y, Dong X, Zheng N, Ma H, Zhang X. Efficient solar-driven conversion of nitrogen to ammonia in pure water via hydrogenated bismuth oxybromide. RSC Adv. 2018;8:21871–8.
[235] Babu SJ, Rao VN, Murthy DH, Shastri M, Murthy M, Shetty M, et al. Significantly enhanced cocatalyst-free H_2 evolution from defect-engineered Brown TiO_2. Ceram Int. 2021;47:14821–8.
[236] Xie YP, Yang Y, Wang G, Liu G. Oxygen vacancies promoted interfacial charge carrier transfer of CdS/ZnO heterostructure for photocatalytic hydrogen generation. J Colloid Interface Sci. 2017;503:198–204.
[237] Zhang G, Jiang W, Hua S, Zhao H, Zhang L, Sun Z. Constructing bulk defective perovskite $SrTiO_3$ nanocubes for high performance photocatalysts. Nanoscale. 2016;8:16963–8.
[238] Zhang Y, Xu Z, Li G, Huang X, Hao W, Bi Y. Direct observation of oxygen vacancy self-healing on TiO_2 photocatalysts for solar water splitting. Angew Chem (Int Ed Engl). 2019;58:14229–33.
[239] Sambandam B, Michael RJV, Manoharan PT. Oxygen vacancies and intense luminescence in manganese loaded Zno micro-flowers for visible light water splitting. Nanoscale. 2015;7:13935–42.
[240] Dunn S, Jones PM, Gallardo DE. Photochemical growth of silver nanoparticles on c^- and c^+ domains on lead zirconate titanate thin films. J Am Chem Soc. 2007;129:8724–8.
[241] Chen F, Huang H, Guo L, Zhang Y, Ma T. The role of polarization in photocatalysis. Angew Chem (Int Ed Engl). 2019;58:10061–73.
[242] Li L, Salvador PA, Rohrer GS. Photocatalysts with internal electric fields. Nanoscale. 2014;6:24–42.
[243] Lv Y, Hu C, Yu J, Jiang H, Huang T. Local spatial charge separation and proton activation induced by surface hydroxylation promoting photocatalytic hydrogen evolution of polymeric carbon nitride. IEEE Trans Cybern. 2018;50:383–92.
[244] Hu C, Chen F, Wang Y, Tian N, Ma T, Zhang Y, et al. Exceptional cocatalyst-free photo-enhanced piezocatalytic hydrogen evolution of carbon nitride nanosheets from strong in-plane polarization. Adv Mater. 2021;33:2101751.
[245] Barrio J, Barzilai S, Karjule N, Amo-Ochoa P, Zamora F, Shalom M. Synergistic doping and surface decoration of carbon nitride macrostructures by single crystal design. ACS Appl Energy Mater. 2021;4:1868–75.
[246] Li X, Bartlett SA, Hook JM, Sergeyev I, Clatworthy EB, Masters AF, et al. Salt-enhanced photocatalytic hydrogen production from water with carbon nitride nanorod photocatalysts: cation and pH dependence. J Mater Chem A. 2019;7:18987–95.
[247] Teixeira IF, Tarakina NV, Silva IF, López-Salas N, Savateev A, Antonietti M. Overcoming Electron Transfer Efficiency Bottlenecks for Hydrogen Production in Highly Crystalline Carbon Nitride-Based Materials. Adv Sustain Syst. 2022;6:2100429.
[248] Jia M, Ren F, Chen X, Han W, Jin C, Peng C, et al. Polarization and built-in electric field improve the photocatalytic overall water splitting efficiency of C_2N/ZnSe heterostructures. Int J Hydrogen Energy. 2023;48:19554–63.
[249] Li Z, Zhang L, Liu Y, Shao C, Gao Y, Fan F, et al. Surface-polarity-induced spatial charge separation boosts photocatalytic overall water splitting on GaN nanorod arrays. Angew Chem. 2020;132:945–52.
[250] Khan M, Nadeem M, Idriss H. Ferroelectric polarization effect on surface chemistry and photo-catalytic activity: A review. Surf Sci Rep. 2016;71:1–31.
[251] Li R, Zhao Y, Li C. Spatial distribution of active sites on a ferroelectric $PbTiO_3$ photocatalyst for photocatalytic hydrogen production. Faraday Discuss. 2017;198:463–72.
[252] Huang H, Tu S, Du X, Zhang Y. Ferroelectric spontaneous polarization steering charge carriers migration for promoting photocatalysis and molecular oxygen activation. J Colloid Interface Sci. 2018;509:113–22.
[253] Li H, Quan X, Chen S, Yu H. Ferroelectric-enhanced Z-schematic electron transfer in $BiVO_4$-$BiFeO_3$-$CuInS_2$ for efficient photocatalytic pollutant degradation. Appl Catal B: Environ. 2017;209:591–9.
[254] Park S, Lee CW, Kang M-G, Kim S, Kim HJ, Kwon JE, et al. A ferroelectric photocatalyst for enhancing hydrogen evolution: polarized particulate suspension. Phys Chem Chem Phys. 2014;16:10408–13.
[255] Liu Y, Ye S, Xie H, Zhu J, Shi Q, Ta N, et al. Internal-field-enhanced charge separation in a single-domain ferroelectric $PbTiO_3$ photocatalyst. Adv Mater. 2020;32:1906513.
[256] Chen W-T, Chan A, Sun-Waterhouse D, Moriga T, Idriss H, Waterhouse GI. Ni/TiO_2: A promising low-cost photocatalytic system for solar H_2 production from ethanol–water mixtures. J Catal. 2015;326:43–53.
[257] Dharani S, Vadivel S, Gnanasekaran L, Rajendran S. S-scheme heterojunction photocatalysts for hydrogen production: Current progress and future prospects. Fuel. 2023;349:128688.
[258] Wang X, Jin Z. Adjusting inter-semiconductor barrier height *via* crystal plane engineering: Crystalline face exposed single crystal cadmium sulfide augmentative S-scheme heterojunctions for efficiently photocatalytic hydrogen production. Appl Catal B: Environ. 2024;342:123373.
[259] Li T, Tsubaki N, Jin Z. S-scheme heterojunction in photocatalytic hydrogen production. J Mater Sci & Technol. 2024;169:82–104.
[260] Schumacher L, Marschall R. Recent advances in semiconductor heterojunctions and Z-schemes for photocatalytic hydrogen generation. Top Curr Chem. 2022;380:53.
[261] Qi Y, Zhou G, Wu Y, Wang H, Yan Z, Wu Y. *In situ* construction of In_2O_3/In_2S_3-$CdIn_2S_4$ Z-scheme heterojunction nanotubes for enhanced photocatalytic hydrogen production. J Colloid Interface Sci. 2024;664:107–16.
[262] Liu J, Sun X, Fan Y, Yu Y, Li Q, Zhou J, et al. P-N heterojunction embedded CuS/TiO_2 bifunctional photocatalyst for synchronous hydrogen production and benzylamine conversion. Small. 2024;20:2306344.
[263] Ge W, Song J, Deng S, Liu K, Yang P. Construction of Z-scheme $CoFe_2O_4$@ $ZnIn_2S_4$ pn heterojunction for enhanced photocatalytic hydrogen production. Sep Purif Technol. 2024;328:125059.
[264] Sun S, Ren D, Yang M, Cui J, Yang Q, Liang S. *In situ* construction of direct Z-scheme sea-urchin-like ZnS/SnO_2 heterojunctions for boosted photocatalytic hydrogen production. Int J Hydrogen Energy. 2022;47:9201–8.
[265] Cheng Y, Dou M, Yao M, Ding K, Shao H, Liu Y, et al. Reverse-type-I $MnCo_2S_4$/CdS heterojunction nanorods for highly efficient photocatalytic hydrogen production under visible light irradiation. ACS Appl Nano Mater. 2023;6:16837–45.

[266] Xue X, Lu C, Luo M, Han T, Liu Y, Ge Y, et al. Type-I $SnSe_2$/ZnS heterostructure improving photoelectrochemical photodetection and water splitting. Sci China Mater. 2023;66:127–38.
[267] Cao J, Zhang J, Guo W, Chen H, Li J, Jing D, et al. A type-I heterojunction by anchoring ultrafine Cu_2O on defective TiO_2 framework for efficient photocatalytic H_2 production. Ind & Eng Chem Res. 2023;62:1310–21.
[268] Zhu K, Zhang F, Cai W, Liu C, Wang Y, Meng Z, et al. A novel I-type 0D/0D ZnS/$Ag_6Si_2O_7$ heterojunction for photocatalytic hydrogen evolution. J Phys Chem Solids. 2023;175:111206.
[269] Xu S, Xu J, Wu J, Zhou Z, Wang B, Lan T. Designing of a novel $Mn_{0.2}Cd_{0.8}S$@ZnO heterostructure with Type-II charge transfer path for efficient photocatalytic hydrogen evolution reaction. Int J Hydrogen Energy. 2023;48:7670–82.
[270] Wang Y, Gudiño L, Bedia J, Belver C. Solar photocatalytic hydrogen production through metal sulfide/UiO-66-NH_2 heterojunctions. Sep Purif Technol. 2024;353:128663.
[271] Peng K, Yu S, Luo Y, Zhang A, Xie Y, Luo Y, et al. Enhancement TiO_2 photocatalytic hydrogen production *via* using ABO_3 to construct heterojunction. Colloids Surf A: Physicochem Eng Asp. 2024;682:132822.
[272] Li P-Y, Yuan J-H, Wang J, Wang Y, Zhang P. GaSe/$YAlS_3$: A type-II van der Waals heterostructure with ultrahigh solar-to-hydrogen efficiency for photocatalytic water splitting. Int J Hydrogen Energy. 2024;55:1254–64.